NORTHWESTERN UNIVERSITY

Thermally Activated Self-lubricating Nanostructured Coating for Cutting Tool Applications

A DISSERTATION

SUBMITTED TO THE GRADUATE SCHOOL
IN PARTIAL FULFILLMENT OF THE REQUIREMENTS

for the degree

DOCTOR OF PHILOSOPHY

Field of Materials Science & Engineering

By

Robin Abraham Koshy

EVANSTON, ILLINOIS

December 2008

ABSTRACT

Thermally activated self-lubricating nanolayer coating for cutting tool applications

Robin Abraham Koshy

The different nitride phases of Cr and Mo were studied as possible candidates in a bi-layered system that would constitute a thermally activated self lubrication coatings for dry cutting applications. The intent was to deposit multilayer films of CrN and Mo_2N, where the Mo_2N forms a sacrificial oxide that lubricates at high temperature. The multilayer coatings were hard (>25GPA), oxidation resistant (>600°C) and retained its nanolayered structure up to high temperatures (>1000°C). TGA and SEM studies show that the CrN acts as a diffusion barrier to oxygen and protects the underlying coating from oxidation. The reduction of friction at high temperature points to a thermally activated self lubricating mechanism in operation. As the coating wears the multilayer arrangement ensures the constant supply of lubricating oxides (from the Mo_2N layer) at the sliding interface. XPS analysis of the transfer film, verify the presence of MoO_3 as the primary constituent of the wear debris. Friction tests in a near N_2 atmosphere shows a further lowering of friction at high temperature. This enhanced lowering of friction is linked to lower oxidation rates of the surface in the near nitrogen atmosphere (~2-5% of O_2). Hence controlling the oxygen content in the test environment could allow us to control the oxidation rate and hence the friction regime of the coating.

The coatings were deposited on HSS and WC drill bits for industrial validation testing. Well adhered CrN/Mo_2N multilayer films, ~ 4 μm thick, were deposited with different bi-layer periodicity and CrN:Mo_2N ratios. The coatings exhibited lower torque and thrust values when compared to uncoated drill bits. The industrial tests were inconclusive because temperatures high

enough to activate lubrication were not achieved or metal adhesion prevented the mechanism from operating. Other phases, such as BN, that oxidized at lower temperature and formed lubricating oxides at relatively lower temperatures were explored. Effects of varying bias, partial pressure and power on the properties of composite BN-Mo_2N coatings were studied. a-BN deposited in the composite at 120V bias, -50 V and 2kW formed h-BN on annealing. Other addition (W) to the CrN/(BN-Mo_2N) coating were also proposed.

Dedicated to my dear father, mother and my grandmother,
The late Mr. Koshy Abraham, Mrs. Rajamma Thomas
And the late Mrs. Achamma Abraham
(D/o Mr. C.C Koshy, Chavnikamanil)

TABLE OF CONTENTS

6.3 Deposition rate, compressive stress and TGA studies on co-deposited samples..... 160

LIST OF TABLES

LIST OF FIGURES

Chapter 1. Introduction: Hard Coatings and self-lubrication

1.1 Hard Coatings

Protective Coatings on cutting tools have been in use for a little more than three decades. The drivers for current developments of hard coatings are increasing machine productivity, novel and hard to cut materials and changing environmental mandates. It is the intimate connection between hardness and wear that has driven the industry and researchers alike to pursue hard coatings. As the diversity of the applications of coatings grows to include aerospace and automotive applications, so do the environments in which they operate. The search for wear resistant materials has since been redirected to encompass other material properties rather than just hardness[1]. Wear of materials depends on a range of factors including surface friction, elastic modulus, fracture toughness, contact geometry and environment and chemical reactivity. Cutting performance is also dependant on both the cutting tool and the machine tool system. Cutting tool performance is dependant on tool material, cutting tool geometry and hard coatings. We will focus our efforts on the development of cutting tools, particularly on the coating side of the cutting process. Hard coatings have been integrated into cutting tools for three decades yielding tremendous performance and productivity benefits in industrial metal cutting [2]. Early hard coatings such as TiC and TiN were deposited via chemical vapour deposition (CVD). Physical vapour deposition is the current deposition technique of choice because it can form a conformal, well adhered alloy at low deposition temperatures. Other techniques for hard coatings deposition include plasma assisted CVD/PVD and laser assisted methods like pulsed laser deposition (PLD). The large majority of coatings based on cemented carbide substrates are coated for wear protection using CVD or PVD techniques [3]. Current development has included

multilayers of TiCN, TiAlN, Al_2O_3, AlCrN, $(AlCr)_2O_3$ and super hard diamond like carbon (DLC) coatings. Super hard coatings including DLC and cubic-BN were a huge breakthrough for machining non-ferrous alloys. Figure 1(a) shows a generic scheme of how properties have improved with time. Figure 1 (b) and (c) shows multilayers and nanolayers of AlCrN-TiSiN and TiAlN respectively which represents significant advancements in coating performance. (Figure 1)(d) shows a selection guide based of hard coatings based on field performance and commercial acceptance. The materials selection is based on speed of drilling, hardness and ductility of the work piece which is represented on the each axis. The (Figure 1)(d) shows the change in coating selection from monolithic TiN to multilayers and nano-layers and nanolayers of AlCrN and AlTiN with higher cutting forces and increasing speed. The focus of development as demonstrated above has been to increase hardness and oxidation resistance to achieve increased performance and coating durability. The life of the tool is extended because it is stronger and reduces metal adhesion to the ceramic coating. Some of these hard coatings resisted coating loss by forming protective oxides on the surface. Oxidation damage to cutting tools is a serious concern given the possibility of the tool edge reaching temperatures in excess of 1000°C especially in situations of dry lubrication. A hard well adhered ceramic coating reduces wear and metal buildup, by reducing the forces needed for chip removal, which in turn reduces the overall energy requirement. Such coatings provide a low friction surface, which leads to overall energy conservation.

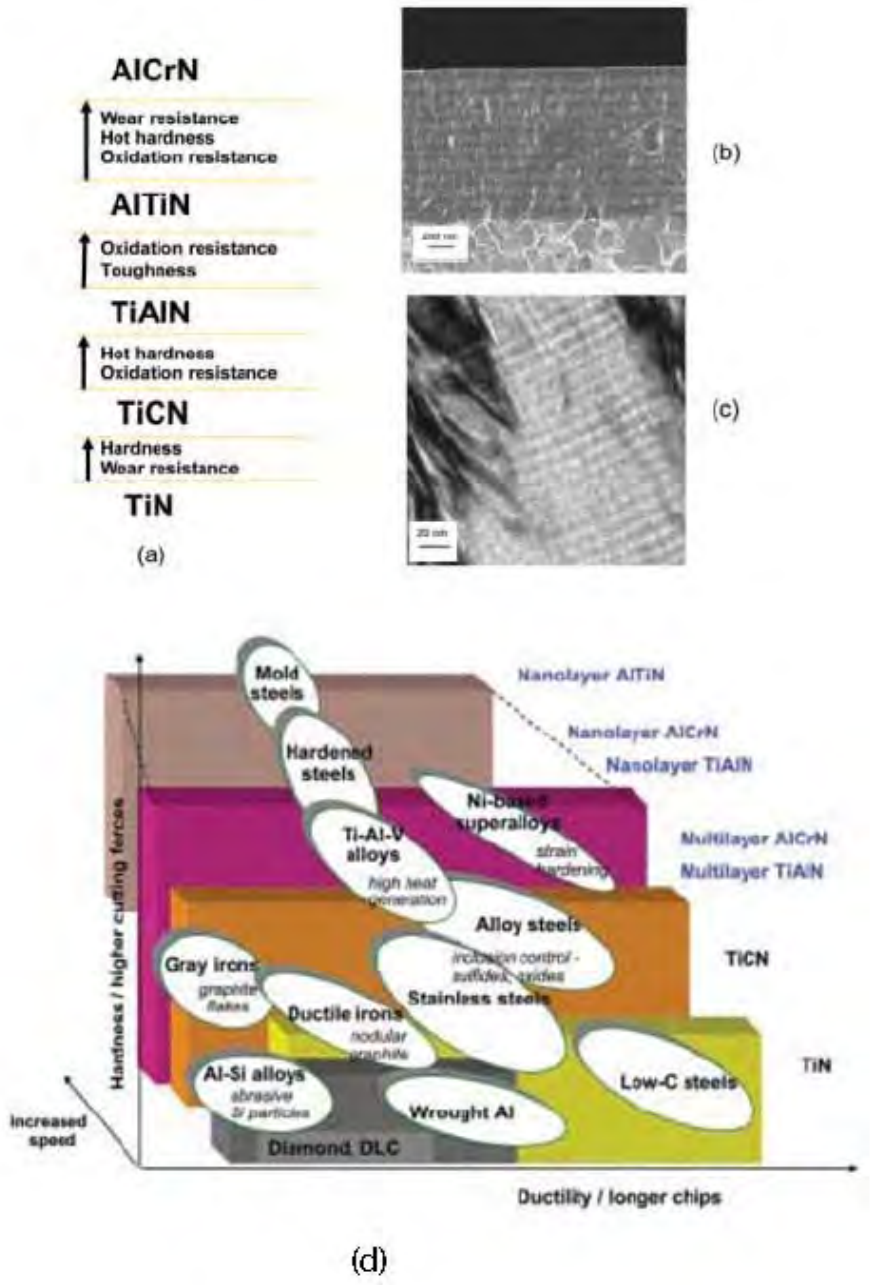

Figure 1. (a) Coating property trends in PVD coatings; (b) Multilayer AlCrN-TiSiN;(c) nanolayer TiAlN (d) Coating selection guide based on field performance and commercial acceptance[reproduced from SVC bulletin, Oct 2007,Dennis.T.Qinto].

The following sections will out line some of the techniques of making hard coatings. The chapter will also outline some of the current methods of lubricating drill bits in machining processes. Some of the initial efforts at implementing self-lubricating coatings will also be discussed. I will discuss some of the potential materials systems that could be candidates in our self-lubricating coatings. Finally this chapter will examine the reason behind the materials system chosen and the properties expected.

Nano-composites: The nano-composite phases about 3-10 nm in size, have been selected from nitrides, carbides, borides and oxides, and are imbedded in an amorphous or crystalline matrix. The encapsulation restricts dislocation activity, diverts and arrests macro-crack development and maintains a high level of hardness leading in some cases to the formation of super-hard coatings. The large volume of grain boundaries provide ductility through grain boundary sliding and nano-cracking along grain/matrix interfaces [4]. These coatings have been at times reported to have hardnesses above 100GPa [5]. A graded interface layer could be applied between the coating and the tool to increase adhesion and to relieve stress. A few examples are CrN/Ni, TiN/TiB_2, TiN/c-BN, Mo_2C/a-(C-Mo_2N) and WC/DLC.

Tough multilayer coatings: These coatings apart from being hard also provide increased benefits from having high strength and fracture toughness. Strain relaxation and mechanism for crack termination in these coatings leads to films with high cohesive toughness. The interface in the multilayer provides a region where cracks can be deflected and stresses can be relaxed. A good chemical adhesion between layers coupled with minimal differences in elastic modulus leads to continuous strain fields across the interfaces. Large changes in stress fields across interfaces typically lead to crack initiations and interfacial crack propagation. cTiC/TiB_2 [6]and

TiN/Ti(C, N)[7] are typical examples of hard tough multilayers coatings with excellent properties.

Functionally graded coatings: The basic idea behind functional grading is to achieve better adhesion, mechanical properties and oxidation resistance by transitioning between the substrate and the final hard coating with a suitable interface material. For example to enhance the properties of WC, an adhesion layer of TiN is deposited, followed by a TiC transition layer and finally WC is deposited as the top-coat [8]. The gradual build-up of material stiffness avoids the formation of sharp interfaces and provides good chemical continuity and load support for the hardest top layer. The presence of equiaxed grain shapes, high angle grain boundaries and low surface energy facilitate grain boundary sliding and incorporating these properties into coatings introduces ductility and prevents fracture. Nano-crystalline carbides with an amorphous DLC matrix designated as TiC/DLC and WC/DLC are typically examples of tough wear resistant composites.

1.2 Wet Machining

Heat generation and friction between tool and chip usually limit machining performance by causing dimensional deviations and premature failure of cutting tools in metal cutting operations. Coolants and lubricants have been traditionally used in high quantities to reduce temperature and friction in the cutting area. Metal cutting fluids are advantageous to the performance of machining operations due to their chip flushing functions as well, but cutting fluids that conform to evolving environmental and employee health standards are forming larger fractions of machining budgets. In some cases, the efficiency of cutting fluids in high speed machining operations have been questioned, since it is unclear if the coolant penetrates into the chip-tool

interface. Over the next decade, legislation from national and international authorities is expected to eliminate hazardous wet lubricants[9] and force a dry or semi-dry machining operation in industry. Currently the machine tool industry lacks cost effective, viable self lubricating coatings. Some of the efforts towards developing cost effective, environmentally sensitive tool coatings will be discussed below.

1.3 Green Machining

The interest in environment friendly “green” manufacturing has spurred development of coatings in the category of dry machining. The concept is to minimize the use of coolants that must be collected and treated. This eliminates the creation of waste that causes long term harm to the environment by improper disposal. Efforts have been mounted across the world to tackle this problem because it is recognized that “manufacturing” is the single biggest generator of waste (by weight) in our industrial society and that a substantial fraction of this weight is liquid. 1985 numbers showed nearly 6 billion tons of waste compared to the second place industry sector of mining at only 1.5 billion tons. Individual governments and many major industrialized countries have also formed alliances to study and solve the major problems with manufacturing waste. Metal removal practices are recognized as primary contributors to the waste generation in the form of cutting fluids and solid chips. There are systems approaches to tackle the overall problem so that process optimization can be done in many areas to reduce fluid use, but certainly, directly attacking the problem by a dry machining strategy is desirable. European estimates of reductions on the order of 60% of fluid usage and nearly 50% of the power usage by optimized machining processes are very attractive [10].

Success can be realized in part if the cooling and lubrication functions can be satisfied or mitigated by appropriate coating design. That is, if tools (coatings) can effectively tolerate high temperatures or can help to reduce them, then coolant usage can be reduced. If the friction level due to the cutting process can be minimized, then lubricant usage can be reduced along with power requirements. Additionally, benefits are gained from reduced amounts of materials and associated handling, and from reduced employee exposure to health-hazards with the elimination of the coolants/lubricants. Trends in OSHA compliance on indoor air quality in the workplace are targeting coolant/lubricant emission sites in manufacturing environments. The implications, opportunities, and challenges for coating designers are to get durability and performance from the make up of the coating and its reaction with the cutting environment.[11] Some of the effects on dry or near dry machining will be discussed below.

1.4 Hard Coatings with a low friction additive

The intent in encapsulating a low friction phase in a hard coating is to ensure low friction during wear. Traditionally the solid self-lubricating composites have been synthesized from powders and through power metallurgical techniques incorporated into a coating. In such cases the low melting phases in the sintered mix have suffered from oxidation and partial burning. This further damages their lubricating properties. Researchers have overcome sintering issues by drilling holes in ceramics and filling them with lubricious materials like intercalated graphite or h-BN[12]. Other instances generally involve incorporating a low melting metal or alloy into ceramics preforms and then demonstrating low friction at high temperature. These materials had their draw backs since the continuity of the hard-phase was broken and hence, reduced both material strength and wear resistance of the final sintered composite. Some of these problems

can be overcome by incorporating nanocrystalline composites in an amorphous matrix. These materials have shown tremendous advancements in hardness[4], toughness[13] and wear resistance[14], while providing reduction in friction at higher temperatures. The incorporation of MoS_2 in DLC matrix, either as nanocrystalline or as laser processed reservoirs has been shown to demonstrate a reduction in friction while maintaining the same level of hardness of the bulk. DLC's unfortunately are not stable at temperatures above 300°C and hence cannot be a suitable coating for high temperature applications. Hence, significant progress still remains to be made in developing hard coatings with incorporated lubricious phases that work at high temperatures.

1.5 Hard coatings incorporating lubricious phase as multilayers

Industry and the research community alike have initiated efforts to incorporate a hard phase into the coating that is lubricious at high temperature[15]. This will be the direction of our research too. Our efforts will be to develop a multi-component multi-functional coating without compromising its bulk properties. It will have high strength that will persist to high temperature, excellent toughness to resist cracking and delamination, low wear and optimized friction, and the ability to self-lubricate by forming oxides at temperatures appropriate for the work piece cutting conditions. Our effort is to make improvements in coating design and materials selections, essentially tackling the challenge of how to incorporate desirable materials into the coating in a form that best takes advantage of the synergism of material properties. This typically means a compromise when trying to combine a hard, durable coating with a lubricious element or compound that might reduce friction, which, if present on the surface, will readily wear away, and if incorporated into the coating, will ruin the structural integrity of the coating.

The cutting performance of a tool is a result of the complex interaction of many factors, including tool design (geometry), base material, coating, surface topography and the work piece. The phenomena that come into play at the interface involve all the components through their affects on sliding friction, elastic/plastic deformation, and wear resistance. Clearly, the strength of the tool must be greater than that of the work piece, and the coating must be durable so that it remains functional for a sufficiently long time. Key functions of the coating are to provide the right friction, reduced metal buildup, oxidation resistance, and the right degree of abrasiveness of the tool relative to the work piece material. For instance, one wants minimal friction between the cut surface and the tool, since any frictional work here just serves to waste energy and heat the pieces. However, one does not want to eliminate all interactions between the cut surface and the tool, since abrasion between the two will have an influence on the roughness of the surface finish, which in many practical applications should be as small as possible. The coating surface will wear to some extent and "evolve" during cutting, and it is desired that a steady-state condition be created for long term predictable behavior in terms of cutting rate and surface finish.

As the coated tool coating begins to wear, the nanolayers are exposed and the layer functionalities are enabled. That is, oxide formers are exposed to the cutting action and can produce lubricious phases to facilitate movement of cut metal against the tool surface with reduced friction if the conditions generate a high enough temperature. Where these layers are preferentially worn, a tool surface topography is developed that is partly dependent on this wear mode and the coating structure. This could be beneficial or detrimental. It could, in certain cases, aid in retaining the abrasiveness (cutting engagement) of the tool surface to help cut into the work piece on one hand and create the desired surface finish on the other. The role of

coating structure on cutting effectiveness and surface finish will be interesting to study and the results will feed back into the design methodology for the coating. Other researchers have had some success in incorporating TiAlN/VN nanoscale multilayers which self lubricates at high temperatures. The V forms the low friction V_2O_5 and $AlVO_5$ oxides[16]. The V containing oxides act as lubricants at high temperature in dry sliding contact [15]. Balzers has had some success with a multilayer system of a hard TiAlN coating and a soft solid lubricant WC/C coating[17]. W forms WO_3 a low friction phase at elevated temperature. Erdemir has suggested several different materials including Mo, W, V and Re that could be appropriate to incorporate into a coating[15]. This combination of hard and soft coating allows for improved chip flow, reduced cutting forces, lowered coefficient of friction and inhibits sticking and welding of the work piece.

1.6 Material Selection

Most development of PVD hard coatings for cutting applications has involved the deposition of materials such as TiN, TiC, ZrN, ZrC, CrN, TiAlN, and others, including combinations in layers, nanolayers, and composites (dispersed phase on a micro- or nano-scale). Most efforts to-date have focused primarily on making coatings that are strong (high hardness), durable (low wear), and resistant to oxidation at high temperatures (~ 1000˚C). More recent research has emphasized the need for toughness as well [4,5], and the drive toward dry machining has pushed researchers to consider how lubricious materials might be incorporated into the coating. One of the few solid lubricant materials to get significant attention is MoS_2. Work with the MoS_2 system has resulted in its being commercialized [6] as a top-coat for a hard coating system in order to maintain low friction. There has been some success, but it is not the answer for all situations,

and according to the present concept, might be more useful if a lubricious phase could be formed in situ as needed, particularly for cutting applications where a top coating would be removed quickly.

Certain metal oxides are also known to be lubricious at high temperatures; however, it is not practical to attempt to incorporate these materials (as oxides) in a reactively deposited nitride coating. Thus, it makes sense to incorporate selected oxide-forming elements in the coating if possible, in order to form lubricious oxides when the contact surfaces experience high temperatures. This auto-initiated response to high friction, high temperature conditions are a primary objective for the research work presented here. Incorporating the oxide-forming elements into the coating will be part of the challenge of making a working self-lubrication coating.

In the selection of the lubricious oxide forming phase at high temperature, we have at our disposal various metals and metalloids such as Re, Ti, Mo, Zn, V, W, and B previously shown to demonstrate low friction at high temperature[15]. Examples of other oxide formers that appear to form viable lubricious candidates include P and S and possibly some low-melting metals (e.g., Pb, Bi, Sn). Boron is attractive because it is known to form boric acid in the presence of oxygen and water, and this has been shown to exhibit very low friction in sliding wear [7]. Certain compounds of phosphorus and of sulfur are known to form excellent boundary lubricants (used as additives in liquid lubrication technology). Combinations of these elements with metals such as Ca (which is also known to form lubricious solids at high temperatures when used as highly-basic additives) can also be advantageous, thus, additional options include the incorporation of pairs of elements (e.g., Ca and S or Ca and P).

The use of these materials in vacuum-based technology such as sputtering (our preparation route of choice) is not generally pursued because of obvious materials accessibility issues (e.g., volatility, toxicity, and extreme reactivity) and the fact that there were easier successes to be gained in the development of harder materials. Numerous questions arise concerning the fabrication of such coatings, some of the process-specific issues are the following:

- One needs compounds (with Mo,B or P, etc.) that are stable in the sputtering environment, and to handling.
- Elements or sputtered/dissociated compounds will be deposited and reacted with nitrogen and/or each other. What compounds will form in the coating, and will the selective oxidation concept work?
- Elements/reaction compounds – what will be the distribution in the coating, and will it be stable?
- The formation of the host phase may be altered by the added elements/compounds. What affect will there be on internal stresses, interlayer adhesion and crystallinity?

We hope to answer some of these questions as we develop a processing strategy for these coatings and understand the tribo-chemistry of dry cutting (and other high temperature wear applications) while attempting development and design of multi-functional coatings.

Our approach:

1. Hard coating “host” structure to provide strength and toughness in a dry cutting environment.
2. A component of the structure that resists oxidation to remain effective at high temperatures.

3. A component of the structure that facilitates dry lubrication in order to enhance performance and tool life, while eliminating the need for liquid lubricants.
4. The right balance of 2 and 3 to ensure optimum functionality of both components.

Figure 2 (a) shows a cartoon representation of our conceptualized coating, with alternating layers of the lubricious oxide forming phase and the oxidation resistant phase. Figure 2 b, shows a conceptualization of the change in the tool/coating surface with use.

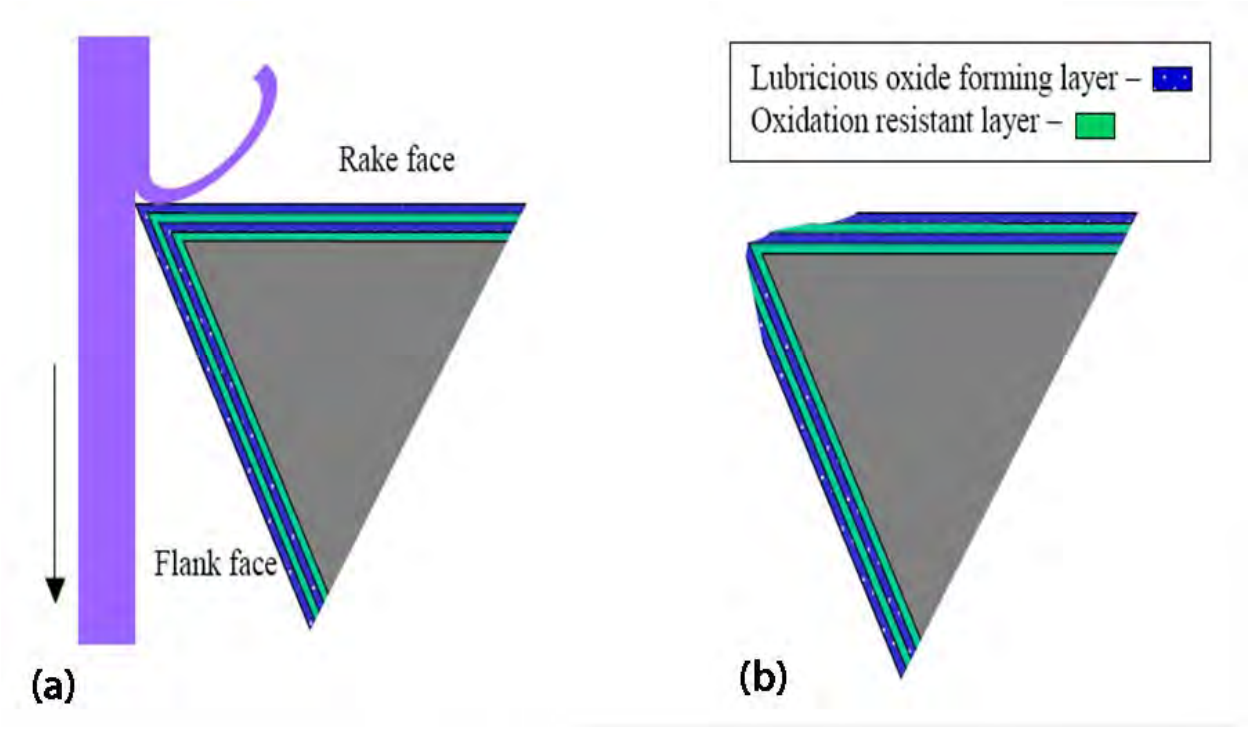

Figure 2. Cartoon representation of multilayered coating on cutting tool (a) shows alternating layers (b) resulting change in tool/coating tip after initial wear.

1.7 The Basic hard coating "host" material system.

The basic intent here is to work with materials in a nanolayered structure that would be hard, tough, adherent, and lubricious at the service temperature (<1000˚C). The basic system of CrN_x and MoN_x to form multi (nano)-layered coatings offers some advantages as a starting point. The phase diagrams of Cr-N and Mo-N show the many different nitrides that can be deposited. The binary phase diagrams of Mo-N (Figure 3) and Cr-N (Figure 4) show that the deposition of many different nitride phases of Mo and Cr is possible and the choice of the phases deposited would dependent on the partial pressure of deposition. The choice of the partial pressure on the other hand will be dictated by the need to optimize the bulk properties of the multilayer coating. Cr is suggested because of its excellent wear (and oxidation) resistance and Mo because of its resistance to oxidation, wear and galling [18-20]. The presumption is that Mo readily forms a variety of different oxides (Figure 5) many of which are known to be lubricious and will therefore reduce the cutting friction and consequently, the heat generated by high-speed contact (relative to a coating without the Mo). Recent work showed that plasma sprayed composites of Cr_2O_3 and MoO_3 benefit from the addition of MoO_3 and exhibit a reduction of sliding friction from ~.4-.5 at RT to ~.2 at 450˚C (self-mated or against Cr-plated discs)[21]. Cr has greater resistance to oxidation (>800˚C) than Mo, and forms a very stable oxide at high temperatures, that is also very hard (>25GPa) and corrosion resistant. The nitrided forms of these metals are very hard (20-30 GPa) and show increases in oxidation and wear resistance relative to the metals. The oxide formation at temperatures above 400°C appears to offer promise for the approach. In our case, added characteristics of the selected materials are that they are both hard phases (~ 20-30 GPa) and they are expected to be immiscible in their elemental states up to 800°C (Figure 6).

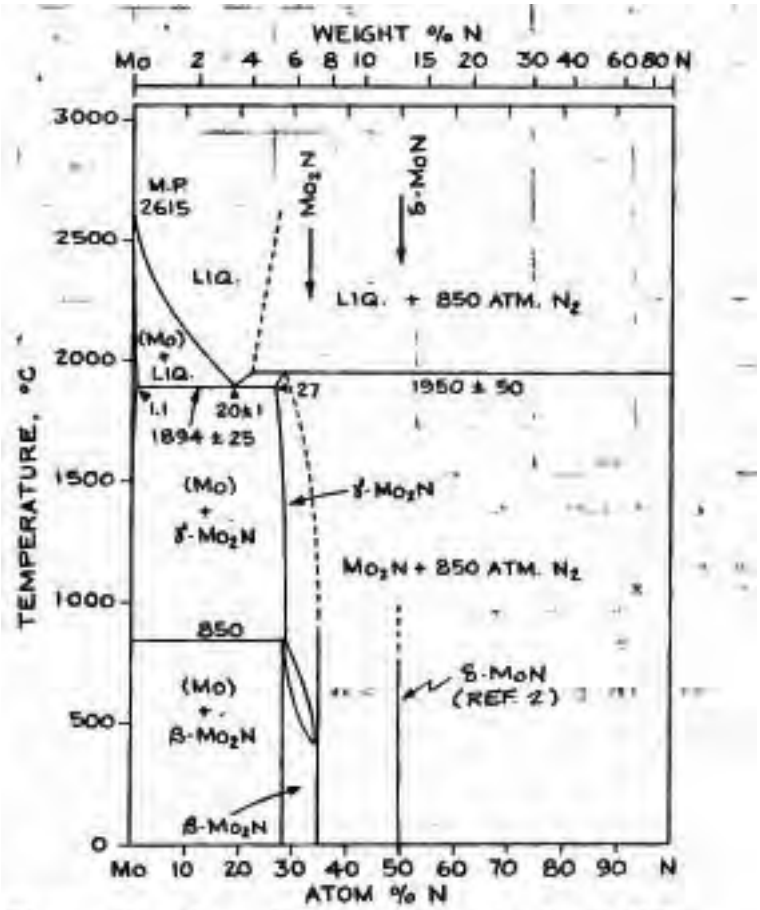

Diagram redrawn from ref. 1 (literature review through 1979); the two forms of Mo_2N are indistinguishable at high-N content and δ-MoN is unstable at N_2 pressures up to 850 atm. However, see ref. 2 which includes δ-MoN and gives congruent M.P. of β'-Mo_2N as about 2000°C at N_2 pressure greater than 1000 atm.

(1) Brewer, L. and Lamoreaux, R.H.
pp 274-277 of "II. Phase Diagrams.", in volume ATOMIC ENERGY REV., SPEC. ISSUE No. 7 ("Molybdenum: Physico-Chemical Properties of its Compounds and Alloys."); L. Brewer, Editor; Internat. Atomic Energy Agency, Vienna, 1980.

(2) Jehn, H. and Ettmayer, P.
"The Molybdenum-Nitrogen Phase Diagram."
JLCM; 58, 1978; pp 85-98.

11/86

Figure 3. Phase diagram of the binary Mo-N.

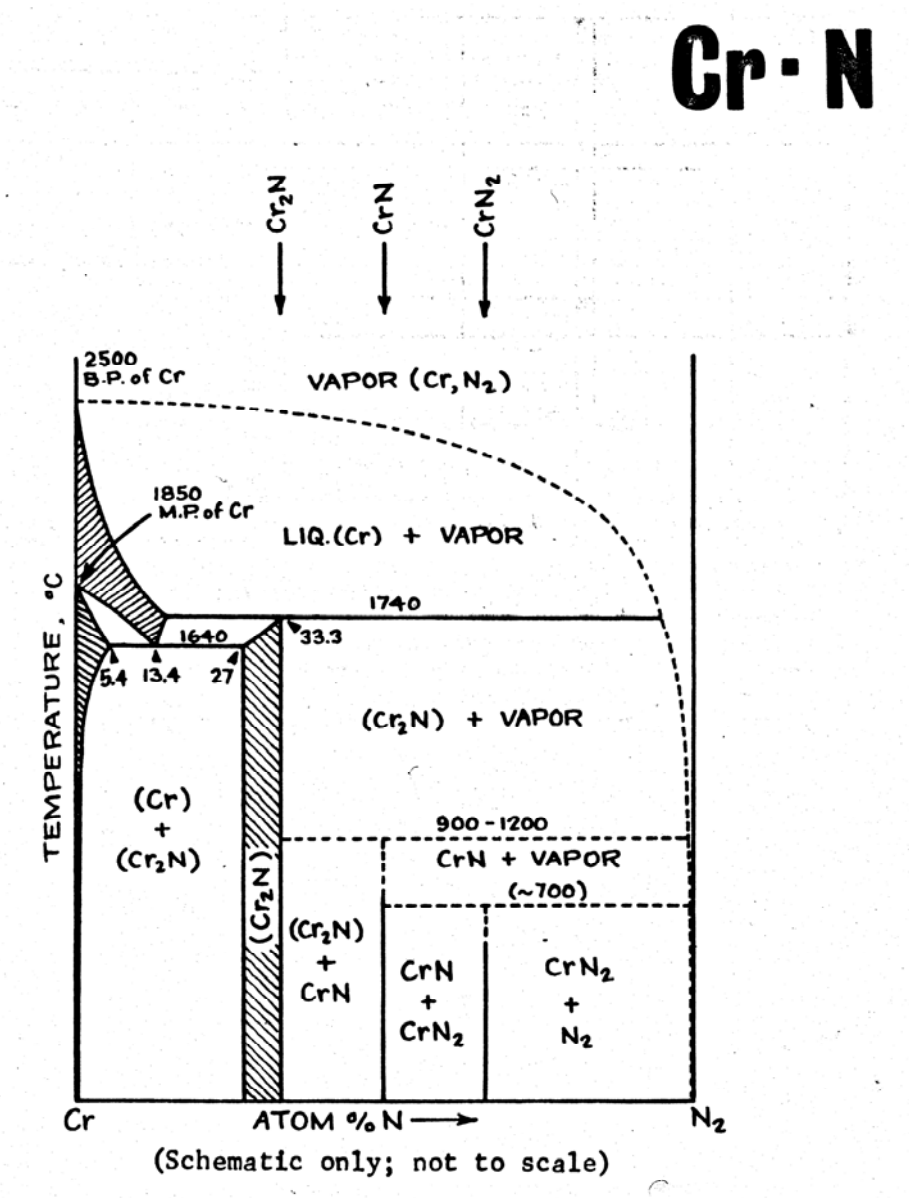

This system investigated under pressures to about 3 atmospheres of argon plus nitrogen. Dissociation temperatures of CrN and CrN depend upon nitrogen pressure.

Diagrammy Sostoianiia Metallicheskikh Sistem; Nauka, Moscow 1971, p 135

Figure 4. Phase diagram of the binary Cr-N.

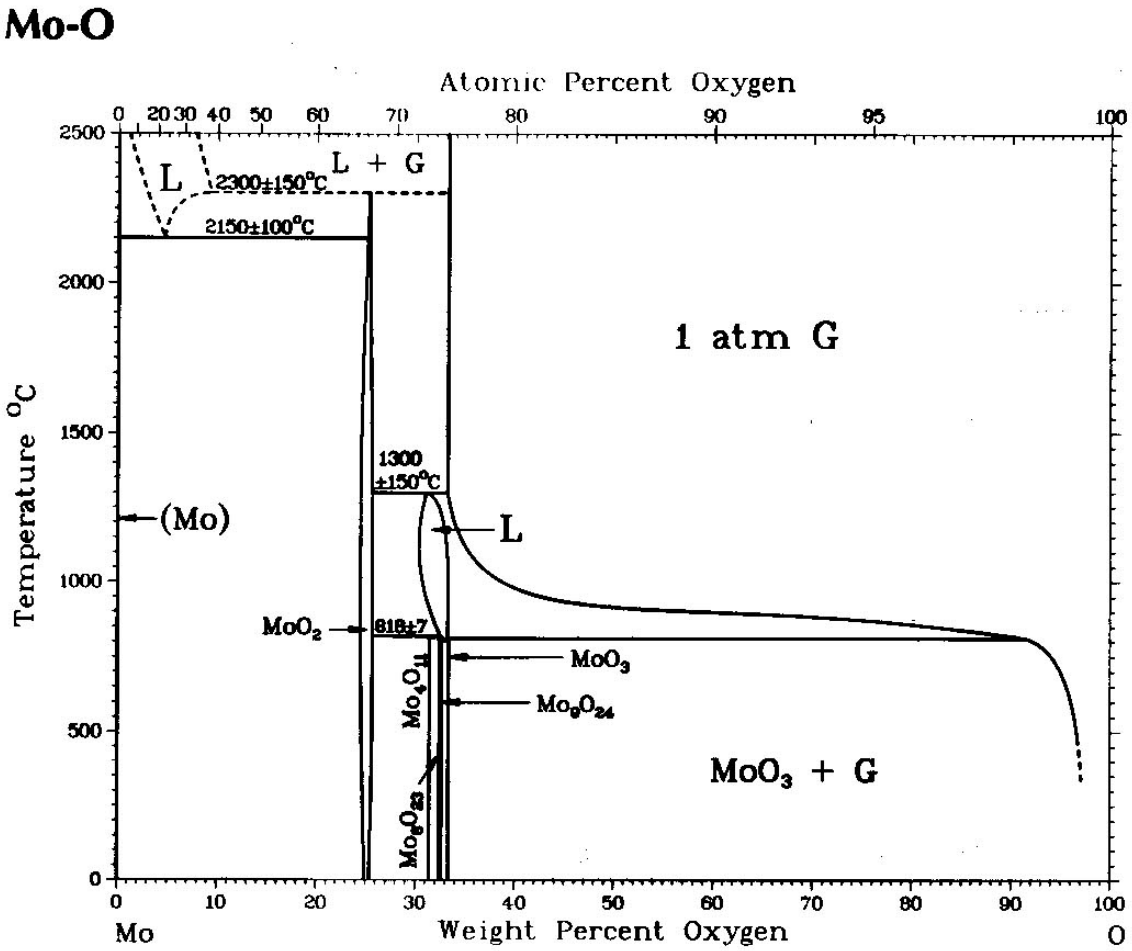

Phase	Composition, wt% O	Pearson symbol	Space group
(Mo)	0	*cI*2	$Im\bar{3}m$
MoO_2	~25.0	*mP*12	$P2_1/c$(a)
		*tP*6	$P4_2/mnn$
Mo_4O_{11}	31.4	*oP*60	$Pna2_1$
Mo_8O_{23}	32.4	*mP*124	*Pc*
		*mP*62	*P*2/*c*
Mo_9O_{24}(b)	32.5	*mC*280	*C*2/*c*
		*mP*70	*P*2/*c*
MoO_3	33	*oP*128	*Pba*2

(a) Or $P2_1$. (b) Might be Mo_9O_{26}

Figure 5. Phase diagram of the binary Mo-O.

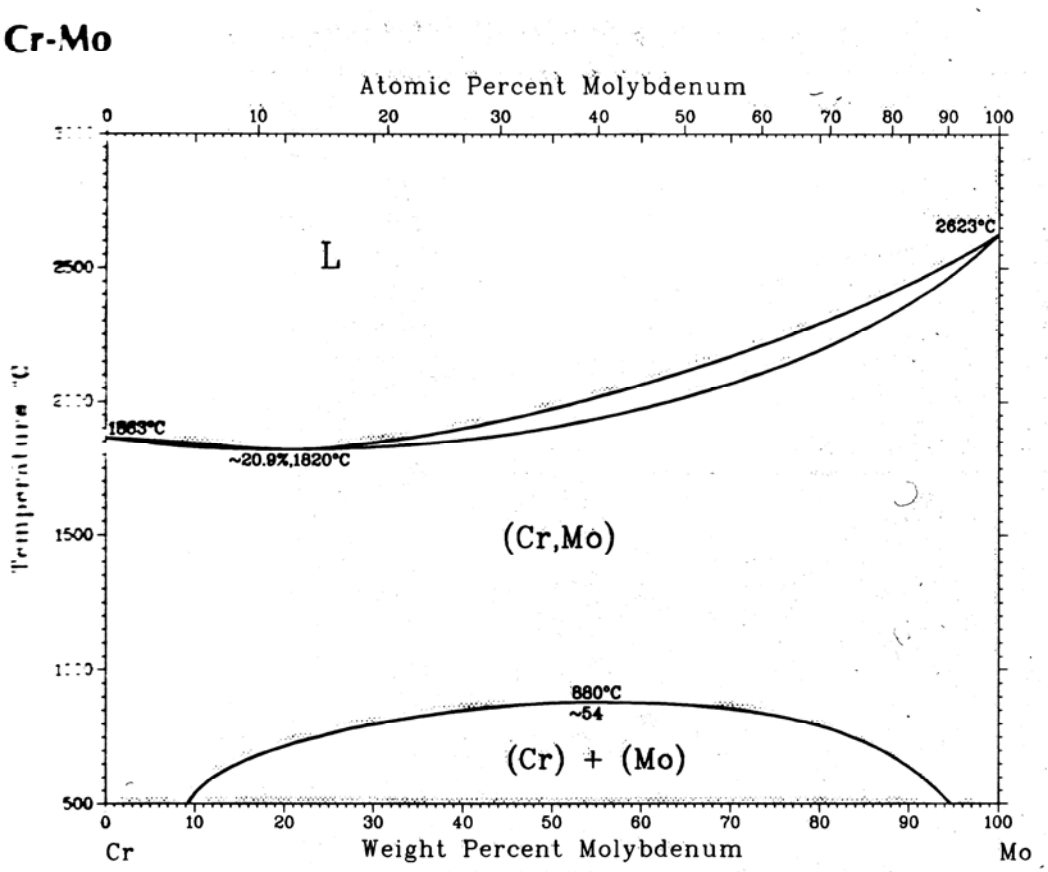

Phase	Composition, wt% Mo	Pearson symbol	Space group
(Cr,Mo)	0 to 100	*cI*2	$Im\bar{3}m$

Figure 6. Mo-Cr phase diagram.

The nanolayered structures would further enhance the toughness of the coatings and help maintain hardness at high temperatures. The hardness enhancements are due partly to Hall-Petch (size) effects, and further enhancement is due to barriers to dislocation motion across interfaces

because of differences in structure and elastic modulus of the two layered phases[22]. (Table 1) shows the crystal structures of the possible compounds that we can synthesis from Cr, Mo and B. The phases to be synthesized will depend on the optimized bulk properties like hardness, residual stress, adhesion etc, and yet be limited by our deposition conditions (we will be depositing both the compounds at the same time in a single chamber). Good adhesion of these materials to cutting tool substrates, as deposited by magnetron sputtering, has been demonstrated for the respective metals and metal nitrides. Indeed, CrN_x coatings are commercially available from several sources, and both metal-nitride systems have been extensively studied.

Table 1. The different compounds that can be synthesized from Cr, Mo and B, with their crystal structures.

Elements/Compounds	Crystal structure	Lattice parameter(Å)
Cr	bcc	2.91
Cr_2N	hcp	a=4.75,c=4.42
CrN	fcc	4.14
Mo-N	fcc	~3.14
β-Mo_2N	tetragonal	a=4.2,c=8.0
γ-Mo_2N	fcc	4.16
MoN	hcp	a=5.74,c=5.62
B	rhombohedral	5.06
h-BN	hcp	a=2.504,c=6.661
c-BN	cubic	3.61

Figure 7 (a), (b) and (c) is a cartoon representation of the some of the possible relative distributions of the proposed oxidation resistant phase and the possible lubricant phase. Figure 7 (d), (e) and (f) shows proposed structure combination of Mo_2N, BN with the oxidation resistant phase CrN. Using these refractory metal nitrides as the basis of the coating structure, it is envisioned that the CrN_x layers can provide the high temperature hardness and oxidation resistance to maintain effective cutting at high temperatures. The MoN_x layers are strong enough

to support the cutting function, but will begin to be sacrificial by forming oxides at a certain temperature-pressure combination.

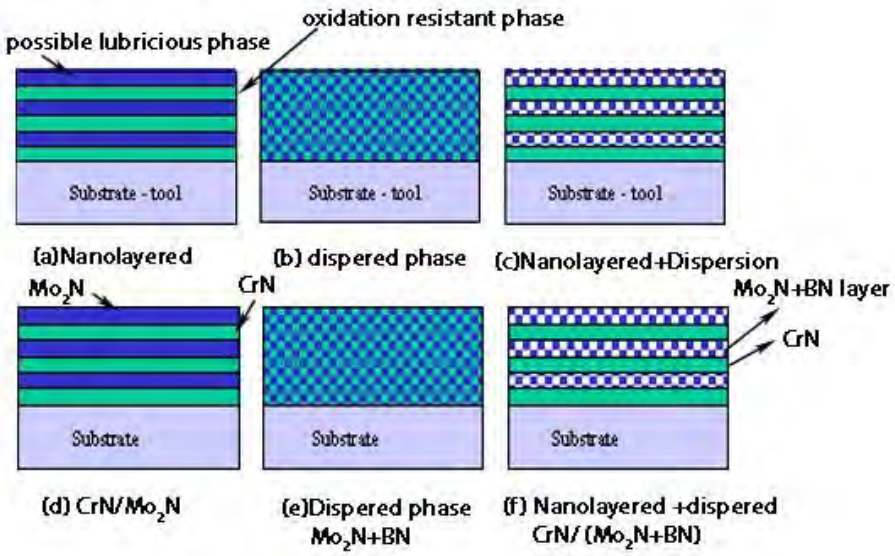

Figure 7. Cartoon representation of the proposed generalized multilayer structure in (a), (b), and (c) while (d), (e) and (f) represents some of the proposed structure/compounds.

The use of MoN_x is a novel concept for this application, but as a layer component in the nanolayered structure, positive use may be made of the reaction. By controlling the nanolayer structure it may be possible to effectively "meter" the Mo oxidation rate. Not only will its effect on the friction of the coating be interesting to study friction, but also on the nano-topography of the coating as it evolves due to the wear and oxidation processes. Our study provides a unique opportunity to observe a "controlled" microstructure response to sliding contact and to investigate the tribology of nano-roughened surfaces in dry sliding and cutting.

MoO_3 forms at about 500˚C and is liquid/gas above about 700˚C. Enhancements (additional lubricious oxides at lower temperatures) to the MoN_x phase performance are a challenge and will be addressed by co-sputtering desired elements in a solid form, such as a Ni or Co(B, P, Ca, etc.) plated source materials (targets), or from targets of stable compounds (e.g., B_4C or InP) where available. We intend to achieve some phase separation through a dispersion of the additions on a nano-scale within the MoN_x layer. The nanoscale dispersion will be assisted by the use of nano-dimension layers. Within the layer, dispersion will be dependent on thermodynamics to some extent and on the energy available to assist atom movement on the growth surface. Since sputtering process temperatures are typically less than about 200˚C, the energy factor is largely influenced by the process conditions such as pressure, substrate bias voltage and target power. These factors combine to control the kinetic energy of atoms and ions impinging on the substrate surface, and thus, the energy available for ad-atom mobility. The next chapter will discuss the sputtering process in detail.

Chapter 2: Deposition and Experimental Techniques

Functionalized hard coatings can be deposited by different routes and this chapter will discuss at length the advantages of the deposition technique of choice: unbalanced magnetron sputtering. This chapter will also dwell into the limitations of prior deposition techniques, some of the incremental technological advancements made in resolving those limitations and some of the future developments to the existing sputter coating technology. Finally I will elaborate on some of the instrumentation details of the magnetron chamber used for depositing the coatings and the experimental techniques used to characterize the bulk properties of the coatings.

2.1 Sputtering

Sputtering is a deposition process for materials in which charged ions bombard the material to be deposited and target atoms are ejected and deposited on a substrate. A schematic representation of one of the early sputtering system is shown in (Figure 8). W. R. Grove[23] when reporting on the electro-polarity of gases inadvertently ended up making the first pulsed sputtering system. This system is represented in Figure 9. Essential to any sputtering system is a vacuum chamber typically pumped down to 10^{-6} or 10^{-7} Torr and backfilled with an inert gas, typically argon. The idea behind working in lower pressures is to ensure a mean free for the sputtered atoms to reach the target and to ensure proper plasma generation. A glow discharge plasma is ignited by applying large negative potentials on the targets relative to the anode. The anode is usually any grounded surface within the vacuum like the chamber walls, ground shields and at times the substrate and its holder. The plasma initiates when an ionized gas particle is accelerated towards the target by the applied potential difference. Secondary electrons are ejected from the surface of the cathode, which in turn ionize more Ar gas which ultimately can be made self sustaining.

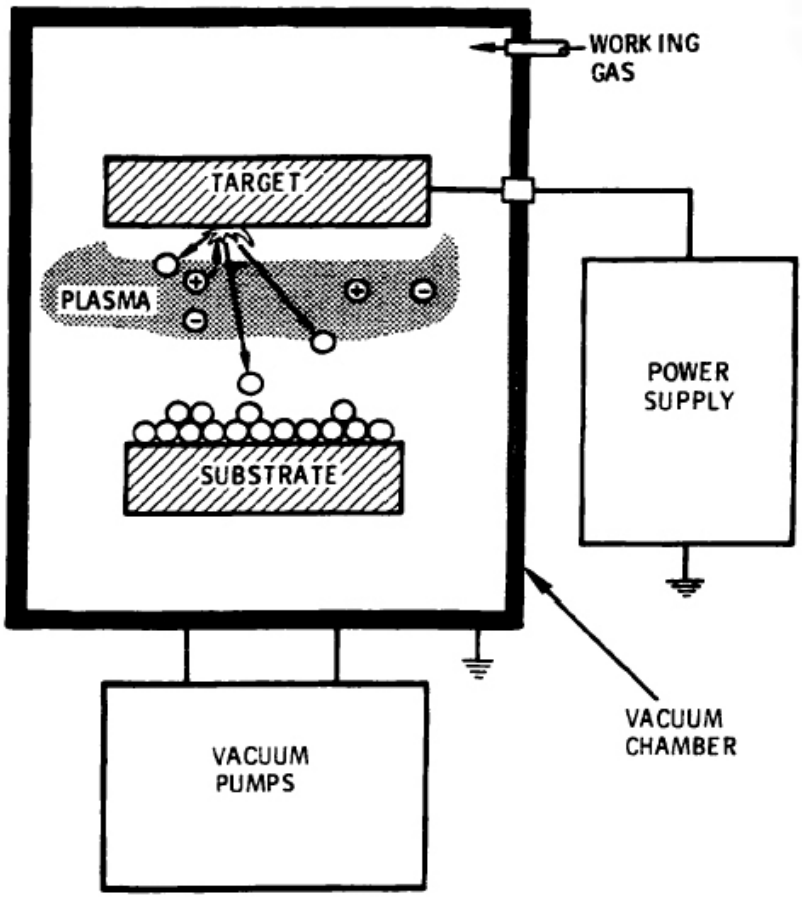

Figure 8. Schematic diagram of a simple sputtering system (Thorton 1982).

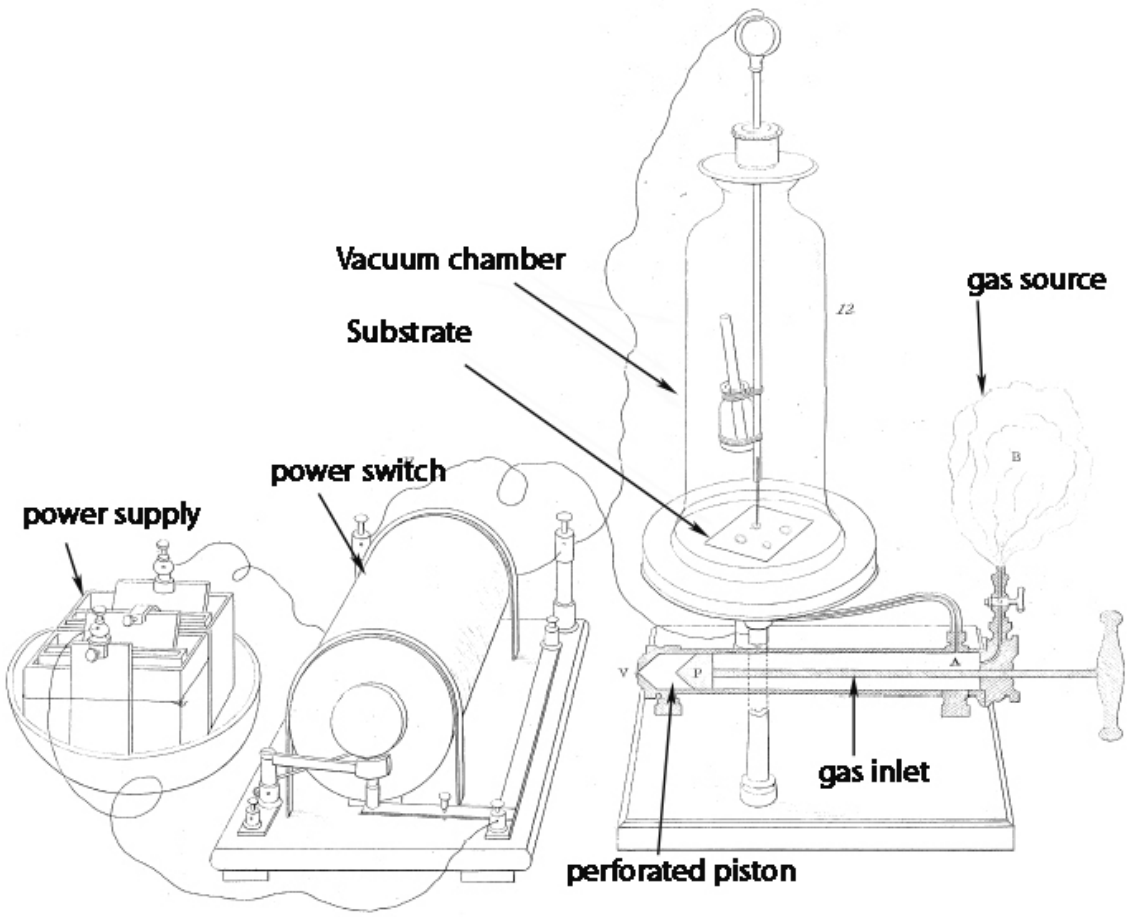

Figure 9. A system demonstrating electro-chemical polarity of gases, that was also the first pulsed sputtering source (Grove 1852).

Ionized inert gas atoms in their collisions with the cathode transfer a significant part of their energy as heat; however parts of the energy are transferred to the cathode atoms as kinetic energy. These energetic atoms are then ejected from the cathode and are transferred to a substrate.

2.2 DC and RF sputtering

Direct current sputtering is the simplest sputtering process in which a simple voltage difference is applied between two electrodes. If the voltage difference is high enough a break-down potential is achieved and the gas phase is ionized, leading to charged gaseous species bombarding the cathode and leads to material being sputtered onto the anode. The voltages applied are anywhere from 100V to the kV ranges and the gas pressures are ~100 mTorr. A major draw back of such a system is the build up of charge, when depositing non conducting phases, on the cathode and the sputtering yield decreases with time. One of the ways to avoid this is to alternate the potential on the target and substrate. Applying an alternative current with low frequencies leads to DC sputtering of both surfaces, since the ions and the electrons in the plasma are mobile. On further increasing the frequency above 50 kHz the heavy ions can no longer move with the switching potential, while the electrons can continue to neutralize positive charge build up.

2.3 RF sputtering

Sputter deposition via rf power is particularly useful due to its ability to enhance ionization efficiency of the plasma. The electrons in the plasma gain energy from the rf field (alternating field) through in-phase oscillations. This enhanced ionization efficiency thought the advent of rf power has allowed industry to coat many more conducting and insulating materials more efficiently. The use of an ac power supply opens the electron trap, critical to high sputter rates, once each cycle. This greatly decreases the deposition rate by up to 50% or even higher depending on the system geometry and at times gives rise to substantial substrate heating. The charged species are subjected to oscillating electrical fields that accelerate and move them in

opposite directions every half cycle. The ions, unlike the electrons, cannot respond fast enough and hence both the cathodes become negatively charged with respect the positive ion space charge (their transit time > 1/f frequency of the r.f plasma). With increasing frequency of the power source, there is a reduction in the minimum operating pressure, while at constant pressure the discharge impedance decreases. These two observables from the plasma lead to the conclusion that ionization efficiencies per electron increases. One major disadvantage of rf-sputtering is the cost of the power supplies and the need for matching networks. Matching networks are necessary because rf-generators are designed for purely resistive loads typically of the order or 50 Ω, but typical rf discharges have much higher and more complex impedances. Reflected power on coupling the rf-power supply with a matching network should be typically less than 1%.

As a hybrid between rf-sputtering and dc-sputtering, pulsed dc power supplies have been developed. Pulsed dc supplies have a large negative voltage pulse, during which sputtering is done, followed by a relatively small positive voltage pulse. The positive voltage gets rid of the charge accumulated in the prior negative cycle. These power supplies generate a pulsed dc signal with a frequency which can be varied from 1- 300 kHz. The rate at which pulsing occurs is critically important because the oxide film on the surface of the target needs a certain amount of time to discharge. This technology has allowed industry to venture into reactive sputtering of insulating materials. The addition of a magnetic field to increase the yield of secondary electrons has led to magnetically enhanced sputtering which is discussed in the next section.

2.4 Magnetron sputtering

Magnetron sputtering, as the name suggests, is a magnetic field assisted variation of sputtering invented in the early 1960's by Kay [24]. To implement magnetic field assisted sputtering, magnets are placed behind the target to set up a magnetic field in a configuration similar to the one shown in Figure 10 (a). The magnetic field $\vec{B}$ exerts a force on the secondary electrons in the $-\vec{v}x\vec{B}$ direction. Figure 10 (b) shows a cross section of a magnetron cathode with a graph showing the steep drop off in magnetic field with distance from cathode. The secondary electrons are effectively trapped following a helical orbit close to the surface of the target.[25, 26] These electrons in the process collide with Ar atoms leading to a much higher ion density near the target than can be achieved without the magnetic field. This confined ion current is responsible for the characteristic erosion "race track" observed in planar magnetrons. The increased ionization efficiency achieved in the magnetron mode allows the discharge to be maintained at lower operating pressure (typically, 10^{-3} mbar compared to 10^{-2} mbar) and lower operating voltages (typically -500V compared to -2 to -3 kV) than is possible in the basic sputtering mode. In conventional magnetrons the plasma is confined to the target region. A region of dense plasma typically extends ~50mm from the target surface. Film growth on substrates in this region will be subjected to ion bombardment. The ion currents drawn at the substrate is generally insufficient to modify the structure of the film if the applied bias is too high. Applying a negative bias can increase the energy of the bombarding ions. This however, leads to increased film stress and defects and is detrimental to the overall film properties. These issues can be overcome without introducing excessive intrinsic stresses at relatively low energy (<100

eV) ions is generally preferred [27, 28]. These conditions can be provided by an unbalanced Magnetron.

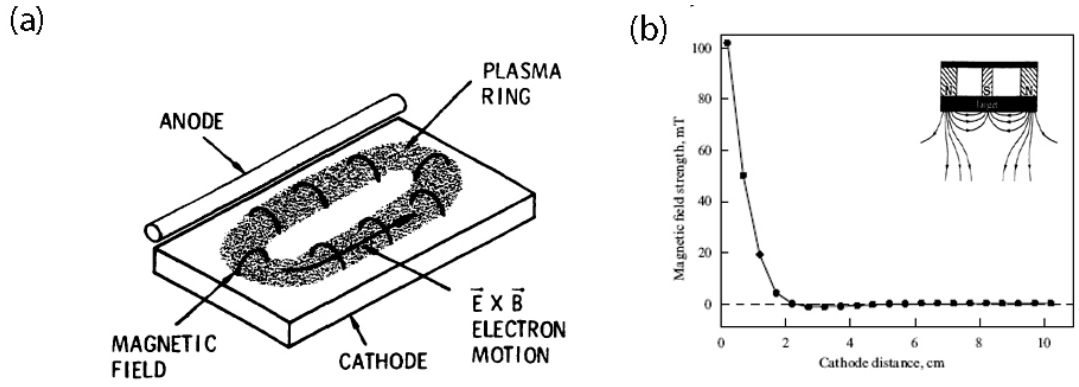

Figure 10. (a) Shows the formation of the race track near the cathode (after Windows, 1986) (b) Shows an unbalanced magnetron with a graph showing the drop of magnetic field strength with distance from cathode (reproduced from Kastanov,2007).

Windows and Savvides[29] used stronger magnets around the perimeter of the target and weaker magnets in the centre which is referred to as an unbalanced magnetron. The additional field lines extend out from the target towards the substrate as shown in Figure 10(b). These additional field lines form an electron trap in the vicinity of the substrate enhancing the ion density near the depositing film. The ions can then be used to bombard the growing film, enhancing its packing fraction and enhancing its mechanical properties. The plasma is no longer strongly confined to the target region but is also allowed to flow out towards the substrate. This allows extraction of high ion currents from the plasma with relatively low bias on the substrate. Substrate ion currents an order of magnitude higher than a conventional magnetron can be routinely generated when using an unbalanced magnetron. In dual cathode magnetrons two types of configurations are possible.

The magnetrons can be set up in a mirrored or closed field configuration, Figure 11 (b). In arrangement the magnetic fields end up canceling each other out at the substrate, assumed to be placed mid-way between the cathodes. In this configuration some of the field lines are directed towards the wall, secondary electrons following these lines are lost, resulting in a low plasma density in the substrate region. In the opposed case, the magnetic field closes around the substrate, leading to a higher degree of ionization near the substrate Figure 11 (b). Operating in this mode results in an ion-to-atom ration incident at the substrate some 2-3 times greater than that obtained under the same conditions in the mirrored or single unbalanced magnetron configuration.[27]

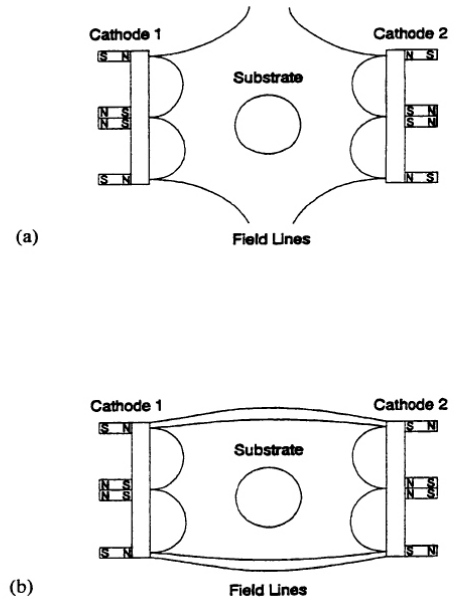

Figure 11. Schematic representation of magnetic field lines (a) mirrored (b) opposed unbalanced (Spoul 1990).

2.5 Reactive sputtering of nitrides and oxides

Compounds of interest can be deposited by sputtering from a target within a reactive environment. Reactively sputtering compounds with the targets in their elemental states achieve a higher deposition rate and is typically much cheaper than sputtering the compounds themselves. When depositing nitrides, a small amount of nitrogen is added to the working gas, the sputter yield of the metals decrease significantly because of target poisoning. Figure 12 can be taken as a generic example of a reactively sputtered compound. The regions of low oxygen fraction show a high deposition rate., while with increasing nitrogen content the deposition rate decreases significantly . This can be traced to “poisoning” of the target with the surface being covered with the TiN[30] which has a lower sputter yields than the metals. The sputter yield of the target varies between elements and also depends on the energy of the Argon ion impinging on the target surface. Figure 13 shows the effect of increasing the Ar ion energy on the sputtering yield of Ti, Nb, Co, Ta and Th. With increasing Ar ionization energy the sputtering yield finally plateaus out. Higher energy Ar ions tend to imbed themselves in the target and yield no appreciable increase in sputtering, so this trends is shown by most other metals during sputtering. At low partial pressures of deposition, film composition is ideal, while higher partial pressures are plagued by low sputtering rates. The ideal operating point is between these two extremes and past attempts have focused on controlling the flow of reactive gases in order to maintain the partial pressure within this region. This has proved unsuitable however due to inherent instabilities. Figure 14 shows the hysteresis curves of TiN reactive sputtering.

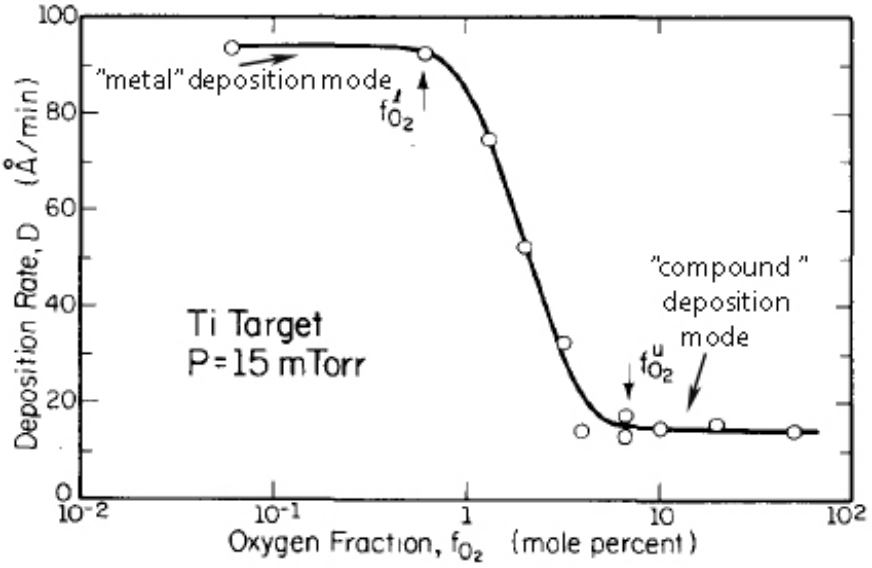

Figure 12. Plot of deposition rate vs. mole % oxygen in the Ar, O_2 discharge (reproduced from Wu, 1079).

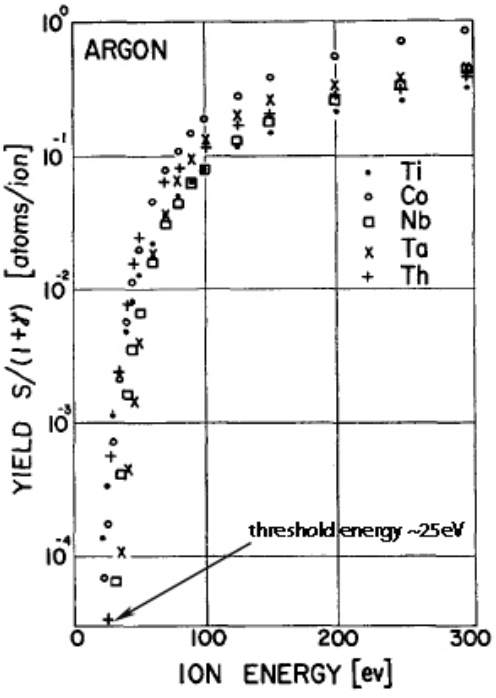

Figure 13. Experimental sputtering yield data vs. Ar+ ion energy reproduced from Stuart, 1962.

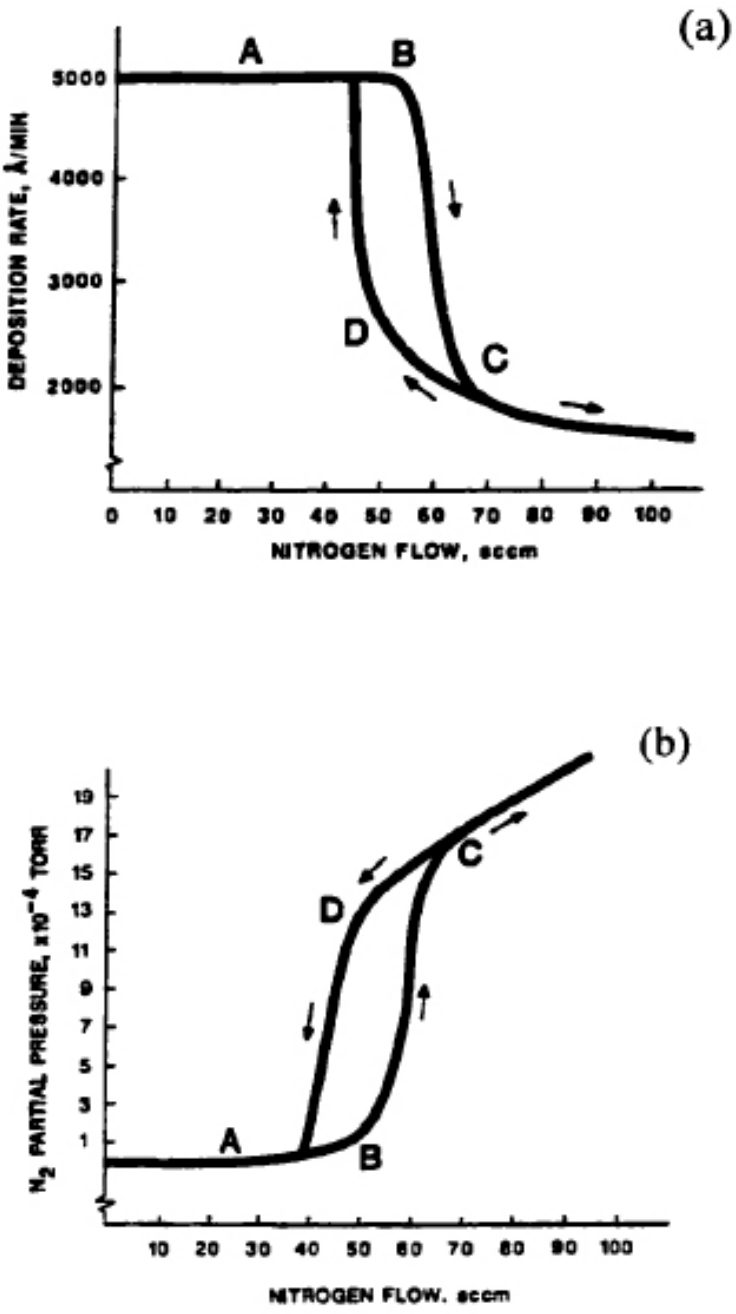

Figure 14. Hysteresis curves of reactive sputtering Ti showing the effect of partial pressure of nitrogen on (a) deposition rate (b) nitrogen partial pressure (Sproul, 1990).

Point A is the stage at which nitrogen is introduced into the chamber, at point B the nitrogen atoms which results from the dissociation of N_2 molecules, are being consumed by the Ti atoms. Point B to C represents the region where the nitrogen content in the Ti increases. Beyond point C is the stoichiometric films and further increase of N_2 leads to target poisoning, which is extremely undesirable. Operating between points B and C leads to the highest sputtering rates and is a desirable region to operate in. The Figure 14 shows how small changes in flow lead to large changes in the partial pressure of nitrogen. This requires an active feedback control of the gas, usually using the partial pressure of the reactive gas or other process parameters as the feedback signal. The primary objective in implementing any strategies for high-rate metal/gas reactive sputtering is to return the process back to its high sputtering rate condition.

- Partial pressure control works by modulating the gas flow rate , while monitoring the partial pressure of the reactive gas via mass/optical spectrometry. With low response time of the feed back loop, there are no forbidden partial pressure operation zones.
- Target voltage control is an indirect method dependent on the fact that target voltage (when operated in constant current mode) is dependant on the partial pressure of the sputtering process. The voltage of the target is thus used as a feedback signal for the gas flow controller. Efficiently working target voltage based controllers require peizoelectrically driven gas flow controllers rather than the normal thermal gas flow controllers. The utility of this technique is related to whether secondary electron emission of the oxide or the nitride is higher or lower than the metal and whether or not

the target voltage is a unique function of the partial pressure. This technique works for Al_2O_3 but not for TiO_2.

- Glow discharge optical emission spectroscopy is an extremely powerful tool for control and monitoring of industrial processes. An optical light signal from the plasma is passed through a monochromator or monochromatic filter. Figure 15 shows a typical Intensity vs. optical emission wavelength plot of Ti deposition. The insert in Figure 15 shows how the intensity drops with increasing partial pressures of oxygen. The level of intensity of the signal at a specific wavelength is proportional to the degree of target poisoning. The signal is essentially at the speed of light, and combined with the quick electronics offers lower response times of the system, which leads to good control. The intensity is also dependant on the number of ions in the plasma and hence the signal has to be calibrated to represent physical quantities such as partial pressure or target poisoning. Some of the other alternative ways of accomplishing good feed back control is via mass spectrometers, optical emission spectrometers or plasma emission monitors.

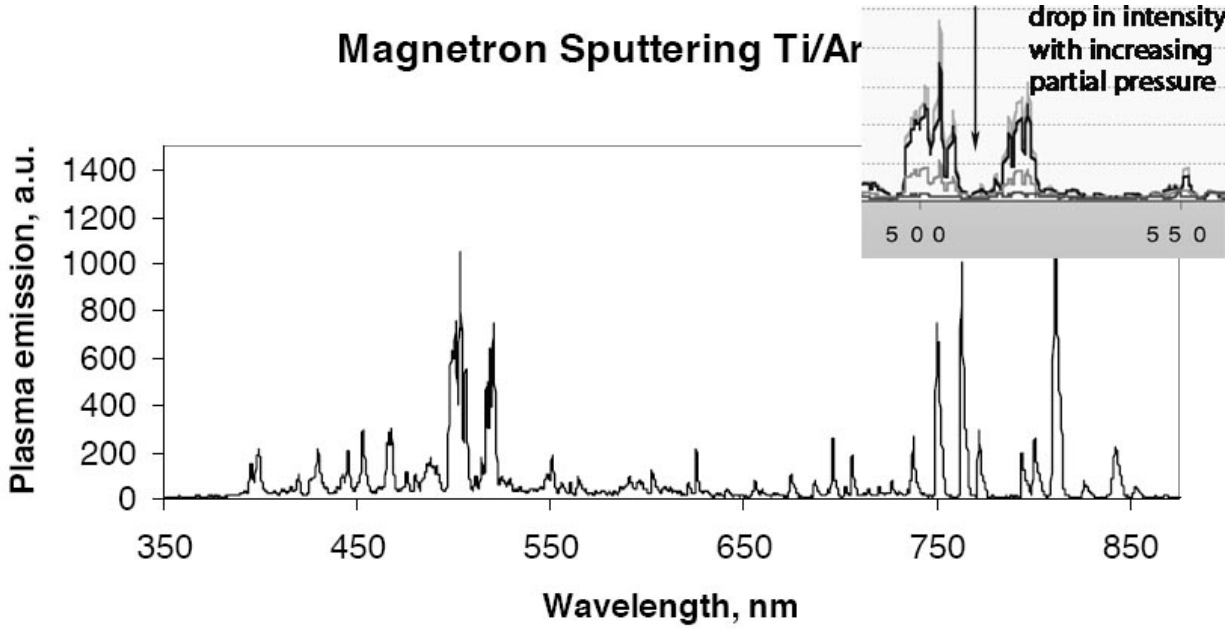

Figure 15. Characteristic plasma spectrum monitored by the GD-OES.

2.6 High power impulse magnetron sputtering.

This method of sputtering utilized high power densities of the order of $kWcm^{-2}$ in short impulses of tens of microseconds at low duty cycles of <10%. The ionization degree of the metal vapour is a strong function of the peak current density of the discharge. At high current densities, sputtered ions with charge of 2+ and higher up to 4+ can be generated. Typical magnetron plasma sources produce mainly sputtering gas ions reaching a typical charge carrier concentration of 10^9 cm^{-3}. HIPIMS can generate a high density plasma [31] of the order of 10^{13} ions cm^{-3}. This enhances secondary ion emission. Figure 16 (a) shows the effects of high power pulsing on the increased discharge voltage and Figure 16 (b) shows the Cr^{2+} ions, a higher ionized species present due to the higher current densities. Sputtering of Ti produces 4+ ionization.

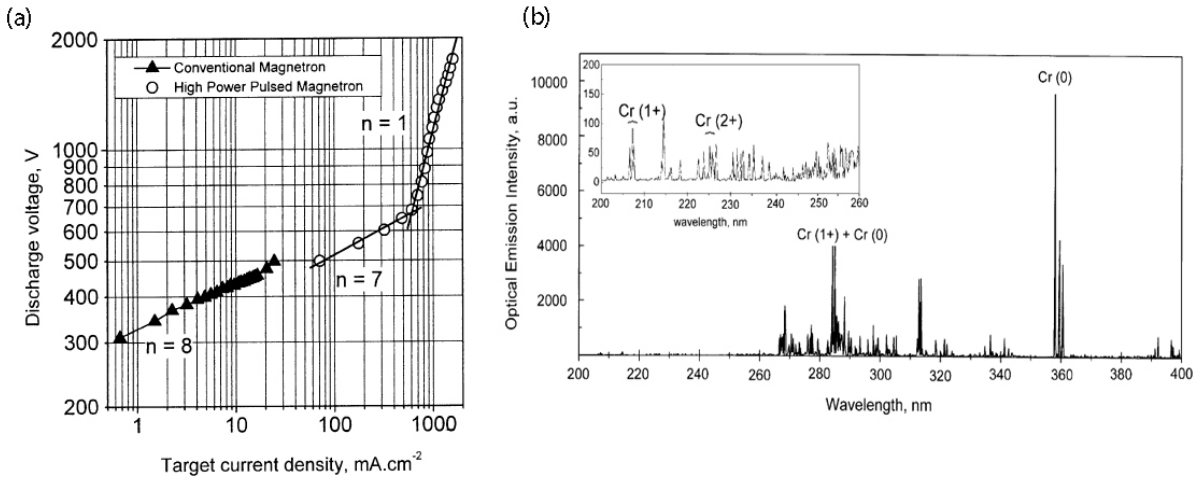

Figure 16. Effects of high pulse discharge on Cr sputtering in Ar atm at a pressure of 3 mTorr (a) I-U characteristics of the pulsed discharge. The component n of the power law I=KUn (b) Optical emission of the high power pulsed sputtering of Cr in an argon atm. The two fold and one fold ionization of the Cr was observed in the dense region of the magnetron. (after Ehiasarian,2002).

2.7 Effect of bias on film growth

Any material growth process is heavily influenced by the energy available for samples to grow. Specifically in sputter deposition the energy of the depositing atoms, the energy of the ions bombarding the surface and finally the temperature of the substrate all heavily influence the bulk properties and the phase of the deposited films. The substrate temperature is generally thought of as a homologous substrate temperature Ts/Tm, where Ts is the temperature of the substrate and Tm is the temperature of melting of the film. Thornton[32] and Messier[33] in their seminal work have represented these process, structure relation in the form of a structure zone model. Figure17 shows the structure zone model (SZM) which was constructed from observations of the microstructure of metallic thin films. The deposited structures were separated into four zones labeled I, II and III. The boundaries of these zones are dependant on the working gas pressure

and homologous substrate temperature. Zone I consists of a voided columnar microstructure resulting from shadowing by adjacent columns. Since the substrate temperatures were low, deposited atoms lack the mobility necessary to from a dense microstructure. At higher working gas pressure, the zone I microstructure persists at even higher temperatures due to the lower energy of the deposited atoms and bombarding neutrals which are reflected from the sputtering target surface. The reduced energy is due to the increased collisions within the plasma, which is proportional to the working gas pressure. At low Ts/Tm < 0.3 the deposited adatom do not have enough energy to move around on the surface of the film. Zone T the transition zone is characterized by densely packed columnar grain structure. Densification occurs due to the bombardment Ar ions and reflected neutrals, however the bulk diffusion is still limited which prevents extensive growth of these grains. The Zone II, is a higher energetic region where the adatom diffusion is sufficient so that grain faceting and extreme surface roughness is evident. Ts/Tm >~0.5, is the region of zone III where there is sufficient energy for the adatoms to move around on the surface and bulk and form its most stable structure at that temperature. This diffusion dominated process causes recrystallization and grain growth leading to large equiaxed grains. Although Thornton developed this model for the case of crystalline metallic films several more reports have linked its applicability to amorphous and crystalline ceramic films as well[34, 35]. The application of bias on the substrate, ions that are extracted from the target and the plasma are accelerated towards the depositing film and serves as an additional energy contribution to surface adatoms. This bombardment favours the formation of the T zone structure as shown in Figure 18.

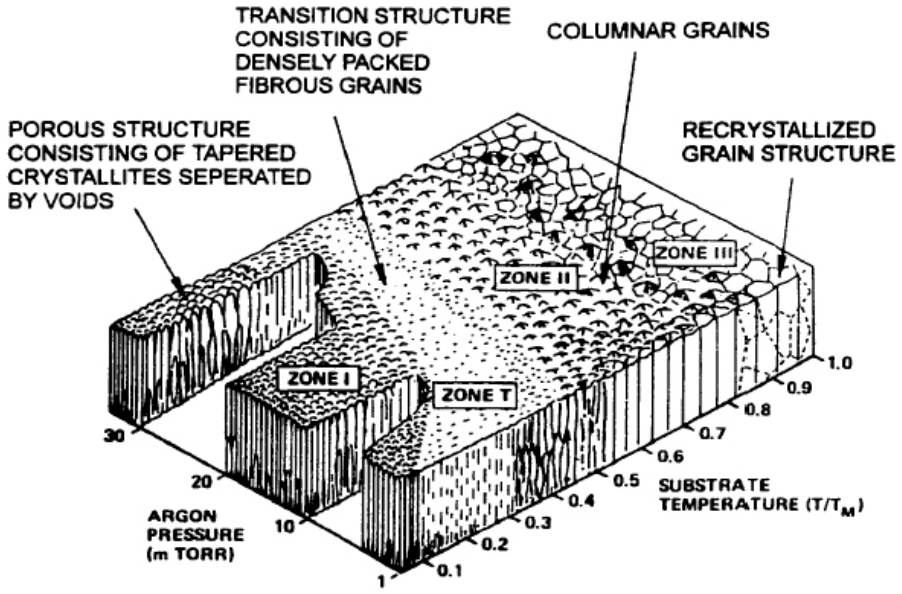

Figure17. Structure zone model of thornton showing the influence of working gas pressure and substrate temperature on the microstructure of the deposited thin film.

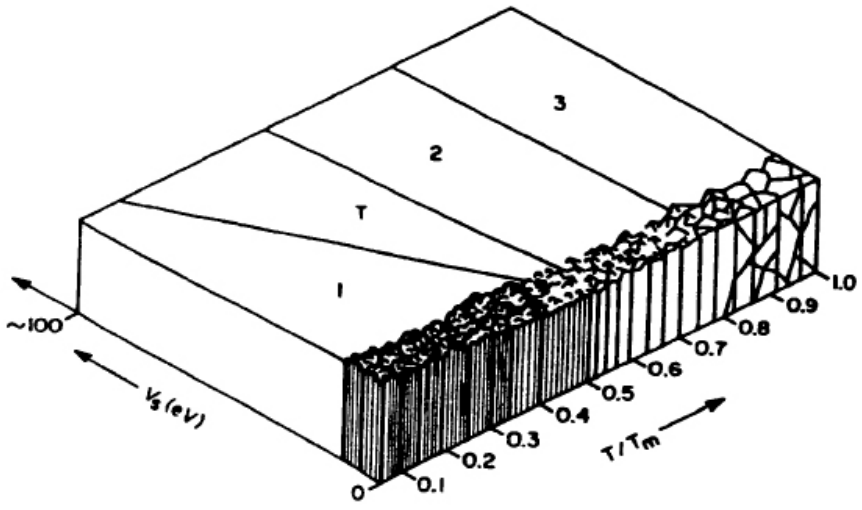

Figure 18. Revised structure zone model incorporating the influence of substrate bias reproduced from Messier 1984.

Increasing the negative voltage or energy of the bombarding ions serves to shift the zone I-zone T boundary to a lower homologous temperatures due to enhanced surface mobility. In depositing hard coatings such as ours we will like to operate in zone T and so it is critical to optimize bias conditions when depositing.

Figure 19 shows the effects on lattice parameter, grain size and hardness of $Ti_{0.5}Al_{0.5}N$ films due to increasing bias. Figure 19 (a) shows lattice parameter increase associated with residual stress increase in the films. Figure 19 (a) also shows the effects on increasing bias on the full width at half-maxium (FWHM) values of the X-ray peaks. The increase in FWHM at lower bias is due to smaller grain sizes, see Figure 19(b), while at higher bias the broadening is due to increase in structural defects and/or increase in micro-strain due to increased bombarding[36]. (Figure 19 (c) shows the increase in hardness due to substrate effects. At low bias the films have an open-voided structure and cannot support load and hence shows low hardness values. The higher hardness at higher bias conditions can be traced to the increase in substrate bias that causes denser structures and generally compressive residual stresses. Defects include point and line defects and Ar gas getting imbedded in the coating.

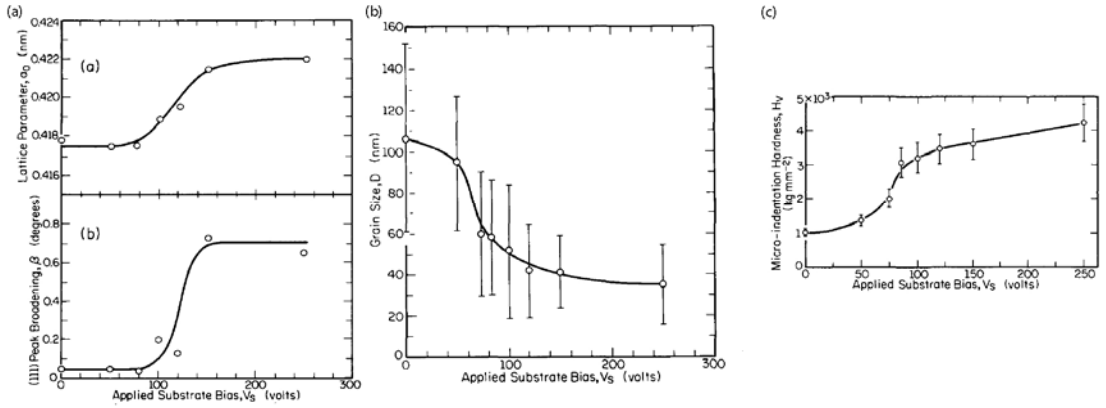

Figure 19. Affect on $Ti_{0.5}Al_{0.5}N$ due applied negative substrate bias (a) lattice parameter effects on lattice parameter and the (111) peak (b) bias effects on average grain size (c) bias effects on hardness of the coating (reproduced from Hakansson,1987).

The magnetron sputtering chamber used for sputter deposition of our coatings is discussed in the next section in the following section. The experimental details of substrate and machines and techniques used will also be discussed.

Experimental setup

2.8 Coating chamber

The magnetron chamber that was used for our coating deposition has a base pressure of $2x10^{-7}$ Torr is shown in Figure 20. The main chamber is initially pumped down by an Alcatel (2033 type) roughing pump then finally pumped down using cryopumps. Figure 20 shows the magnetron chamber equipped with a high-vacuum load-lock which was used to eliminate contamination and excessive pump down time during sample loading. The load-lock and the main chamber are both backed by CTI-8 cryo pumps. A MKS 252 throttle value allows us to control the pumping rate of the cryo pump by opening or shutting the throttle valve. The main chamber has two vertically mounted 12.8 x 40.6 cm planar magnetron cathodes that are facing each other on opposite sides of the substrate holder and 10cm from the substrate. The substrate

holder is a 14cm dia x 42 cm tall hexagonal substrate holder that shadows each target from depositing on each other.

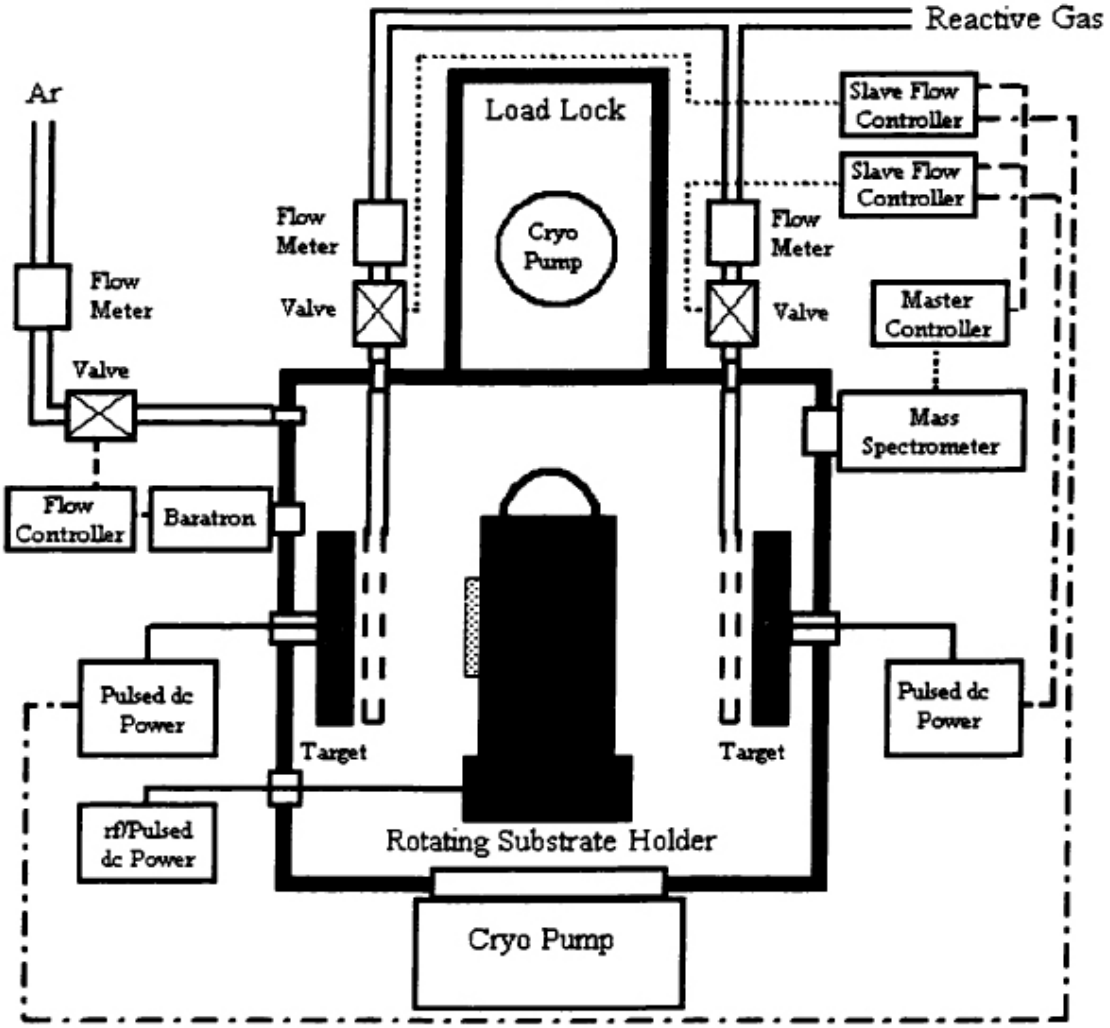

Figure 20. Schematic diagram of the dual opposed unbalanced magnetron sputtering system used for coating deposition.

The substrate holder can have a rotation speed up to 15 rpm which allows us to control the bilayer periodicity of our multilayers. The targets we used were Cr, B_4C, Mo and a composite target of Mo and B_4C. Two Advanced Energy MDX 10kW DC power supplied outfitted with

Advanced Energy Sparc-le V arc suppression units were used to power the targets. The Sparc-le V units generated a pulse as high as 100kHz having a 45 μs negative voltage region followed by a 5 μs positive voltage region having an amplitude of 20% of the negative voltage as shown in Figure 21. The settings of the Sparc-le were varied with target materials and reactive gas to maximize deposition and minimize arcing. An AE-RF XII RF generator can be used to apply a bias to the substrate. MDX magnetron drives with a 10 kW power limit provides drive power to both cathodes. Mass flow controllers are linked to MKS type 260 gas controllers that displace on MKS 261 display. A MKS Baratron® pressure manometer with maximum pressure range of 1 mTorr monitors the net pressure of the chamber during operation by providing feedback to an MFC to maintain constant pressure during sputtering by adjusting Ar input/flow.

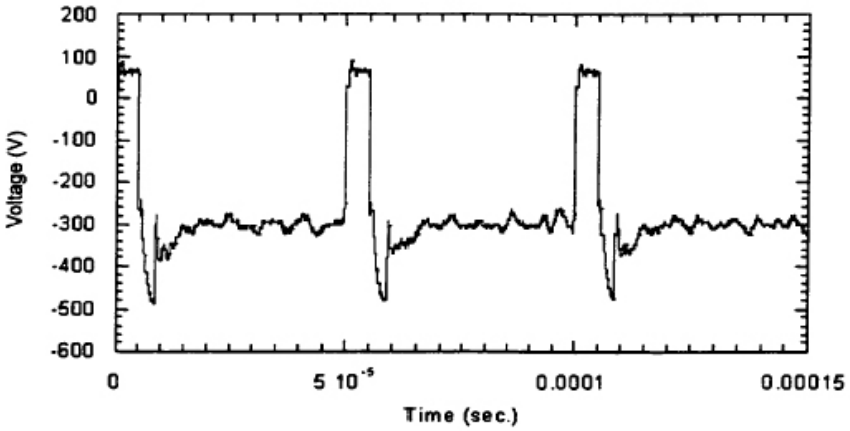

Figure 21. Pulsed DC waveform used to power the sputtering cathodes having a frequency of 20khz, reverse time of 5 μs and a reverse recovery voltage of 20%.

2.9 Substrates used and sample preparation before deposition

The substrates used were single crystal silicon (100) wafers, single crystal (110) sapphire wafers and polished M50 or M2 tool steel. Prior to deposition the substrates were sequentially cleaned in an ultrasonic bath with methanol and isopropyl alcohol. On loading into the chamber the substrates were sputter cleaned in 4mTorr of Ar at an RF power of 1 kW, for 10 min. The coating thickness is 1-2 μm in our test samples while our drill bits have 4 μm of coating. In cases where residual stress measurements were to be made, samples were cut from silicon substrates so that their length to width ratio was ~10:1. The tool steel substrates were cut from 1inch diameter rods into 1 inch x0.5inch sections. They were polished to a 10 nm roughness using standard steps of wet polishing procedure.

2.10 Thermal Gravimetric Analysis

A thermal gravimetric analyzer was employed in this work to measure the weight loss/gain of a sample upon annealing. Samples were placed in a platinum pan hanging on a microbalance inside the furnace. The microbalance was zeroed prior to use. The weight of the sample was monitored throughout the duration of the anneal, and the weight loss/gain was computed.

2.11 Nanoindentation hardness measurement

Hardness and elastic modulus were measured using a UMIS ultra-microindentation system fitted with a Berkovich diamond tip. This instrument has a displacement resolution of 1 nm and a force resolution of 0.01 mN. During the indentation test, the sample is loaded at a rate of 0.02-0.1 mN/s (depending on the maximum load), held for 100 seconds at the peak load to allow time-dependent plasticity effects to diminish and then unload. The maximum load is chosen in order to produce a maximum penetration depth of less than 10% of the total film thickness to minimize

the substrate effects on the measured hardness of the coating. Typically indents depths were in the range of 100 nm and were tested at two different loads with ten indents at each load spaced 20 μm apart. Data is output in the form of a load displacement curve after which a correction to the tip dimension is applied. Hardness and elastic modulus can be determined from the load displacement curve by following the method of Oliver and Pharr[37, 38].

Hardness is defined as

$$H = \frac{P_{\max}}{A} \qquad (1)$$

where the $P_{\max}$ is the peak indentation load and A is the projected area of contact under load. the elastic modulus can be determined by first calculating the reduced modulus which accounts for the elastic displacements of both the sample and indenter as follows;

$$E_r = \frac{S\sqrt{\pi}}{2\beta\sqrt{A}} \quad (2)$$

where β is a constant dependent on the geometry of indenter, which is 1.034 for a Berkovich indenter and S is the contact stiffness which equals the slope of the upper portion of the unloading curve. The elastic modulus of the test sample is calculated from the reduced modulus using:

$$\frac{1}{E_r} = \frac{1-\nu^2}{E} + \frac{1-\nu_i^{\,2}}{E_i} \quad (3)$$

where ν_i and E_i are the Poisson's ratio and elastic modulus of the indentor and ν_i is the Poisson's ratio of the test sample which must be known.

In order to accurately determine hardness and modulus the contact stiffness needs to be precisely calculated. Since the unloading curve is not linear, the following power law expression is applied.

$$p = B(h - h_f)^m \qquad (4)$$

where B and M are fitting parameters and h_f is the final displacement after unloading also determined from the curve fit. The contact stiffness is found by analytically differentiating this expression and evaluating the results at the maximum load.

The next step involves determining the contact depth, h_c, which is less than the total penetration depth, h, for elastic contact as shown in Figure 22. The contact depth can be written as

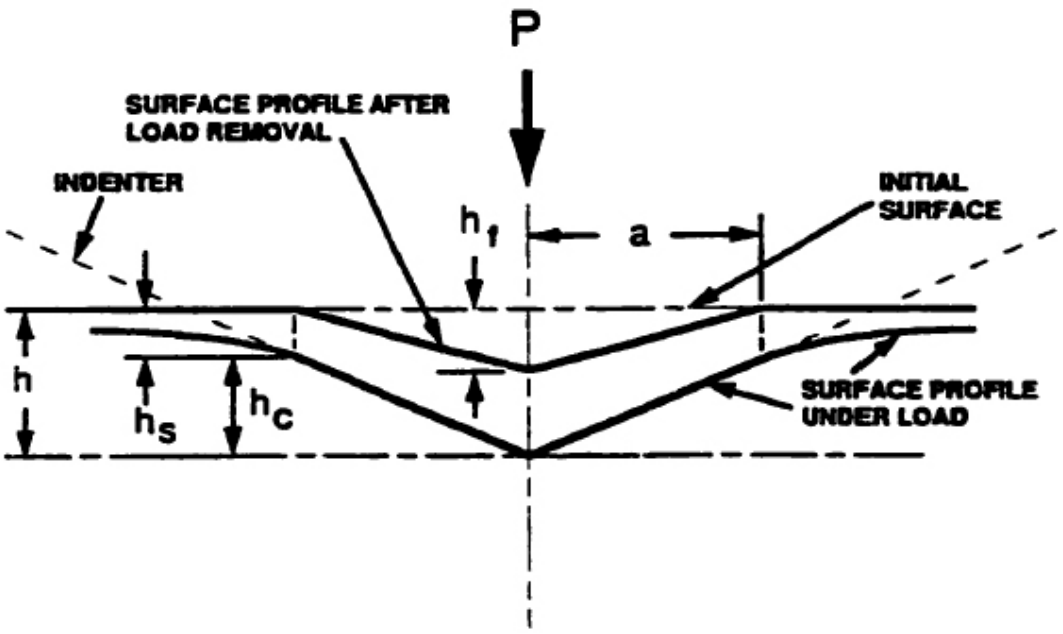

Figure 22. Schematic representation of a nanoindentation hardness impression.

$$h_c = h - h_s \qquad (5)$$

where h_s is the displacement of the surface at the perimeter of the indent and h is the penetration measured by the indentation system. h_s can be estimated from the following expression.

$$h_s = \frac{\varepsilon P_{\max}}{S} \qquad (6)$$

where ε is a geometric constant (0.72) for a Berkovich indenter.

The contact depth can now be calculated, however, the contact area of the indenter still needs to be found to determine hardness. A perfect Berkovich diamond tip has a contact area which is related to the contact depth by the expression:

$$A_c = 24.5 h_c^2 \quad (7)$$

However the Berkovich tip is never atomically sharp and at the small penetration depths commonly used, the rounding of the tip has a significant impact on the contact area. These deviations can be overcome by indenting a standard sample with a known modulus at several penetration depths and by assuming that the compliance of the load frame and specimen can be modeled as two springs in series. Using these assumptions the following equation can be written.

$$A_c = \frac{\pi}{4} \frac{1}{E_r^2} \frac{1}{(C - C_f)^2} \qquad (8)$$

where C is the total measured compliance and C_f is the load frame compliance. The contact area is plotted against the depth of indent and fitted to a third polynomial of the following form:

$$A_c = c_1 h_c^3 + c_2 h_c^2 + c_3 h_c \qquad (9)$$

where c_1, c_2 and c_3 are fitting parameters. Since the load frame compliance affects the area function, an iterative process of adjusting C_f and recalculating the area function is used until the

plot of $C - C_f$ vs. $A_c^{-\frac{1}{2}}$ is linear and extrapolates to zero. Fused silica and sapphire are used as standards since they are isotropic and have known elastic modulii.

2.12 Scratch adhesion testing

Scratch testing is used as a method to characterize the adhesive strength of a coating/substrate system. The diamond Revetest unit is used and a schematic representation is included in Figure 23 (b) below.

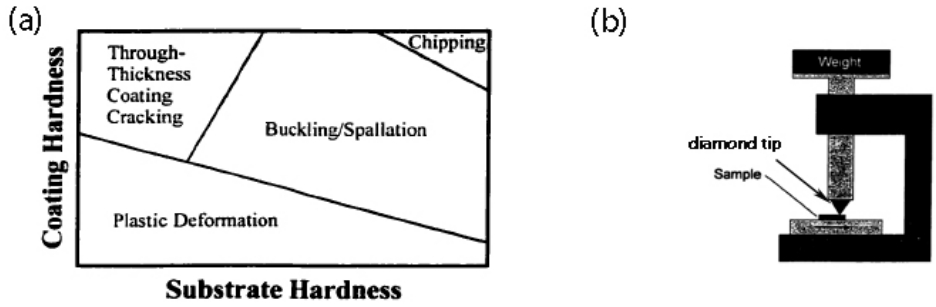

Figure 23. (a) Schematic of scratch adhesion tester (b) failure modes as a function of coating and substrate hardness (bull 1997).

The Rockwell C indenter is loaded axially (Figure 23 (b)) and brought into contact with the coated substrate. The substrate is dragged along the surface under load to produce a scratch. The load is increased in increments until failure of the coating can be observed using an optical microscope. The load at which failure occurs is designated the critical load. Coating failure has been separated into three categories as follows.[39]

- Through-thickness cracking: This form includes tensile cracking behind the indenter, conformal cracking as the coating is bent into the scratch track and Hertzian cracking
- Spallation: This form of cracking included compressive spallation ahead of the indenter, buckling spallation ahead of the indenter or elastic recovery induced spallation behind the indenter.

- Chipping away of the coating.

The type of failure observed is primarily dependent on the coating hardness as well as the substrate hardness and is summarized in Figure 23 (a)

The nitride coatings investigated in this thesis have a high hardness while the substrate used for the scratch test samples,M2 and M50 represent relatively soft materials. Coatings deposited on the M50 and M2 should fail as a result of through thickness cracking and spallation while for harder materials like WC the coating would display spallation or chipping.

The prime advantage of this testing method is the speed of the tests and the relative ease of testing setup. It is difficult to obtain quantitative data since the complicated stress field imposed by the indenter does not easily allow for the calculation of the work of adhesion. Since the mechanical properties of the substrate affect the failure mechanism and hence the critical load to failure, it is rather difficult to compare adhesion results on the same coating with different substrate materials. Samples within a data set also need to have the same coating thickness since the critical load increases with coating thickness. The scratch test is a localized tests so multiple areas of the same coating need to be tested to ensure local inhomogeneties do not affect the result.

2.13 Residual stress measurements

Wafer curvature measurements allowed for the calculation of in-plane residual stress using the Stoney's equation[40].

$$\sigma = \frac{Y_s}{6}\frac{t_s}{t_f}\frac{1}{R} \qquad (10)$$

where Y_s represents the substrate biaxial elastic modulus which is related to the Young's modules by the equation $Y_s = E_s/(1-\nu_s)$ where ν_s is the substrate Poisson's ration, t_s the

substrate thickness, t_f film thickness and R the radius of curvature of the coated substrate. The substrate thickness was measured using a micrometer and the film thickness was measured using a Dektak 3030ST profilometer on a masked section of the substrate. The radius of curvature was also measured using the profilometer with a scan length of 50mm. The initial curvature of the uncoated substrate was taken into account as well as the contributions of the pre-deposition substrate etch to the total film thickness. It is important to note that the value of the stress calculated from Stoney's equation is the summation of both the intrinsic film stress and the thermal stress. The thermal contribution can be solved using the following equation.

$$\sigma = \frac{(\alpha_s - \alpha_f).(T_{meas} - T_{dep})}{\left[\frac{(1-\nu_f)}{E_f} + \frac{h_f(1-\nu_s)}{h_s E_s}\right]} \quad (11)$$

where E_f , E_s , ν_f and ν_s are the young's modulus and Poison's ratio for the thin film and substrate, respectively. The coefficients of thermal expansion for the film and substrate are represented by α_f and α_s while the T_{meas}, T_{dep} denote the temperature at which sample is measured and temperature of deposition. The thickness of the coating and substrate is accounted for in h_f and h_s [41, 42]. Without stage heating, our depositions are at low enough temperature that thermal effects are discounted. The ν_s and E_s used for Si are 0.28 and 131GPa respectively. Several sources of error creep into this measurement. There are differences in length of the Si wafer because it is cut manually. In cases of large radius of curvature the scale length has to be limited due to machine limits. Multiple silicon wafers are places in the magnetron chamber and its residual stresses are calculated and a 10% error bar is arrived at.

2.14 X-ray Diffraction

X-ray diffraction (XRD) is carried out to investigate the crystallinity of the coating material. The scans were carried out in the J.B. Cohen X-ray facility at Northwestern University on a Scintag XDS diffractometer having an unfiltered Cu-Kα radiation source operated at 40kV and 20mA. In some cases to eliminate substrate effects , XRD is carried out in grazing angle geometry. The X-rays are incident on the film surface at a low constant angle (ω), while the detector moves through 2θ, [43] resulting in a shallow penetration.

2.15 Low-Angle XRD

Low angle XRD results from the reflection of X-rays off layer interfaces and thus is not affected by the crystalline quality within each layer. The reflectivity of an interface depends on the difference in electron density of the two layers. In principle low angle XRD directly gives the Fourier transform of the composition change. A Bragg peak can be seen from the coherent interference of each bilayer. Correcting the peak location, θ_B, for refraction leads to

$$\theta_B^C = \sqrt{\theta_B^2 + \theta_C^2} \qquad (11)$$

Where θ_C is the angle of total internal reflection. Using Bragg's equation and the corrected location of the Bragg peak , the bilayer thickness, Λ can be calculated.

$$\Lambda = \frac{\lambda}{2\theta_B^C} \qquad (12)$$

where λ is the wavelength of the x-rays (λ=1.54 A° for Cu K_α). It is important to note that refraction and absorption effects become important at extremely small angles (<3° for Cr K_α radiation) making these patterns more complicated. Another draw back of this method is the inability of the process to distinguish the difference between a rough interface and a diffuse

interface[44]. Simulation can however determine quantitative estimates of Λ (bi-layer periodicity), individual layer thickness and interfacial roughness/width. Our TEM imaging of the interface offers direct evidence of interface roughness so no simulations were carried out as part of our study. The grazing angle studies were carried out on a Rigaku AXT-G Thin-film Diffraction Workstation. The Rigaku has a high intensity 18kW copper x-ray source coupled to a multilayer mirror. The system has selectable x-ray optical configurations suitable for work with single crystals. The unit also features a 5-axis goniometer with several 4-crystal monochromaters that couple to the multilayer mirror.

2.16 X-ray Photoelectron Spectroscopy

XPS is a technique for analyzing the concentration and chemical state of elements present in the near surface region of a material. It is accomplished by irradiating the sample with monoenergetic soft x-rays and analyzing the energy of the ejected electrons, given by the photoelectric effect:

$$B.E. = h\nu - K.E. - \phi_s. \qquad (13)$$

In the above equation, B.E. is the binding energy of the atomic orbital from which the electron originated (in the sample), K.E. is the kinetic energy measured by the spectrometer, $h\nu$ is the energy of the incident photon, and fs is the work function of the spectrometer. As each element has a unique set of binding energies, XPS can be used to identify the elements present in a sample. XPS analysis was performed on the wear debris with an Omicron ESCA probe, which was equipped with an EA125 energy analyzer. Photoemission was stimulated by a monochromated Al K-alpha X-ray (1486.6 eV) with an operating power of 300 W. The analyzer was operated in the constant analyzer energy (CAE) mode at 60 eV (survey scan) and 25 eV

(detailed scan) of core level lines. Binding energies were referenced to the C 1s binding energy set at 285.0 eV.

2.17 Transmission Electron Microscopy

Microstructure characterization on the nano meter scale was carried out via Transmission Electron Microscopy (TEM). Two microscopes were used, the JEOL 2100 TEM and a Hitachi H-8100 TEM, operated at 200keV with a base pressure of ~$1.5*10^{-6}$ Torr in the EPIC facility at Northwestern University. It is a powerful tool to directly image nanocrystallites and obtain phase information since the beam size can be made as small as 1 nm.

Electrons are treated as probability amplitude waves to explain their interaction with materials during the scattering process in a microscope. The wave function Ψ satisfies Schroedinger's equation

$$\frac{h^2}{8\pi m_o e}\nabla^2\Psi + (E+V)\Psi = 0 \qquad (14)$$

In the absence of a potential, the equation has a plane wave solution. Only elastic scattering contributes to diffraction, although ineleastic scattering is relatively large and primarily contributes to background. The image contrast can be explained using spherical wave and Block wave solutions to the Schroedinger equation using different potentials[45, 46]. Dynamical scattering is very important in TEM imaging. The most important approximation made in kinematical theory is that amplitude of the incident beam at any point of the crystal is the same so that the energy transmitted to the diffracted beam is neglected, and in short, only single scattering processes are considered. In most cases, however the diffracted wave will be scattered again by atoms when its amplitude is large.

High resolution images provide structural information at the atomic level. It is not simply a projection of the specimen structure in the direction of the incident beam. There are several

limitations in interpreting HREM images. For many instances one-to-one correspondence does not exist between the object and the image. The observed fringes don't always correspond to the atomic planes. It is extremely important to understand the imaging conditions so that an accurate interpretation can be made. The uncertainty arises due to the fact that HREM images present details of the specimen comparable to the coherence width of the electron wave. Interpretation of high-resolution images are usually based on theories of linear/non-linear imaging usually complimented by various computational simulations[47, 48].

Direct imaging and electron diffraction can provide a fairly complete picture of coatings.

Plan-view imaging is one of the techniques we employ to characterize the bulk information of our BN-Mo_2N composite samples. The sample is viewed in a direction parallel to the surface normal, leading to the beam interacting with the bulk of the sample. All standard imaging techniques including bright-field (BF), dark-field (DF) and high resolution electron microscopy mode (HREM) can be used. On viewing the sample in conventional HREM mode, whether on or titled off zone[45] , the bulk lattice constant dominates the contrast. High-resolution DF mode, in which an image is formed by putting a small objective aperture around a set of bulk diffraction beams, and is useful in obtaining bulk crystallinity information. Selected area (SA) diffraction uses a small aperture in the first image plane below the objective lens to obtain diffraction patterns of selected areas and identify their crystal structures[46]. Scanning transmission electron microscopy (STEM) imaging is a powerful atomic mass (Z) sensitive technique to study material localization on the sub-nanometer scale. The dominant Z contrast for distinction of different materials comes from the high angle annular detector. In a multiphase system if all other variables are constant, the heavier elements appear bright and the light elements appear dark.

This technique allows us to study interfaces down to the sub-nanometer scale and combined with EDX (chemical analysis) serves as a powerful tool for special resolution on the nanometer scale. Cross-section TEM samples were prepared using a standard preparation technique [49] , initial steps in TEM sample preparation are shown in Figure 24. Thinning down to electron transparency was accomplished using a Gatan Precision Ion Polishing System (PIPS). During the ion milling the sample is rotated quicker when the ion beams are in the direction almost parallel to the interface than when the beam is perpendicular to the interface. This corrects for differences in sputtering rates of the film and the substrate.

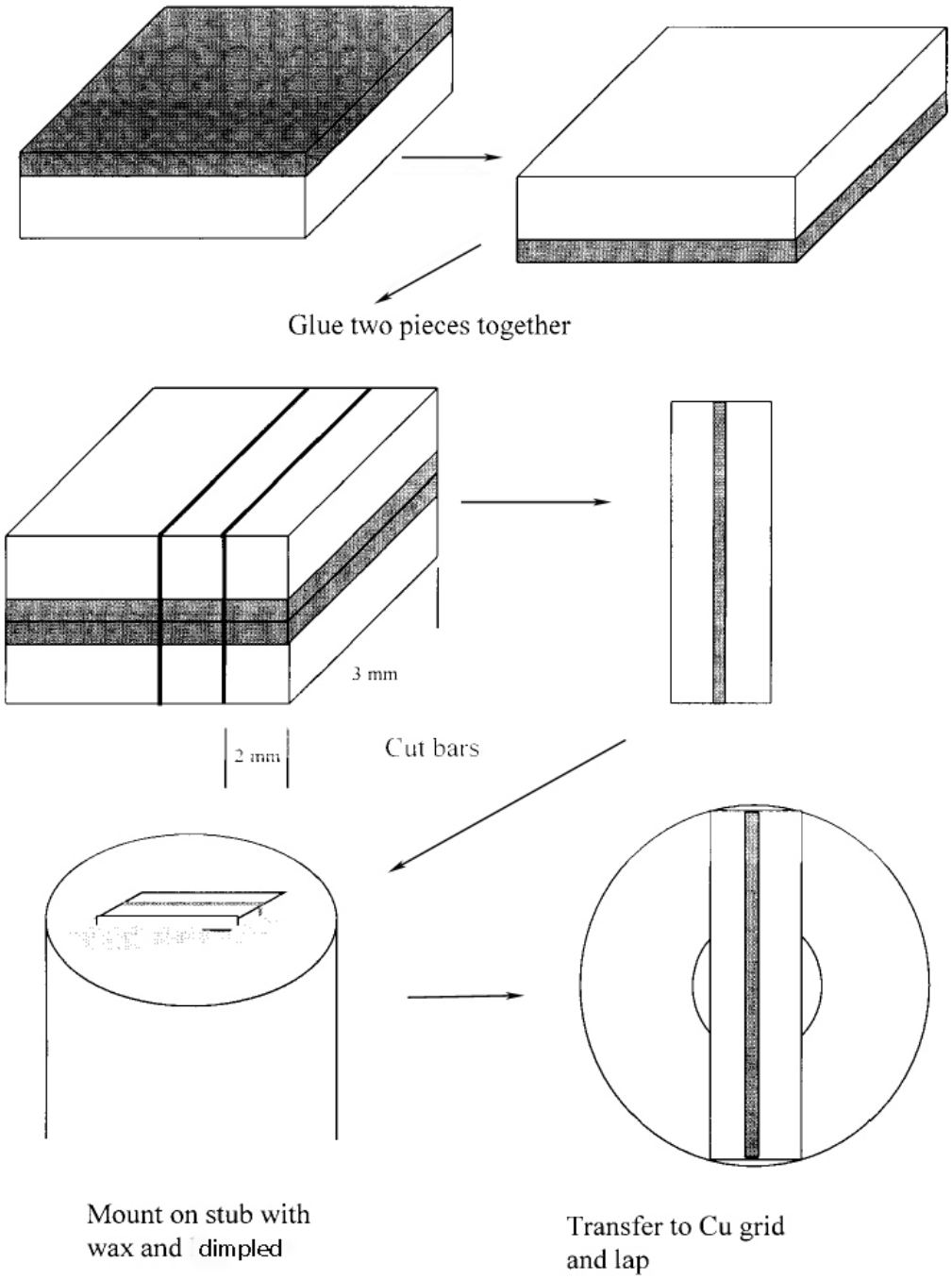

Figure 24. Schematic representation of initial sample preparation technique used for cross-sectional TEM samples.

2.18 Friction testing at room and high temperature

A CETR micro-tribometer (UMT) is used for our room temperature friction studies. It is set up in a ball-on-flat configuration calibrated according to the manufacturer's instructions. A schematic of the test rig is shown in Figure 25. The machine applies normal forces on the flat surface via a stationary ball. The flat is then rotated at a specified speed and the force in the plane of the substrate is measured.

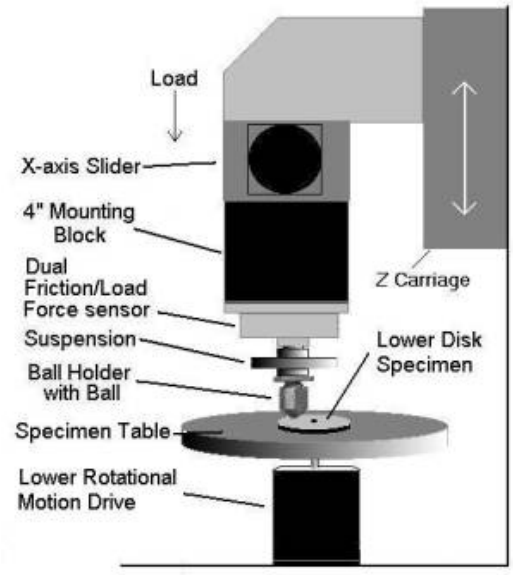

Figure 25. Schematic of ball on flat configuration CETR room temperature tribometer.

The high temperature tribometer is a CSEM tribometer which has a maximum temperature rating of 1000°C. The testing setup is very similar to the room temperature tribometer except that the substrate is heated to the desired temperature level before running the ball on the surface. Figure 26 shows the coated M50 on the tribometer stage surrounded by the furnace heater jacket. An image of the tribometer at high temperature is also inserted into Figure 26. The unit at Argonne National Laboratory was non-functioning and had a leaky heating coil. Custom parts had to be built to get it working and pass safety protocols. Dr. Bob Erck's help is acknowledged here.

Figure 27 (a) shows the external floating power supply that was used to power the leaky heating filament of the tribometer. Figure 27 (b) shows the custom built over-temperature controllers that cut off power to the heating coils in case of excessive temperature and cooling line failure. An aluminum enclosure with a lid around the ball holder serves to enclosed the test piece and acts as a primary chamber in which specific gases can be backfilled. This primary chamber is backfilled with nitrogen for some of the high temperature tests. This enclosure is by no means air tight since cooling fans are present in close proximity to cool the bearings. Limitations of the equipment and impurities in the N_2 gas (5 ppm O_2) make us conclude that the atmosphere is only "near nitrogen" and has nominally about 2-5% of oxygen contamination. Although for convenience the following chapters will refer to the tested in the "near N_2" just as test in N_2, due note should be made of the 2-5% oxygen contamination level.

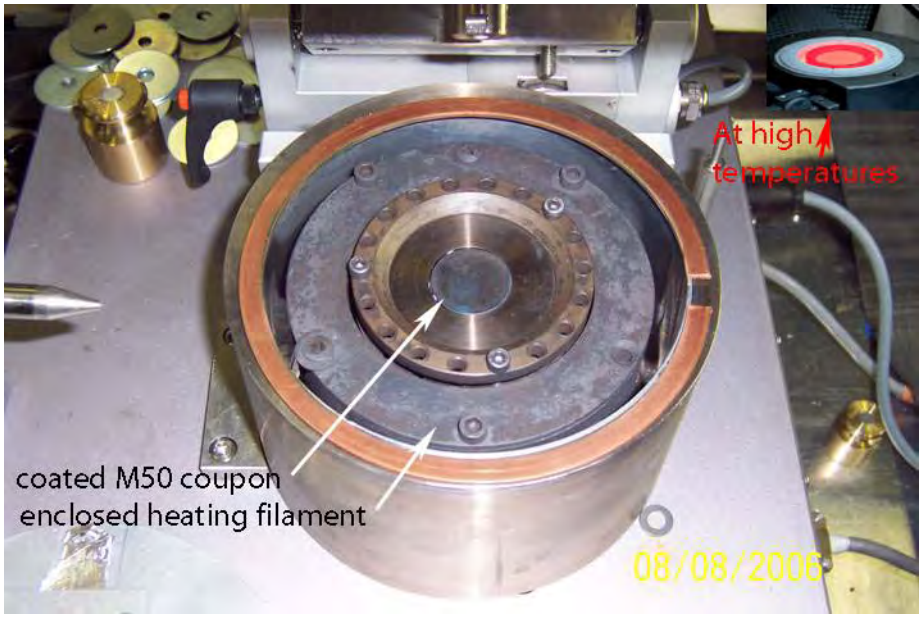

Figure 26. Sample holder arrangement of the CSEM high temperature tribometer.

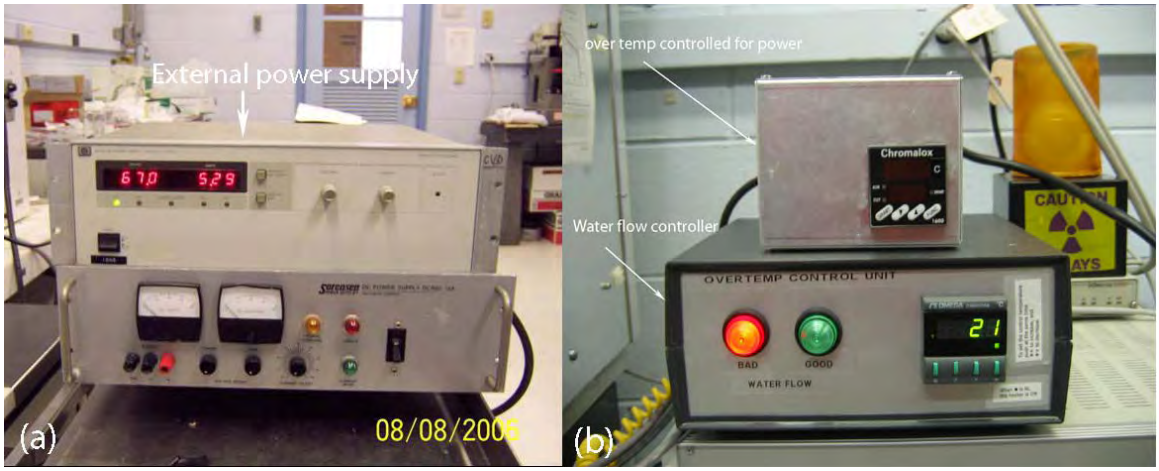

Figure 27. Custom addition to the CSEM tribometer (a) External floating power (b) Custom lab built over temperatures controllers.

2.19 Industrial validation testing

Continuous drilling tests were conducted at Ford and Boeing laboratories to determine the performance of the CrN/Mo2N coatings in standard drilling operations. 20 mm holes were drilled in compacted graphitic iron blocks at Ford. While 0.4'' holes were drilled in Ti6Al-4V alloy at Boeing. Other parameters such as feed-rate are shown in Table 2. Temperature was measured with a calibrated thermal imaging camera's at both test sites. Figure 28 (a) shows the test setup at Ford Figure 28(b) shows the custom built spindle that allows us to direct nitrogen into the drill bit via its through-holes and test in N_2.

Table 2. Validation testing parameters at Industrial test sites. (note: s.f.m =surface feet per minute, i.p.r=inches per rotation and d.o.c=depth of cut).

	Work Piece	Test Conditions
Boeing Test	CGI	(325-400) s.f.m/0.005 i.p.r/ (20-40 mm) d.o.c
Ford Tests	Ti6Al4 alloy	(30-80) s.f.m/ 0.002i.p.r/0.4" d.o.c

Figure 28. (a) CNC machine at Ford (b) custom made spindle to feed in nitrogen.

Figure 29 shows the testing fixture at Boeing with the thermal imaging camera recording the rise in temperature of the block as the block drills into the test block. The figure shows the two configurations possible for the testing. Figure 29 (b) shows the thermal profile as a function of the depth of cut. On the x-axis is the thickness of the block and the y-axis is the temperature recorded at the corresponding position

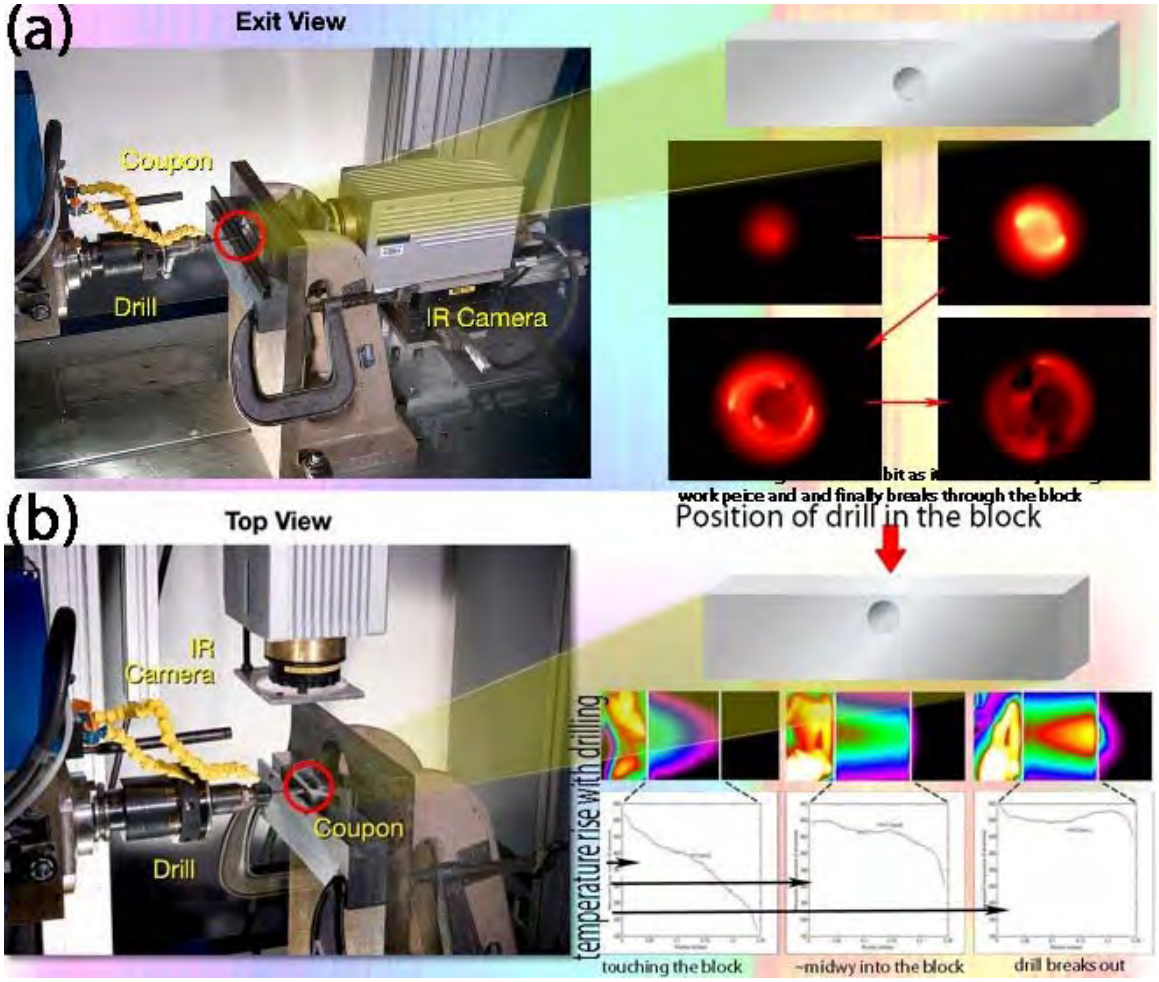

Figure 29. Boeing validation testing test fixture (Courtesy James Castle, Boeing Co.).

Chapter 3. Synthesis and characterization of molybdenum nitride and CrN/Mo_2N multilayers

3.1. Introduction. The basic idea is to incorporate an oxide forming element into the coating to achieve a low friction phase through an auto-initiated response at high temperature. B, P, S are possible candidates as well as incorporating low melting metals like Pb, Bi and Sn. Boron and its advantages will be discussed in the following chapters but its ability to form boric acid in the presence of oxygen is highly desirable. Compounds of phosphorous and sulfur are known to form boundary lubricants, currently in widespread use in liquid lubrication technology. The above listed elements in combination with metals such as Ca can be advantageous. An additional option is incorporation of pairs of elements like Ca and S or Ca and P.

It was proposed to use materials in a nano-layered structure that will be hard, tough, adherent, and lubricious at the service temperature (<1000°C). The use of CrN_x and MoN_x to form multi (nano)-layered coatings offers some advantages as a starting point. Cr(N) is suggested because of its excellent wear and oxidation resistance to about 800°C [18, 19] . CrN and Cr_2N have high hardness, modulus and ratio of H^3/E^2. Among the chromium nitride phases, CrN is known to have the best resistance to abrasion wear. In comparison to hard chrome, the nitrogen doped chromium coatings offer excellent abrasive wear resistance and corrosion resistance[50]. Mo_2N on the other hand has favorable hardness and tribological properties. Mo(N) [20] because it is likely to oxidize at about 500°C, forming its low friction oxide, MoO_3. The presumption is that the Mo-oxide will reduce the cutting friction and consequently the heat generated by high-speed contact (relative to a coating without the Mo). Mo based alloys offer excellent galling resistance in dry un-lubricated contact, but are prone to brittle failure modes[51]. The brittle breakout and

spallation of the coatings can be reduced using other materials as a matrix. The work reported in this chapter is focused on characterizing the individual phases and their behavior. This work was intended to provide insight into which oxides might be formed and how the nitrides and their oxidation products would behave at different temperatures.

Results and discussion

3.2 Molybdenum oxide films

Molybdenum oxide (MoO_3) is the phase that, we propose, will be formed at high temperature from the MoN_x in the coating. MoO_3, formed from the oxidation of MoN_x [21, 52-54] is known to be a lubricious phase and would provide reduced friction. Initially, Mo-oxide films were deposited directly by reactive sputtering and analyzed to determine the phases that were likely to appear as oxidation products. The oxide samples were then annealed in air at several different temperatures to determine their stability of its oxides at different temperatures. This also allowed us to study any physical changes that might occur to the oxides as a result of heating (up to 600ºC). Following these treatments and characterization, we tested the sliding friction.

Phase Characterization

The reactive sputtering was carried out in an atmosphere of 0.3mTorr oxygen and a total pressure of 4mTorr (O_2+Ar), on an M50 substrate with a substrate bias of -50V. The deposition conditions were chosen based on prior MoO_x deposition carried out in this lab. The partial pressure choice was set high enough to form enough oxide. The XRD results confirmed that we deposited MoO_2 and Mo_4O_{11}. Figure 30 (a) shows the XRD pattern on annealing the coating at 250ºC where MoO_3 and Mo_4O_{11} formed the predominant phases. Further annealing to 550ºC (Figure 30 (b)) sharpened and intensified the peaks, but MoO_3 becomes the dominant phase.

There are peaks that can be possibly identified with other phases such as Mo_8O_{23} / Mo_9O_{27} but the identification is still somewhat uncertain, via XRD, due to nearly overlapping peak positions for some of these complex phases. Annealing increased the surface roughness from 25nm in the deposited coating to 100nm and 350nm at 550ºC and 600ºC respectively. Hardness was a low 3-4 GPa and it is likely that the oxide was weakly adhered to the substrate in addition to being very weak itself [55]. Again the higher value of hardness occurred after annealing at the highest temperature, which is indicative of some stress relief and recrystallization.

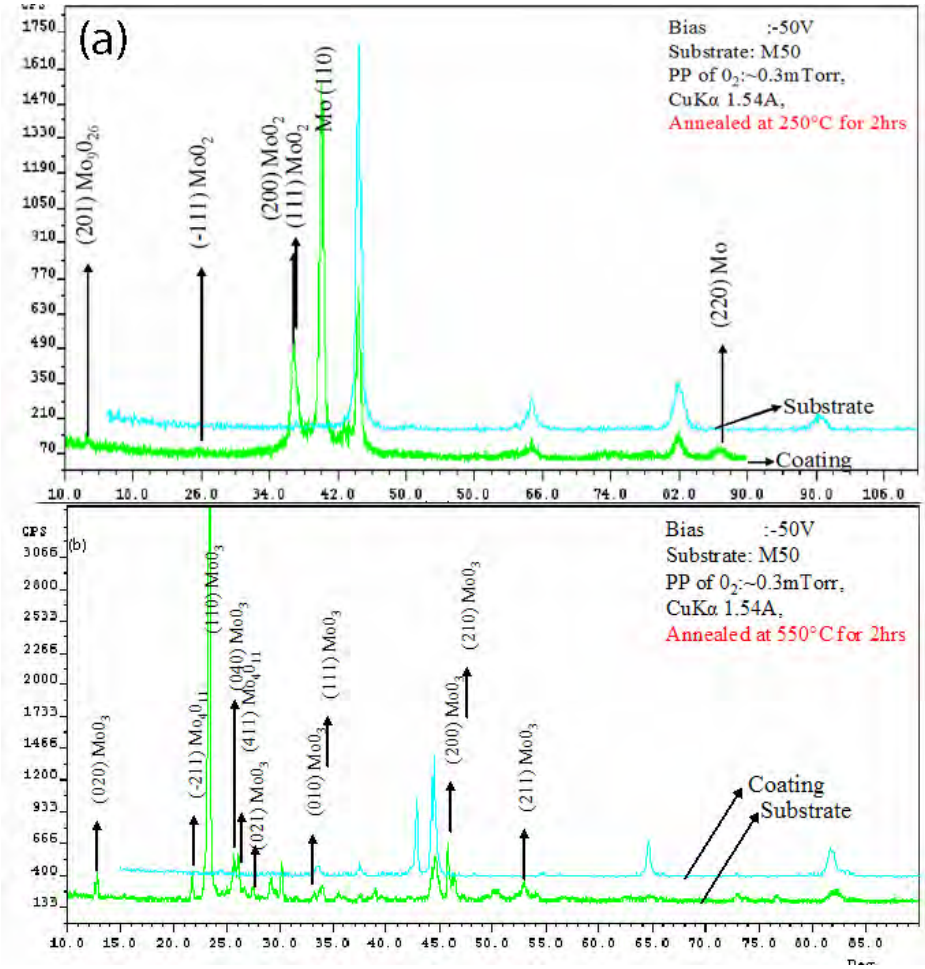

Figure 30. XRD pattern on annealing molybdenum oxide at (a) 250°C (b) 550°C.

Tribological behavior of Mo-oxide films:

Sliding wear tests on the Mo-oxide surfaces demonstrates that the combination of MoO_2 and Mo_4O_{11} as deposited shows a low COF value of less than 0.15. While it is expected that the MoO_3 surface would exhibit low friction [21, 52-54] it was unclear what to expect from the other oxides such as MoO_2, which are stable to relatively high temperature. As the film is annealed, the friction plots get noisier, apparently due to structural changes in the oxide. When annealed at about 550ºC, where the oxide is predominantly MoO_3, the friction is again a stable value of about 0.1 - 0.12 (Figure 31)

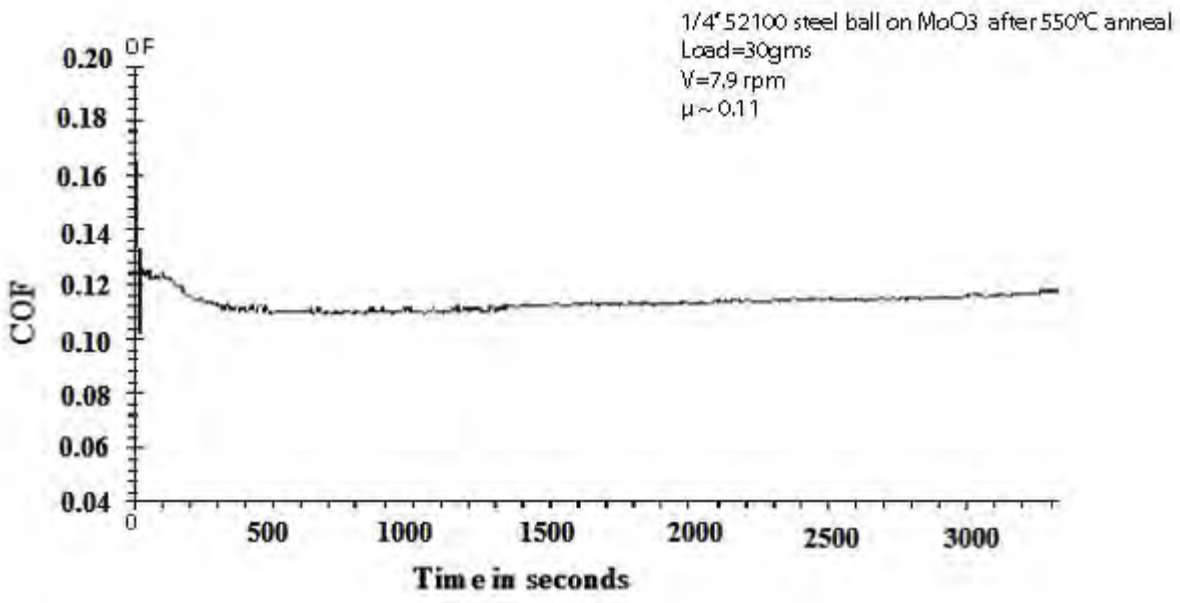

Figure 31. Friction plot for 550ºC-annealed Mo-oxide (MoO3) .

3.3 Chromium oxide films

Cr_2O_3 is the expected product of CrN_x oxidation and is known to be hard and abrasive [21]. It was important to understand and confirm mechanical and friction properties of the oxide, since this could give us some insight into the wear processes in the multilayer and the role played by the Cr_2O_3 formed there. Cr_2O_3 films were reactively sputtered, on an M50 substrate at various partial pressures of oxygen and a total pressure of 4mTorr (O_2+Ar) with a substrate bias of -50V. Hardness of the as deposited sample was about 25 GPa which on annealing at 200ºC dropped to 15 GPa. Further Annealing leads to an increase in hardness to 18Gpa, 20Gpa and 30Gpa at temperatures of 250ºC, 400ºC and 600ºC respectively. The drop in hardness initially on annealing could be indicative of stress relief as defects migrate to free surfaces or interfaces. Friction tests on the coating shows that Cr_2O_3 removes material from the steel ball fairly rapidly and a “steady state” condition is reached quite rapidly. The COF value appears in the 0.6-0.7 range which is consistent with published results [21]. The friction value has a component of metal on metal sliding involved since metal-metal sliding lies in the 0.6 to 0.8 range. Metal transfer is confirmed via EDS and optical microscopy.

Heat Treating in Argon

As deposited Cr_2O_3 is annealed in the presence of Ar (Figure 32), indicate that the as deposited film shows strong preferred texture and this is enhanced on annealing. The (104) and (110) peak of Cr_2O_3 show sharpening on annealing, indicating a preferred orientation.

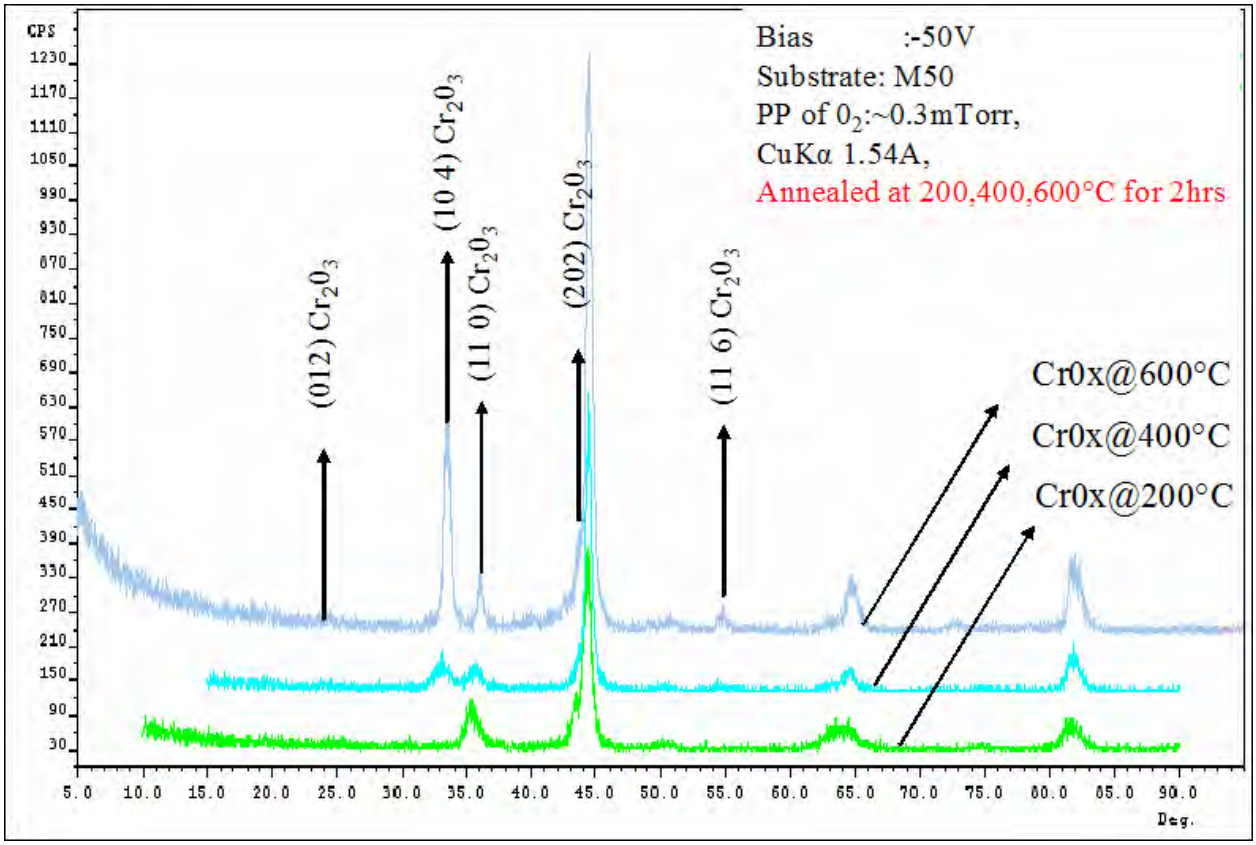

Figure 32. XRD micrographs change with annealing temperature of Cr_2O_3.

3.4 Mo-nitride films

MoN_x deposition has been carried out at different partial pressures was carried out. We will discuss annealing and friction effects of a solid solution phase of Mo-N_x here in this section. Figure 33 shows the effects of annealing the deposited sample from RT to 400ºC. The (110) peak of Mo-N solid solution shows a sharpening on annealing, indicating a preferred orientation of (110). This is similar to the results of annealing Cr_2O_3 (Figure 32). Since molybdenum nitride is one of the constituents in our multilayer coating, it is necessary to explore the oxidation process on the MoN_x films. The different phases of MoN_x were reactively sputtered at different partial pressures of nitrogen forming Mo-N_x, β-Mo_2N and γ-Mo_2N. At low partial pressures of 0.3mTorr N2 a coating of Mo-N_x is formed (Mo bcc structure with nitrogen incorporated into the lattice). At intermediate partial pressures of (1-2) mTorr β-Mo_2N (hexagonal) was deposited and at partial pressures of 2mTorr and above γ-Mo_2N (tetragonal) was deposited. This is in good agreement with literature [56].

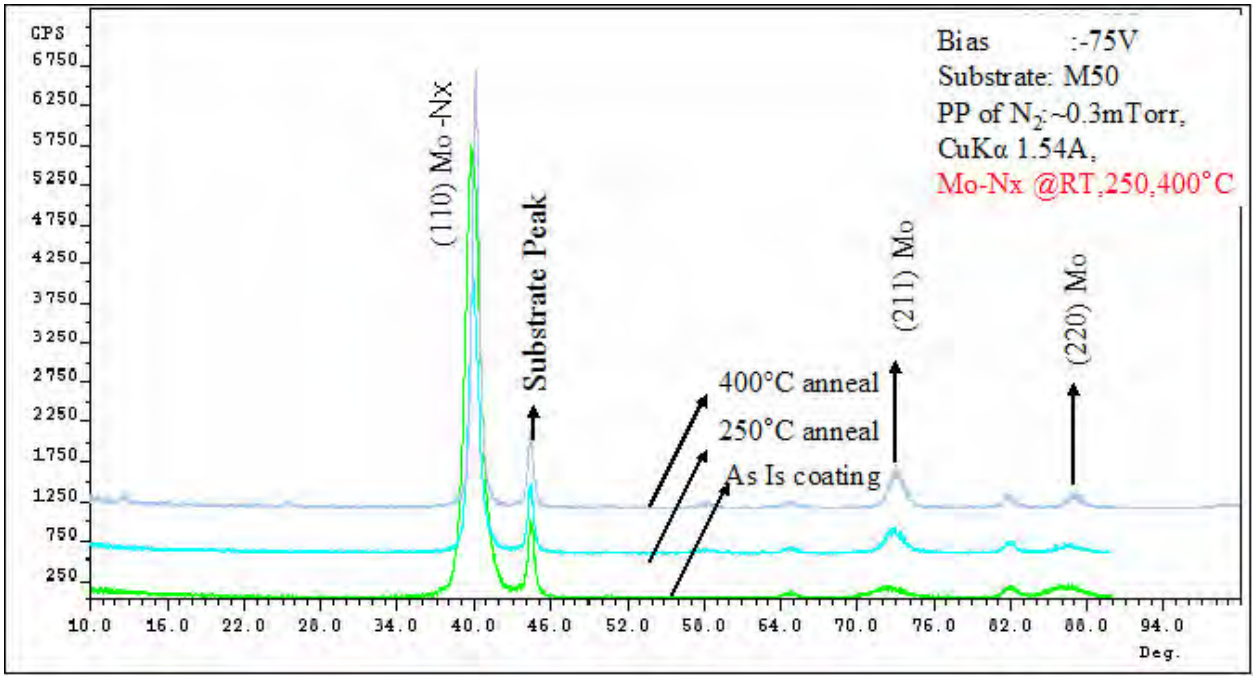

Figure 33. Micrograph of change in XRD pattern of Mo-N_x on annealing. .

The oxidation products and oxidation temperatures of Mo_2N have been well characterized by researchers [53, 55, 57] . We report the annealing results on Mo-N_x since it showed the lowest COF at room temperatures. Annealing Mo-N_x showed that the MoO_2 phase and possibly the Mo_4O_{11} phase appear first, but up to 400ºC, the dominant structure is still Mo-N_x.

At 650ºC, we observed nearly complete oxidation with a dominant MoO_3 peak and Mo_4O_{11} (Figure 34). Many of the unlabeled peaks are from the oxidation products of M50 substrate.

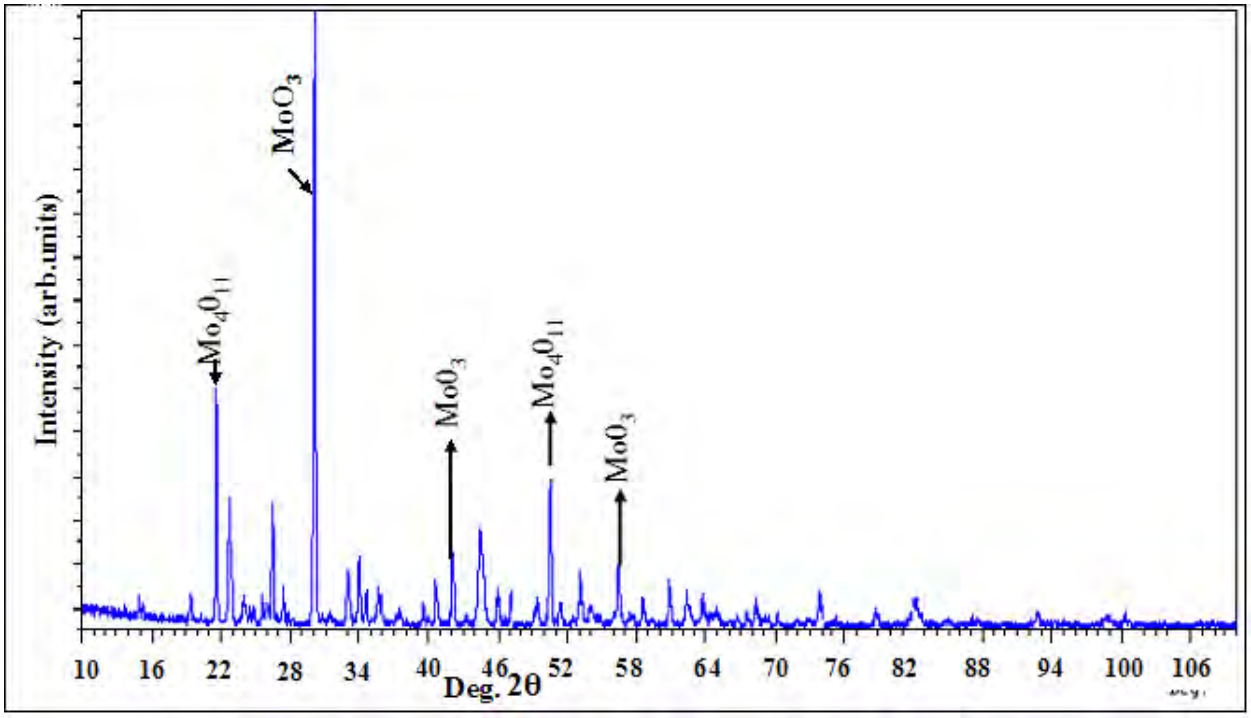

Figure 34. XRD pattern for Mo-N_x deposited on M50 and annealed at 650ºC

Heat Treating in Air

Tribological behavior of MoN_x films:

We found that the Mo-N_x film exhibits a lower friction coefficient of 0.16 to 0.18,(Figure 35) (the horizontal line in the figure assists in reading the COF level). Other nitride phases such as β-Mo_2N and γ-Mo_2N showed a COF ~0.7. Friction testing on an annealed Mo-N_x sample in air (annealed at 400°C for 1 hr) indicates a friction coefficient of around 0.16 (Figure 36). Though our XRD data does not indicate any oxidation products, there is a marked difference in the nature of the friction curve. The curve is markedly noisier with indication of early breakdown and a gradual increase of friction to 0.6-0.7, indicative of a loss of the coating. It appears that the transformation from the nitride to the oxide might not yield a surface quite as stable (mechanically) as the as-deposited oxides, but the resultant friction is still quite low. The properties of Mo-N_x suggest that it is not very hard (12 GPa), whereas we know that MoNx films

can be deposited with hardness values in the 20-30 GPa range [20]. Thus, most of the sputtered phases show crystallinity on deposition, and on annealing, the XRD pattern indicates recrystallization and growth taking place. The Mo-N_x phase was a low friction phase which on annealing, maintained its low friction behavior. Given our success with depositing the CrOx and MoO_x, our effort in the following section will be to characterize the phase-space of Mo and Cr nitride.

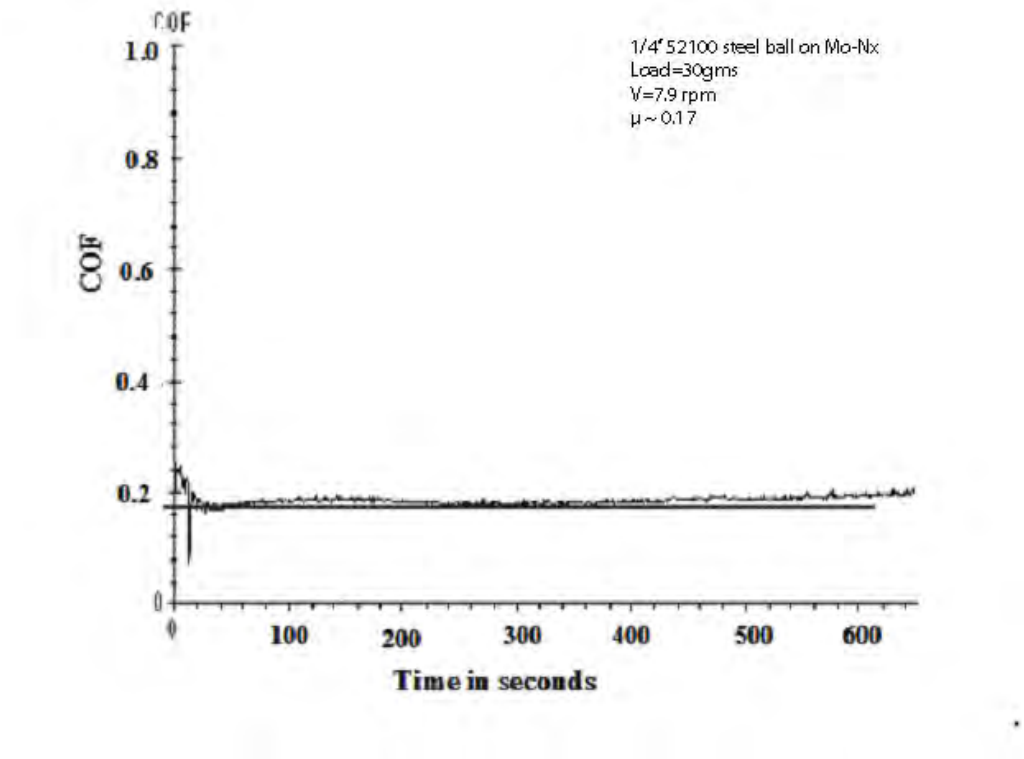

Figure 35. Friction trace for as-deposited MoN_x coating.

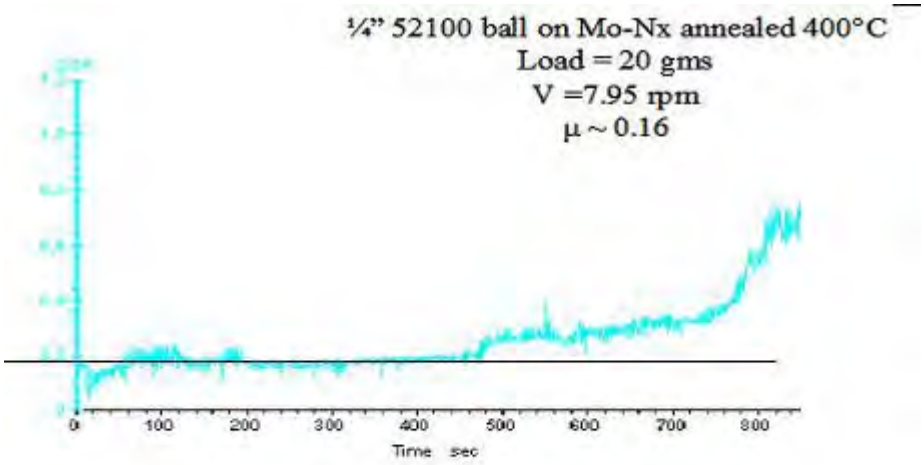

Figure 36. MoNx annealed at 400°C and tested at room temperature showing low friction.

3.5 Deposition of phases of MoN_x and CrN_x

Given the multiple phases of Cr and Mo with wide ranging mechanical properties it is important to optimize our sputtering conditions to get good bulk hardness and good adhesion to the substrate. Prior experience in depositing MoN_x has shown that -50V is a good bias condition for well adhered films. The powers on the chromium and molybdenum cathodes were set at 2.1 kW and 3.5 kW respectively. The power level was limited by the maximum operating current of the power source (Cr side). The total pressure was held constant at a 4 mtorr pressure ($Ar+N_2$), and the substrate bias was a constant -50V. It is critical to understand the effect of nitrogen partial pressures on the formation of the nitrides since the reactivity of Cr and Mo to nitrogen is different (Figure 37). The general trend of lower deposition rates with partial pressure is related to the nitride poisoning of the target. The CrN_x deposition rate seems to follow such a trend except at 2 mTorr, where the deposition rate seems to increase by about 1.4 times from its value at 1.5mTorr. This is related to the higher amounts of cubic-CrN in the coating at 2 mTorr than at 1.5 mTorr. For equal number of Cr atoms deposited CrN (70 $Å^3$/Cr atom) occupies more volume than Cr_2N (50 $Å^3$/ Cr atom) due to differences in lattice parameters. Hence for equal metal deposition rates the coating at 2 mTorr should be about 1.4 times thicker than the deposition rate at 1.5 mTorr. Allowing for lower metal deposition due to target poisoning our calculations are in good agreement with the results. The deposition rate increase at 3.5mTorr in the Table 3 shows the possible phases and lattice parameters of Cr and Mo that can be reactively sputtered. The β-Mo_2N and Cr_2N are the hardness phases, in the following sections we will discuss the phases that we deposit and the process and adhesion optimizations carried out for this deposition.

Table 3. The different compounds that can be synthesized from Cr and Mo, with their crystal structures.

Elements/Compounds	Crystal structure	Lattice parameter(A°)
Cr	bcc	2.91
Cr_2N	hcp	a=4.75,c=4.42
CrN	fcc	4.14
Mo-N	fcc	~3.14
β-Mo_2N	tetragonal	a=4.2,c=8.0
γ-Mo_2N	fcc	4.16
MoN	hcp	a=5.74,c=5.62

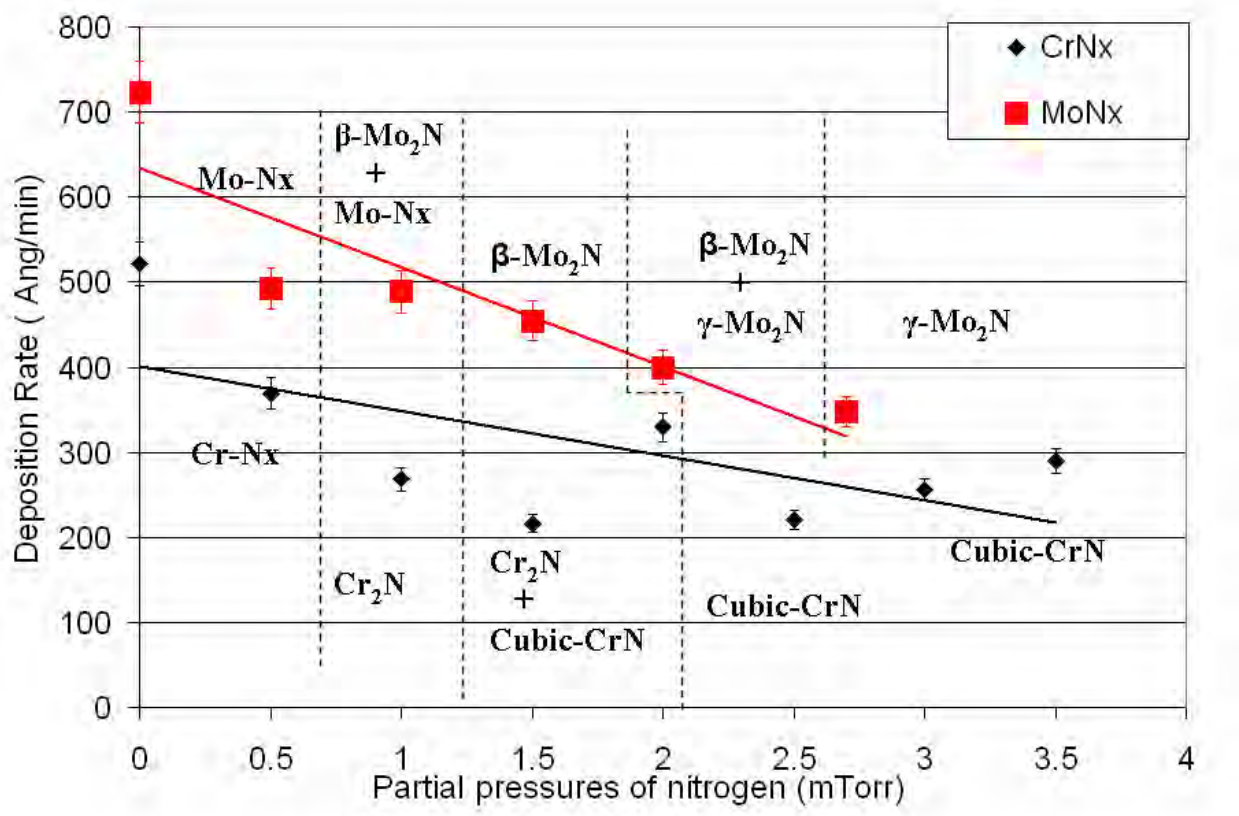

Figure 37. Deposition rates and Phase regions of CrNx and MoNx.

Varying the partial pressure of nitrogen allows us to characterize the deposition rates of the different phases of both CrN_x and MoN_x. The deposition rates control the relative thickness of the two phases. XPS was carried out to determine the exact phases of chromium nitride at intermediate nitrogen partial pressure, since an XRD analysis failed in identifying the phases present because of peak broadening and overlap. The Cr $2p_{3/2}$ in the 1.0mTorr to 2.0mTorr range of reactive sputtering pressure can be decomposed into two components from Cr_2N (576.24 eV compared to reference value of 576.1 eV) and CrN (575.24eV compared to the reference value of 575.5 eV). With increasing partial pressure the peak shifts from the Cr_2N to the CrN peak. The CrN peak location is in better agreement with reference values than those described in literature.[58, 59]

In the case of Mo at partial pressures of less than ~0.8mTorr of nitrogen, we have Mo-N_x, the bcc phase with nitrogen incorporated into its lattice. At intermediate nitrogen partial pressures of around 1 mTorr we have a mixed phase of Mo-N_x and Mo_2N. At pressures of 1.5mTorr of nitrogen, we have the hardest phase of β-Mo_2N.At higher partial pressures of 2 mTorr and above we have the γ- Mo_2N phase forming, initially in combination with the β-Mo_2N and at higher partial pressures it exists as the predominant phase[56]. Similar phase regions of Cr-N_x (solid solution of nitrogen in Cr), Cr_2N and CrN are depicted in Figure 4. The vertical line shown in Figure 4 depicts approximate phase regions. This is in good agreement with similar studies in literature [19, 20].

3.6 Nanostructured multilayered films

To maximize hardness nanolayered (Figure 38) films were deposited via reactive sputtering at an intermediate partial pressure of 1.5mTorr. The Figure 38 (b) shows a cross-section SEM image

with the multilayers clearly visible. The net bilayer thickness was ~5nm with the Mo_2N layer about 3 nm thick and the CrN layer about 2 nm thick. The interface between Mo_2N and CrN typically shows sharp contrast. Calculations from the intensity profiles shown in Figure 39 (a) shows a cross section TEM image of the multilayers while (b) is a line scan of the intensity across the multilayer. The peaks in Figure 39 (b) corresponding to atomic columns in the TEM image. A rough calculation based on these intensity modulations within the CrN and Mo_2N layers allows us to determine the exact number of atomic layers that constitute each layer. The Mo_2N layer contains nominally about 14 atomic layers and the CrN layer about 9 atomic layers. Any atoms lost in interface would show up as a diffuse contrast at the interface and could only be a few atomic layers since bilayer contrast is generally visible throughout the imaged film. The total pressure was held at a constant 4mTorr ($Ar+N_2$) and the substrate bias was a constant -50V. Sapphire substrates were used in samples that were annealed to high temperatures. The chromium and molybdenum targets were set at powers of 2.1 kW and 3.5 kW. This is the regime where the hardest phase of β-Mo_2N and a combination of CrN and Cr_2N are formed, with CrN being the dominant phase. Further characterization of the multilayers are carried out in chapter 4. Different nanolayers periods were synthesized using different rates of rotation of the substrate holder. At low enough bi-layer periodicities with certain combination of compounds multilayer coatings are known to show super-hardening effects. This is a possibility in our films and it was important to characterize this. Figure 40 shows that the bi-layer periodicities were varied from 28 nm to 4 nm. The Mo_2N and CrN hardnesses are included as reference. The hardness of the multilayers is within the rule of mixtures. The hardnesses of the films were in excess of 25Gpa making them suitable for tool coatings and no appreciable hardness increments above the rule of

mixtures (~23 GPA) were observed. Further characterization of the nanolayers will be discussed in Chapter 4.

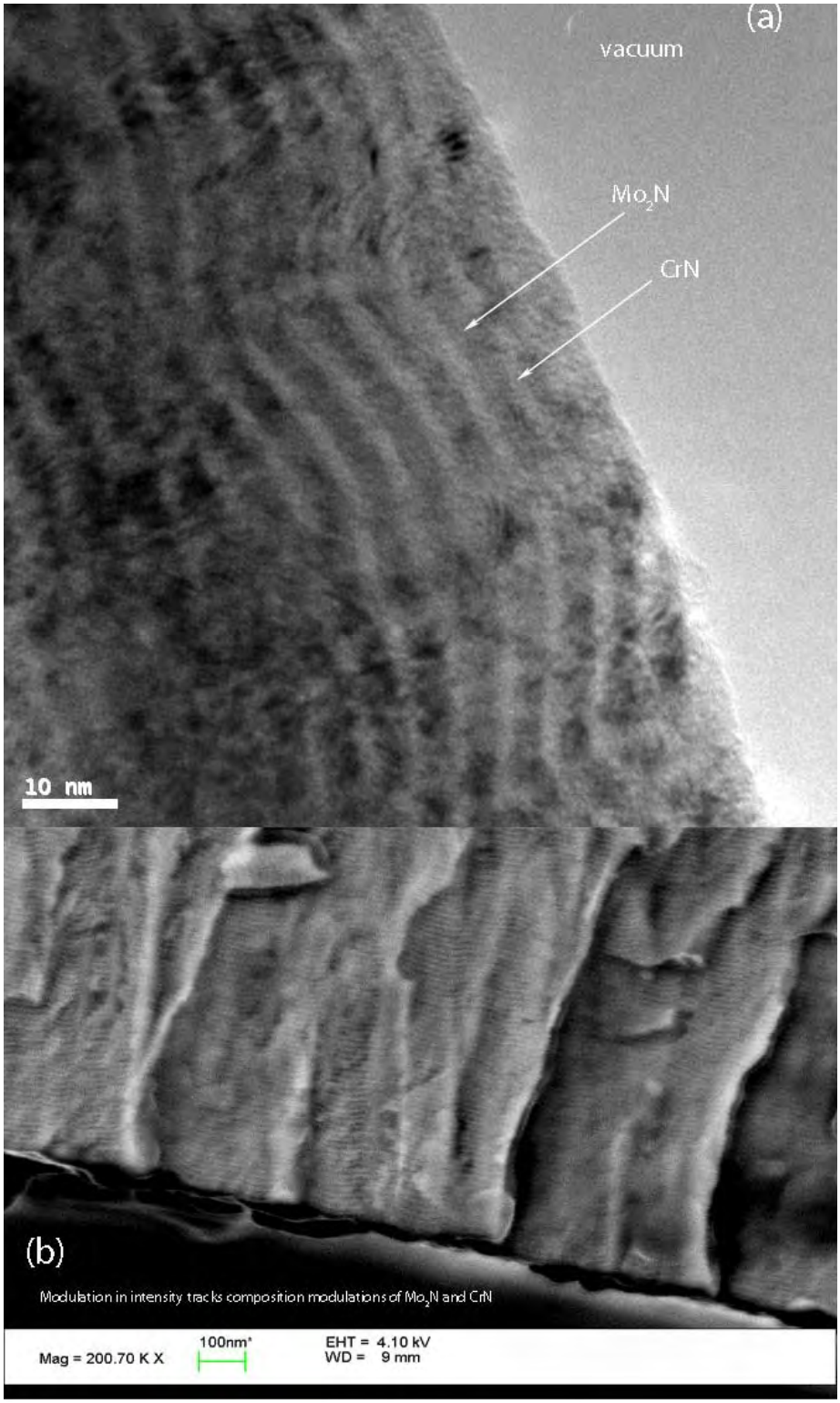

Figure 38. (a) TEM in bright field mode and (b) SEM images of CrN and Mo_2N multilayers

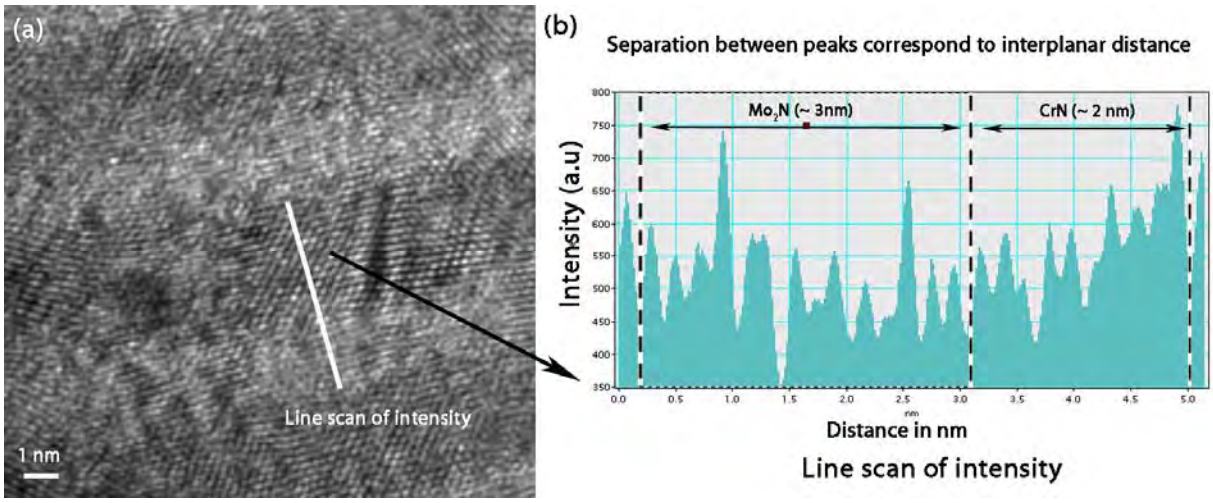

Figure 39. (a) HRTEM image in BF mode shows the contrast difference between the Mo_2N and the CrN multilayers, a rough calculations of the CrN and Mo_2N layer thickness is shown in (b).

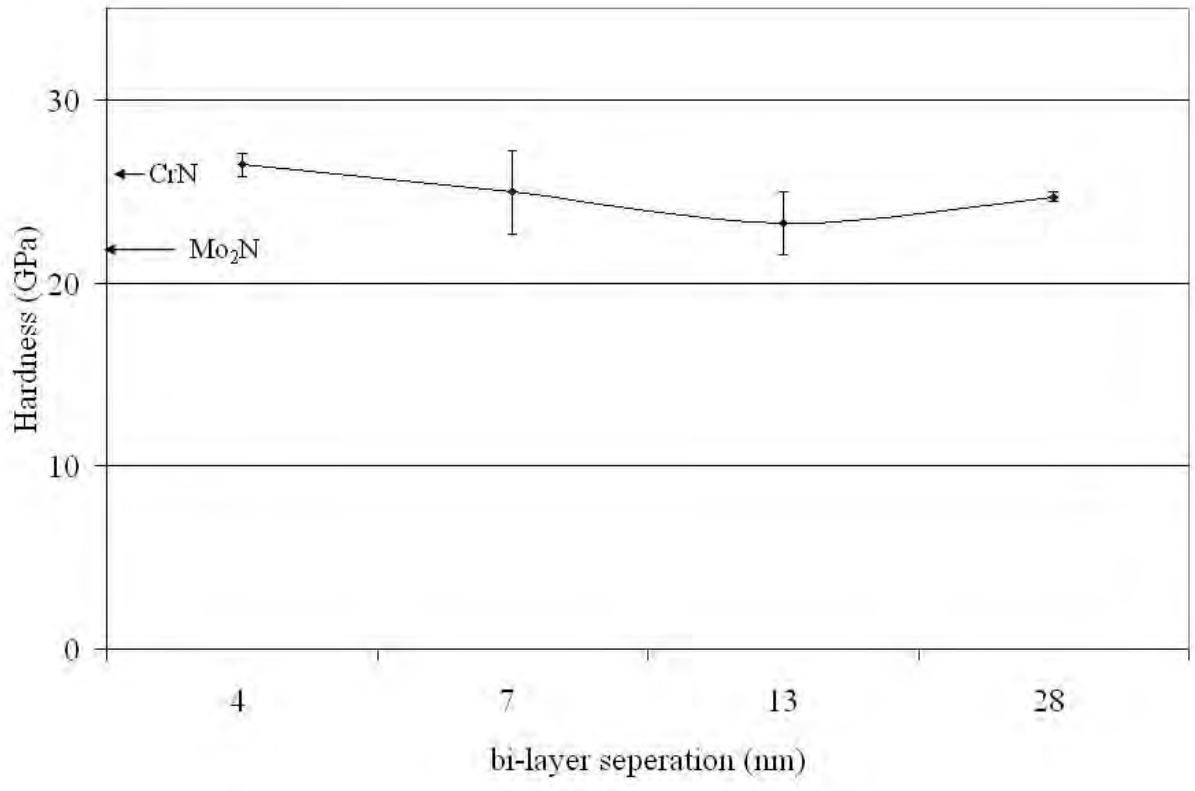

Figure 40. Hardness vs. Periodicity for CrN/Mo_2N multilayers and for CrN and Mo_2N films.

3.7 Conclusions Deposition of the nitrides and oxides of Cr and Mo was carried out .The low friction behaviour of MoO_3 was demonstrated. The various oxidation products of Mo were characterized. Reactive deposition of Cr in O2 showed that a hard and stable Cr_2O_3 phase is likely to form. A complete deposition rate and phase characterization of the CrN_x and MoN_x was carried out. A hardness test of the nano-layered coatings showed them to be in the hardness range of 20-25 GPa. This is the high hardness regime suitable for a tool coating. Deposition of nano-layered Mo_2N/CrN was carried out.

Chapter 4. Temperature activated self-lubrication in CrN/Mo_2N nanolayer coatings

4.1 Introduction

In this chapter CrN/Mo_2N coatings of various multilayer thicknesses will be deposited at various relative ratios of CrN to Mo_2N. The bulk properties such as hardness, residual stresses and adhesion will be characterized and optimized. High temperature friction tests to investigate its properties at high temperatures. The goal of this chapter is to demonstrate the workings of a self-lubricating coating at high temperature. The bulk properties of the coatings will be further optimized with the goal of coating industrial drill bits with these hard coatings. Hard coatings for cutting tools have been in use for the last many decades ,[60-64] and [65], and have evolved from the initial, simple nitride and oxide coatings (such as TiN and Al_2O_3) applied by CVD and PVD in the 1970's, to more complex, high-performance alloy nitrides (such as TiAlN) employed today. Our efforts are to develop a dry lubricating coating which is the direction industry seems to be taking with the development of other coatings for dry machining applications [66-69].

4.2 Experimental plan

In order to verify lubrication at high temperature and study dependence on the relative ratio of Cr to Mo, the relative amounts of CrN, Mo_2N and the bilayer thickness will be changed. Table 4 shows the coatings that were deposited in this chapter and the relative ratios of the Cr and Mo phase with their bi-layer thickness as well. The different depositions are achieved by varying the power settings on the targets. The bilayer period was varied by changing the rate of rotation of the substrate holder. Chapter 3 discussed the effects of bilayer periodicity on bulk properties at a fixed power level [70]. The current chapter seeks to characterize multilayers of Mo_2N/CrN. TGA studies on the coating will give us some insight into the oxidation process the coating undergoes

with temperature. Annealing tests on the coatings will help characterize the stability of the interface with temperature. Post annealing SEM studies on the surface and cross section will yield direct evidence of the stability of the Mo_2N and CrN interface with temperature. Hardness studies on these coatings would help us understand the effect of changing bi-layer periodicity and power, since these coatings that will eventual serve as hard coatings on drill bits. Finally high temperature friction studies will be carried out to verify self-lubrication at high temperature.

Table 4. Table shows the samples deposited, their relative Mo and Cr ratios, bi-layer periodicities and environmental conditions under which its friction was tested.

Multilayer Samples Deposited			
	Mo_2N:CrN	Bilayer periodicity(nm)	Friction Tested (Air/N_2)
Sample 1	5:4	13	Air
Sample 2	5:4	18	Air/N_2
Sample 3	5:4	4	Air/N_2
Sample 4	10:3	12	Air/N_2

4.3 TEM characterization of the CrN/Mo_2N multilayers

TEM studies would provide direct imaging of the interface of CrN and Mo_2N. Sharply delineated interfaces would provide clear phase separation and would allow us to ensure the controlled wear of individual phases as the top coating wears. This would allow us to ensure the Mo_2N arrives at the surface in a controlled fashion and provides lubrication as needed. Figure 41 confirms a highly crystalline coating with sharp interfaces. The origin of contrast in this case (bright field mode) of the TEM is due to the constituent layers having different atomic number (Z contrast). The lattice imaging allows us to clearly see the differences in crystal orientation across the layers of CrN and Mo_2N. The lattice constant mismatch between fcc-CrN and fcc-Mo_2N is ~1.5% and as region A shows there are some preferred orientations of the coating that leads to epitaxy across the layers in the (111) direction (Figure 41). Region B in the figure also shows areas where the preferred orientation between the layers is not preserved. The electron diffraction insert in Figure 41 shows how the diffraction patterns of the two phases are indistinguishable. The (111) and (200) planes have been indexed. Figure 42 shows a cross-section STEM image of the multilayer.

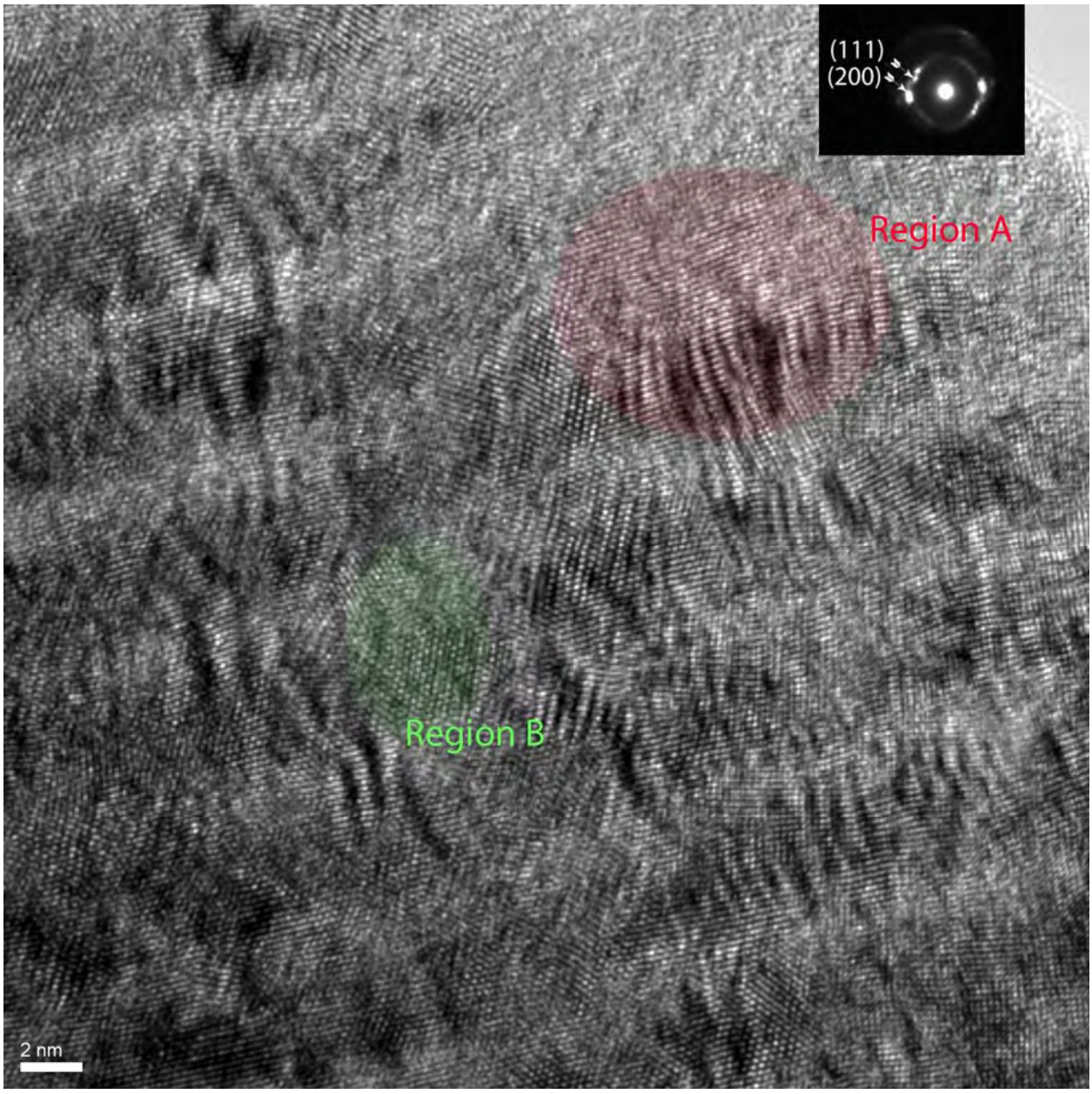

Figure 41. Cross-sectional TEM micrograph of the multilayers in bright field mode.

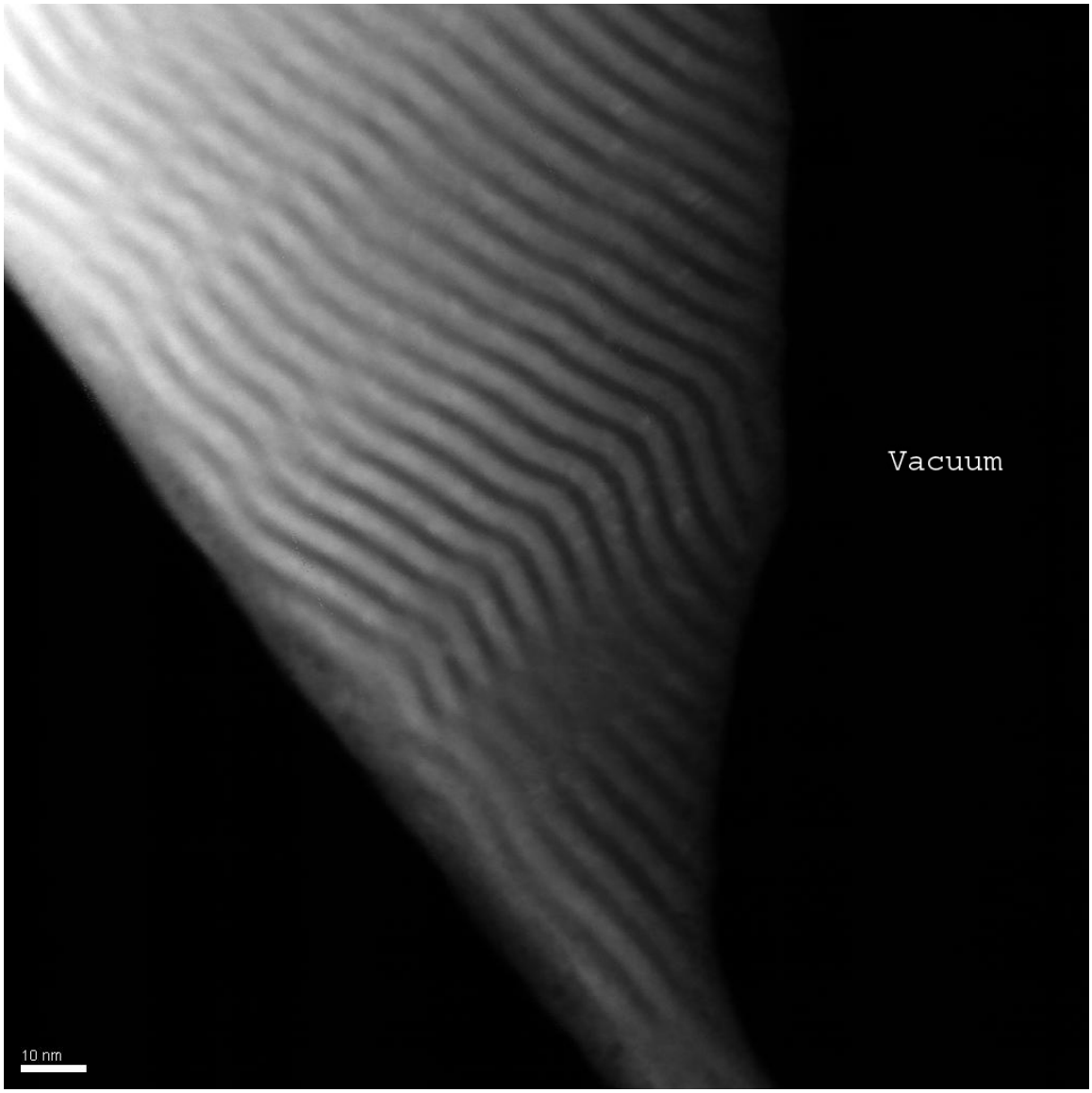

Figure 42. Cross- section STEM micrograph of the multilayers.

The origin of contrast in cross-sectional STEM is almost solely due to differences in atomic number from different scattering angle. The bi-layer thickness is ~6nm and the relative ratio of Mo to Cr phase is 5:4. The STEM image confirms the sharp interfaces, which are critical to the performance of CrN/Mo_2N as a system that self lubricates at high temperature.

4.4 Low angle XRD studies.

Multilayer samples were deposited on a sapphire substrate and subsequently heated in an Ar atmosphere. The rate of heating of the furnace was ~15°C/min and the sample was held at its highest temperature for 2 hrs before allowing the furnace to cool down to room temperature. The Ar flow was maintained at all times during the heat up and cool down cycles. Sapphire was used as a substrate because of its temperature stability. Low angle X-ray diffraction is able to quantify composition modulations and Figure 43 shows that the individual components of our multilayer films are distinct at 400°C and even up to a high temperature of 600°C.

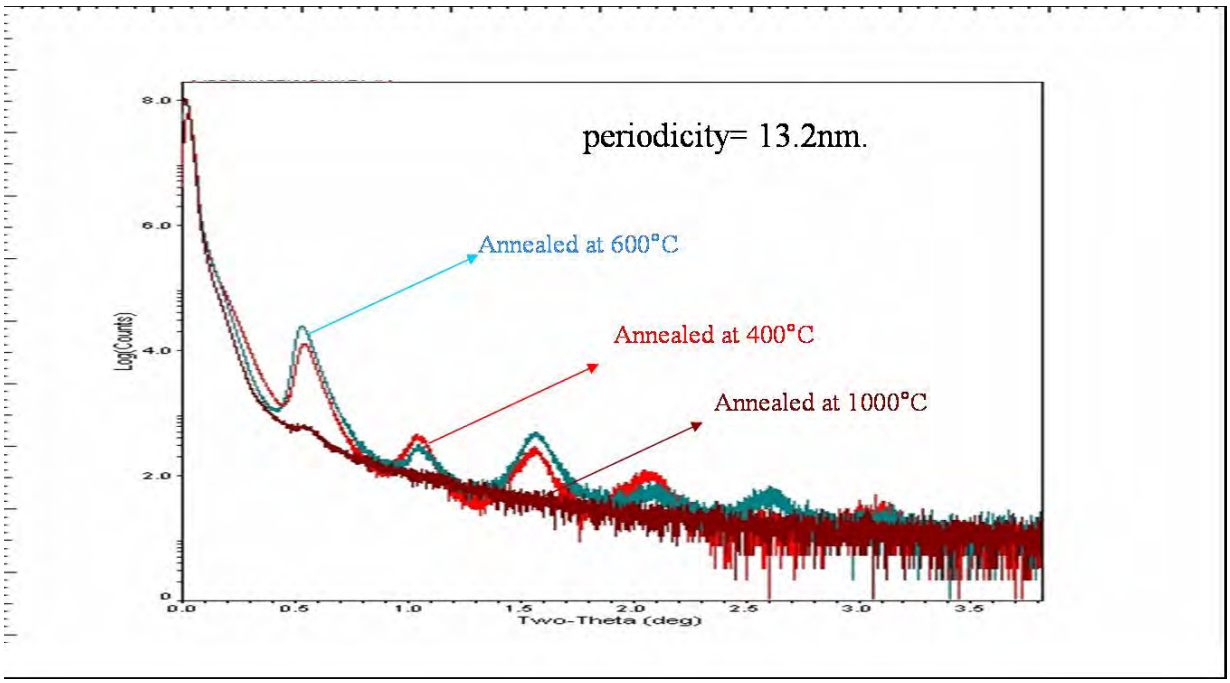

Figure 43. Low angle X-ray diffraction of multilayer sample annealed at 400,600,1000°C.

The multilayer films at 1000°C seem to have lost their peaks. Low angle X-ray diffraction studies are very sensitive to the surface roughness. The loss in x-ray diffraction resolution is possibly due to an increase in surface or interface roughness. Our SEM studies on the surface

and cross section of the coating show that this is the case. Figure 44 (a) shows the surface damage and enhanced roughness from the heat treatment of the sample. Figure 44 (b) shows a cross-section inverted image (substrate towards the top right hand corner) of a deposited sample. Contrasting it with image Figure 44 (a) the damage to the heat treated sample is clear. Our SEM imaging of the cross section at 1000°C does show that the layers are still present. The interface was sharply delineated at 1000°C [70]. It is also important to the note that Ar is not entirely an inert atmosphere and depending on the hydrocarbon impurities it could act as an oxidizing or reducing atmosphere, hence part of the surface damage, or the surface reaction layer, could be traced to the atmosphere. It is however, known that CrN, on oxidation, forms Cr_2O_3 at high temperature and serves as an oxidation diffusion barrier for the lower underlying layers [[71],[18]]. This protects the bulk of the coating from any oxidation damage.

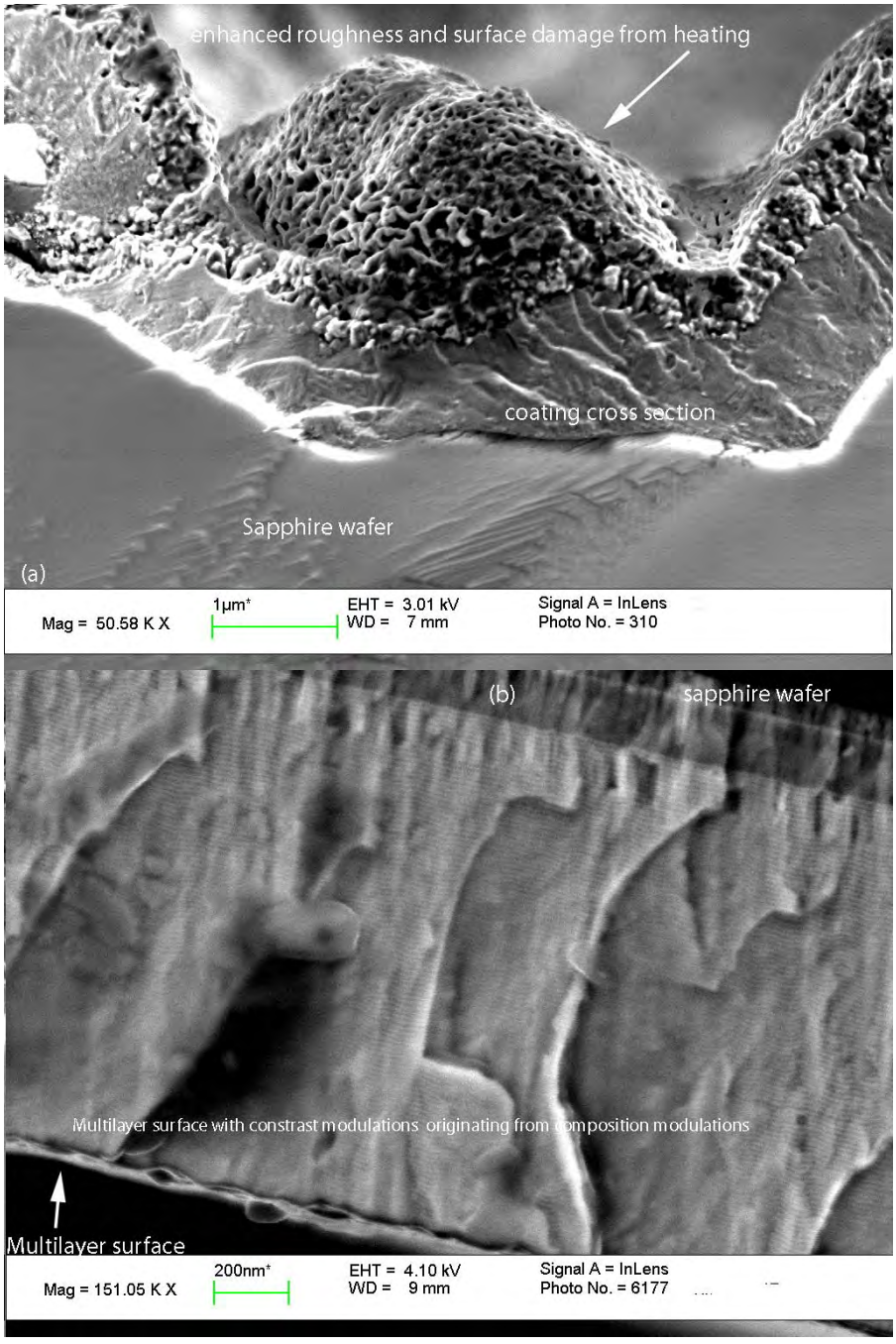

Figure 44. Cross sectional SEM image of CrN/Mo2N multilayers (a) shows the cross section after heating in Argonne up to 1000°C (b) shows the cross section image of the deposited film.

4.5 TGA Studies

Weight loss or gains are generally disruptive processes to coatings and thermal gravimetric analysis is a simple analytical technique that measures the weight loss and weight gain as a function of temperature. Understanding the magnitude and temperature ranges of these effects will allow us to design better coatings. It is important to note here that the films are deposited on Si wafers and the mass plotted on the y-axis is corrected for Si mass gain. The control Si wafer and the Si wafers on which the compounds and the composite are coated are not always the same thickness. This means that a thinner wafer of equal mass will show larger mass gain with temperature than a thicker Si wafer of equal mass (exposed surface area). Hence sharp rises or loss in mass can be attributed to the coating while small mass gain or loss trends could be attributed to substrate effects.

The samples were coatings (~1 μm) samples deposited on Si wafers. The thermal gravimeteric study (Figure 45) on the multilayer shows the protective nature of Cr_2O_3 formed as part of the oxidation process The Mo_2N bulk sample shows mass gain as early as 500°C. At a temperature just around 700°C there is an increased rate of oxidation indicated by mass gain and finally at temperatures above 700°C there is evaporation loss. The temperature regime is consistent with published results [55] The CrN curve on the other hand shows steady mass gain with temperature as the coating and the Si substrate are oxidized (Figure 45)[72]. It is important to note here that the coatings are deposited on a single side polished Si substrate and the unpolished side of the substrate contributes in a substantial but deterministic way to the mass gain of the system. The most interesting of the TGA plots is the curve depicting the effects of oxidation on the multilayer system. The multilayer system shows a steady mass gain up to around 800°C after which there is

a significant mass loss presumably due to the loss of Mo as MoO_3. The mere presence of CrN in the multilayer and its subsequent oxidation serves to shield the lower layers from oxidation damage as its serves as a diffusion barrier [71] and delays the mass loss of Mo by 150°C. The increased mass gain of the multilayer curve over the CrN, Mo_2N or the multilayer coating is due to poor adhesion to the Si wafer and cracking of the film. This leads to the Si surface under the coating being exposed to oxidation and consequent mass gain. Since the substrate effects are substantial Figure 45 is plotted showing the relative mass gain before the correction for Si mass. Figure 46 show the TGA graphs corrected for Si mass gain. Figure 47 (a) and (b) shows the surface of the multilayer after TGA tests. The steady drop in mass of the CrN is due to the differences in thickness of the Si wafer. The graphs have been corrected for mass gain of the Si. This is done under the assumption that the Si wafers were of similar thickness. This is not the case in the CrN sample which was deposited on a relatively thicker Si wafer. Hence for a given mass the control sample (thinner Si wafer) has a larger surface area exposed to oxidation and hence it gains more mass compared to the Si wafer on which the CrN was deposited. Figure 47 (c) and (d) shows CrN and Mo_2N surface after TGA tests. Figure 47 (c) shows the surface damage on the CrN surface while (d) shows that there is significant loss of the coating surface that exposes the Si wafer surface. Some residue of the Mo_2N is still visible.

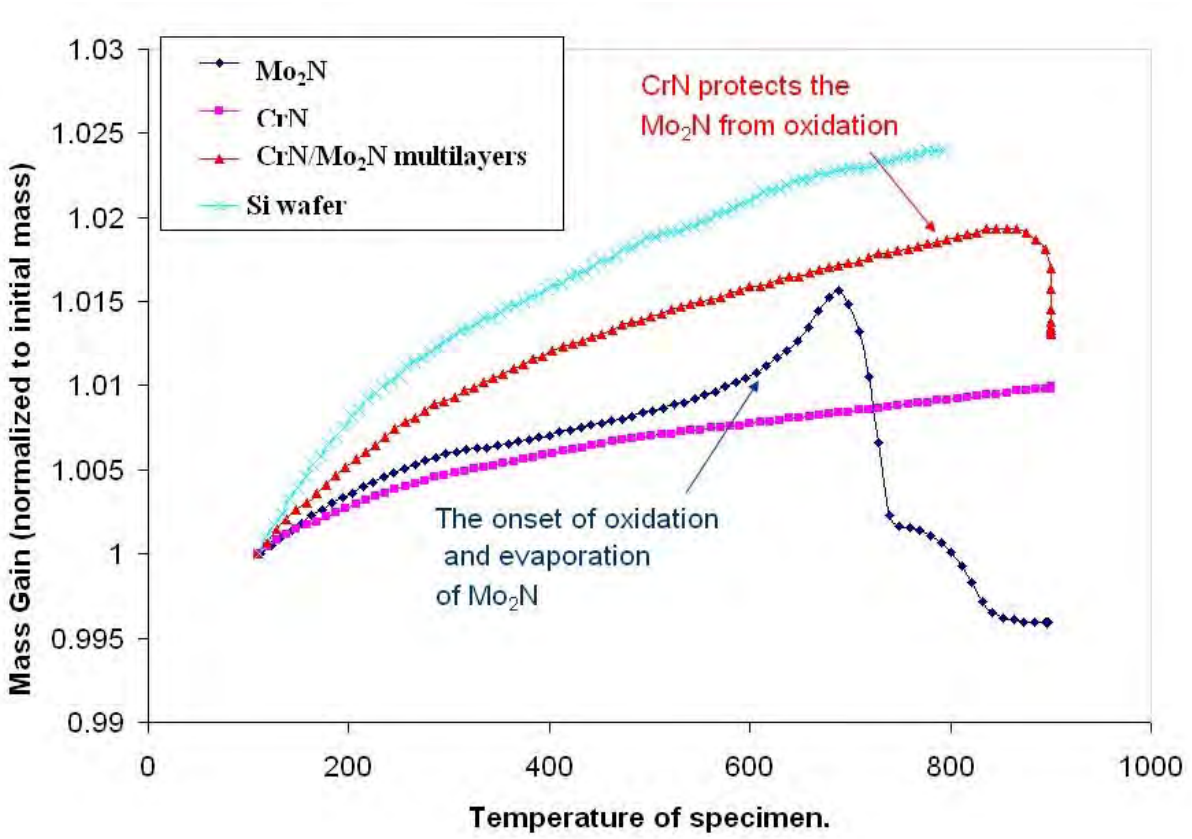

Figure 45. TGA plots of weight gain of the substrate (Si wafer), multilayer sample (CrN/Mo_2N ::4:5), Mo_2N, and CrN.

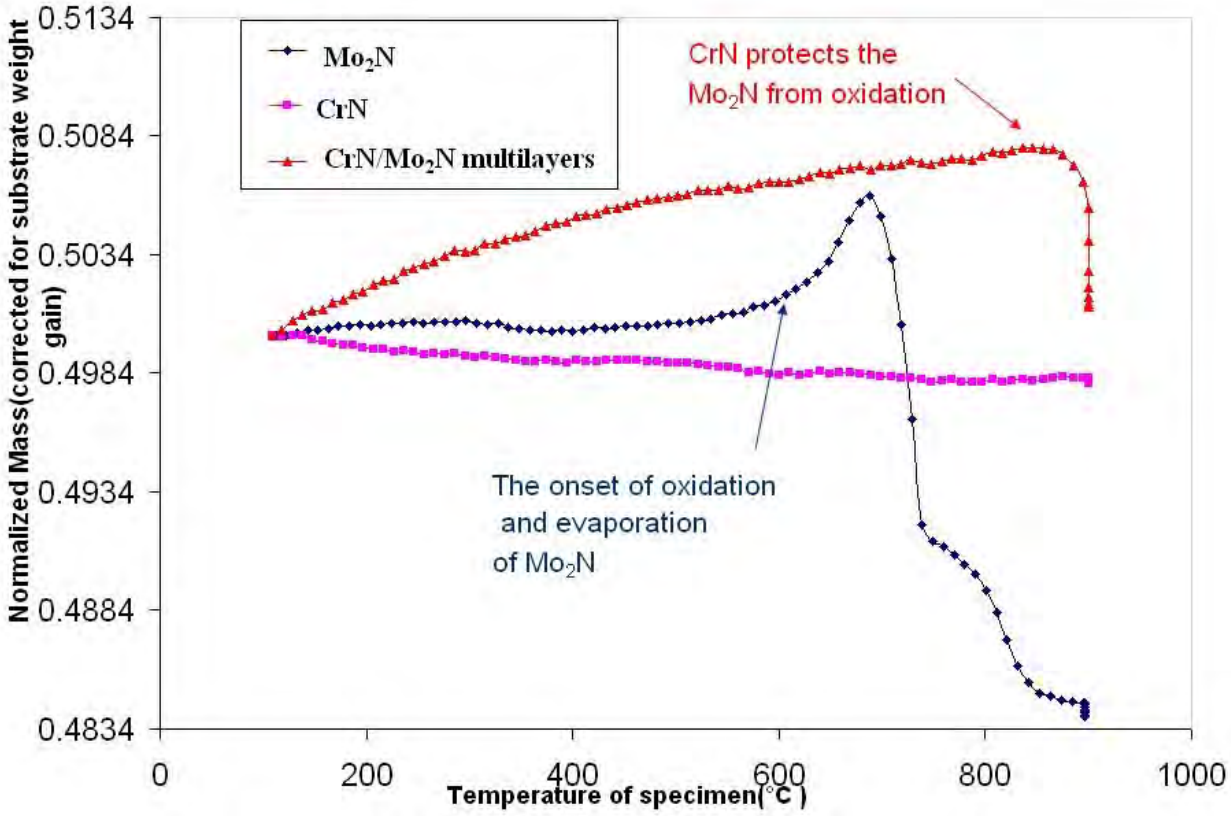

Figure 46. TGA plots of weight gain of the substrate multilayer sample (CrN/Mo_2N ::4:5), Mo_2N, and CrN corrected for the Si weight gain.

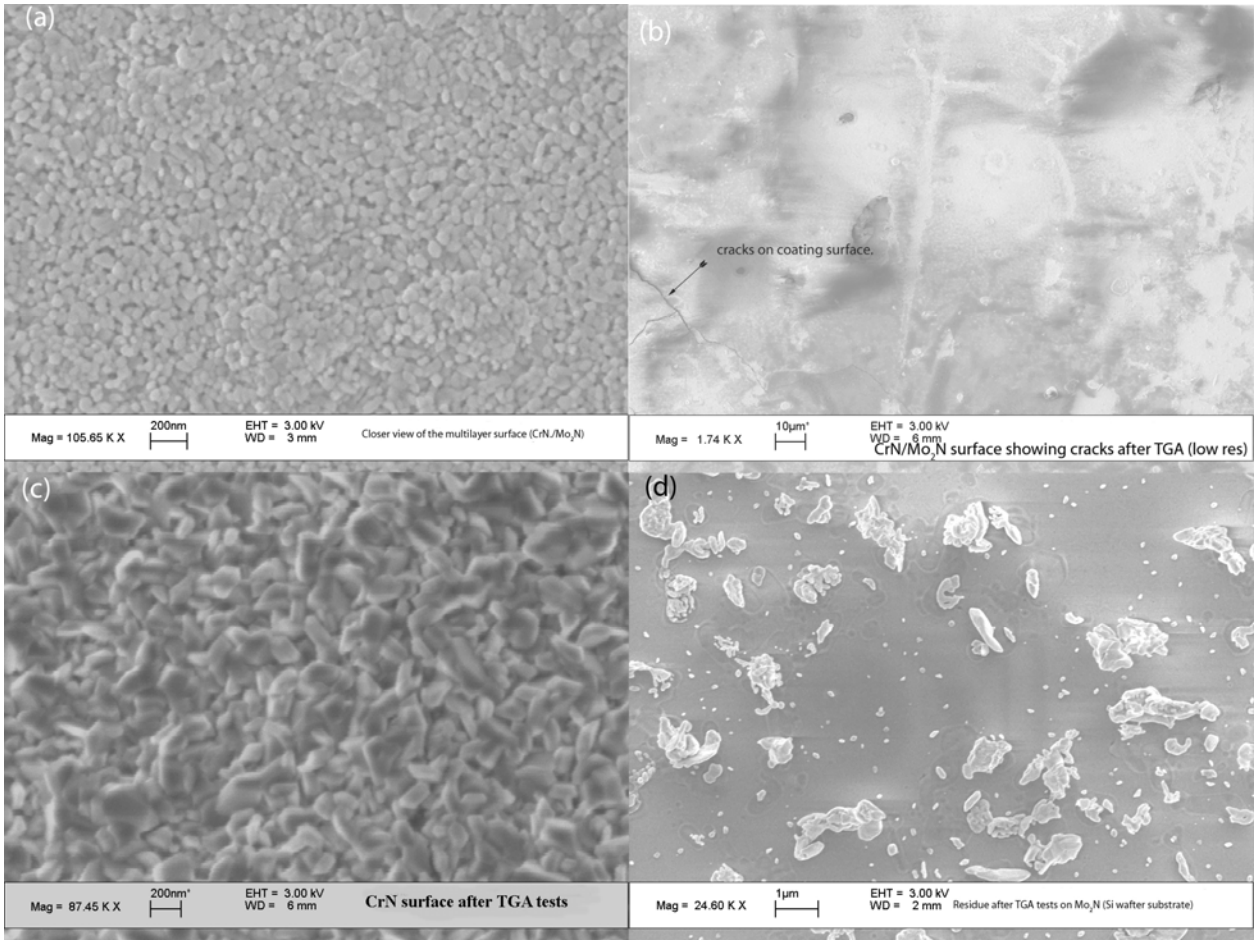

Figure 47. Post TGA SEM images of the coating surface (a) CrN/Mo_2N multilayer surface (high res) (b) CrN/Mo_2N multilayer surface (low res) (c) CrN surface (d) exposed Si surface and left over debris from Mo2N anneal.

The surface morphology of (Figure 47) (a) compared to (Figure 47) (c) shows the difference between bulk CrN and the multilayers. The CrN surface has a relative coarse growth of the oxides as opposed to the multilayer. The nanolayer structure and presumably the nanoscale width of the CrN present seem to lead to a relatively smooth multilayer surface as opposed to the bulk CrN. Given that the films are resistant to fairly high temperatures, it is important that the films are hard enough to withstand wear at high temperature. Our effort in the next section is to investigate the dependence of hardness on composition.

4.6 Hardness Analysis

Our goal is to develop hard coatings that can not only withstand wear but also self lubricate at high temperature. In changing the amount of the lubricant phase in the coating we would not want to compromise on the hardness of the film hence, it is extremely important to characterize hardness as we change composition.. Increasing the relative amounts Mo phase could lead to enhanced lubrication at higher temperature. It is with this goal in mind that coatings were deposited at different Cr and Mo power. Nano hardness tests were then carried out via a UMIS nano-indentor discussed in chapter 2. Figure 48 shows the hardness effects when the relative amounts of Mo_2N is increased in the coating by increasing the power on the Mo cathode during deposition and hence increasing the relative ratios of CrN/Mo_2N from 1:2, 4:5 to 3:10. The bilayer period is decreased by increasing the rate of rotation and consequently dropping the bilayer period from 19 nm to 5 nm. We have learnt from Chapter 3 that changing the bi-layer thickness at a fixed power of deposition of Cr and Mo leads to the hardness being in the general rule of mixtures. We learnt that is the case here (Figure 48) only for the hardness of the 27 nm bi-layer separation. This is the only point that was deposited at 3.5kW of Mo and 2.1 kW of Cr. These were the power levels at which the CrN and Mo_2N hardness were determined. The rest of the points lie outside the rule of mixtures because the power on the Cr target was either lowered (1.5kW) or raised (3.5 kW). The relative softening of the coating is due to the change in power on the Cr cathode which leads to a corresponding lowering of energy on the depositing species and relatively lower flux of Cr species arriving at the substrate. Prior studies on CrN in our lab have shown that crystallinity, crystallographic orientation and hardness are influenced by

depositing power on the Cr cathode[73]. The softening of the Cr phase is expected here and this explains the why the points lie outside the rule of mixtures.

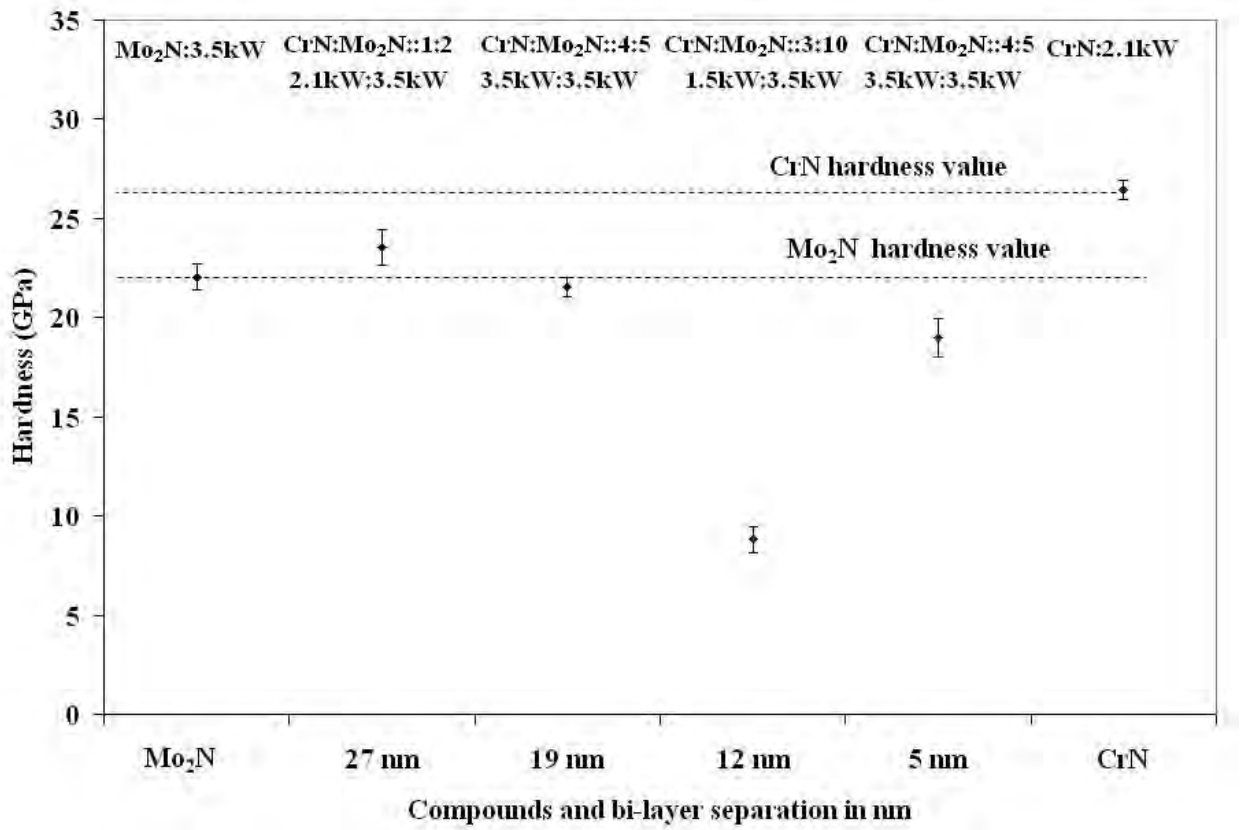

Figure 48. Hardness of CrN and Mo_2N and the different multilayer films. The relative amounts of the phases are represented as a ratio and the power used during reactive sputtering is shown.

4.7 Tribological studies and subsequent characterization of the multilayer films

4.7.1 High temperature friction studies on the Mo_2N/CrN multilayers

Our efforts in this section are to verify if the coating at high temperature provides self-lubrication. Towards this end we will use a high temperature tribometer at Argonne National laboratories, details of which are outlined in chapter 2. High temperature friction tests on the sample were carried out at a 1 cm/s, constant velocity of rotation and a 40 gm load in air. The CrN/Mo_2N ratio is 4:5 and bilayer periodicity is ~13 nm. Figure 49 (a), (b) demonstrate the raw friction vs. number of rotation results at RT and 600°C, these are representative curves from which the steady state friction values are extracted for all the high temperature figures that follow. Figure 50 shows the averaged friction results as a function of increasing temperature.

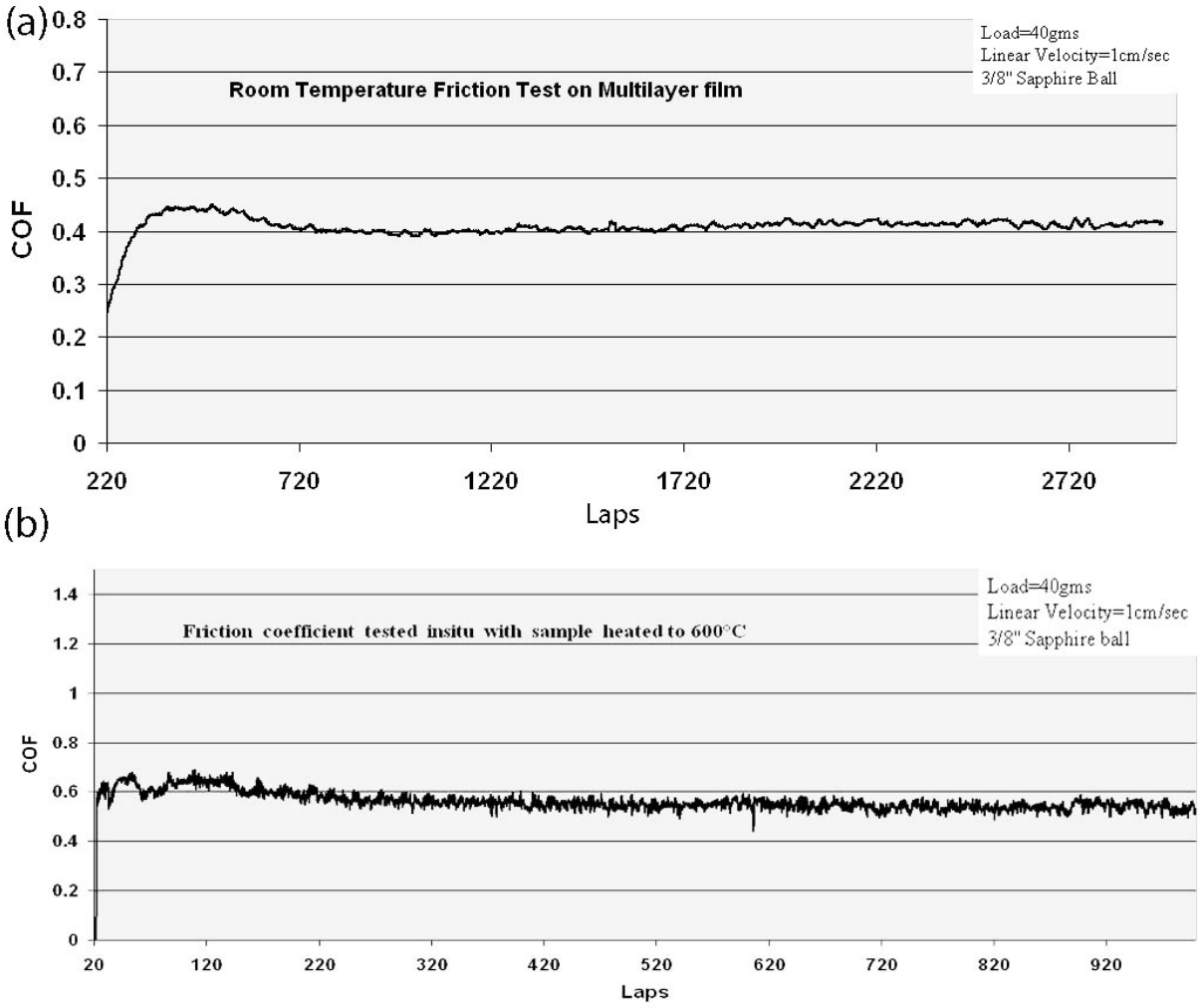

Figure 49. Raw friction plot for multilayers tested (a) RT (b) 600°C.

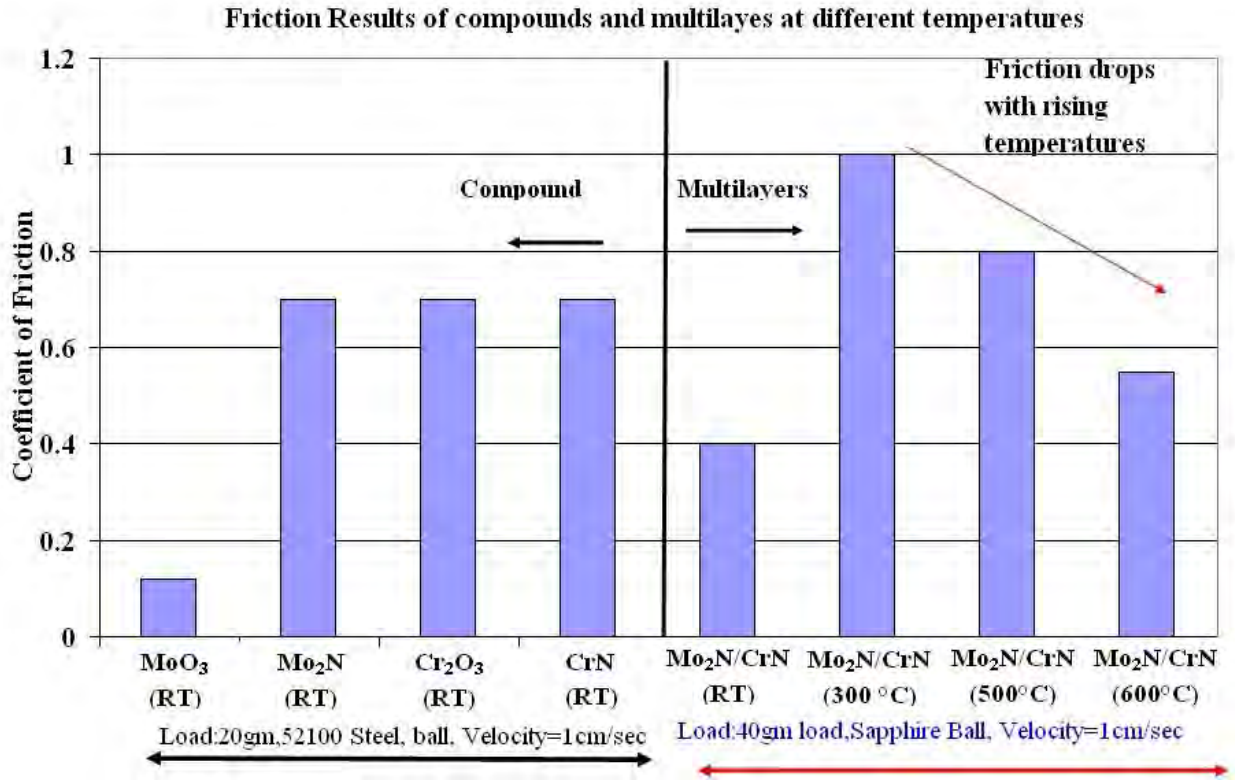

Figure 50. High temperature friction test on Mo2N/CrN multilayer sample in air.

MoO_3 is the low friction phase (COF ~0.16) that we expect to form at high temperature Mo_2N and CrN are constituents of the multilayer films and have relatively high C.O.F's of ~0.6-0.8[74]. The friction tests on CrN, Cr_2O_3 and Mo_2N show a relatively high friction coefficient of 0.7 which is indicative of a metal on metal value, due to abrasive wear of the steel ball. Friction tests on the compounds are discussed in chapter 3. The multilayer tests were carried out with a sapphire ball since it is temperature resistance and the material of choice for high temperature friction tribology studies. Friction tests at 300°C shows increase in friction associated with the formation of abrasive wear particles of CrN, Mo_2N and Cr_2O_3 this is consistent with literature [75].

At temperatures above 300°C, the coating exhibits a lowering in friction. A friction drop of ~20% is exhibited at 500°C and a further drop of ~30% at 600°C. This is a direct demonstration of self lubrication at high temperatures. Figure 51 shows a comparison between the high temperature friction coefficients of the Mo_2N/CrN multilayers and the relatively softer Mo_2N/Cu multilayers [57] and bulk Mo_2N [54]. It highlights the high temperature stability of the Mo_2N/CrN multilayer.

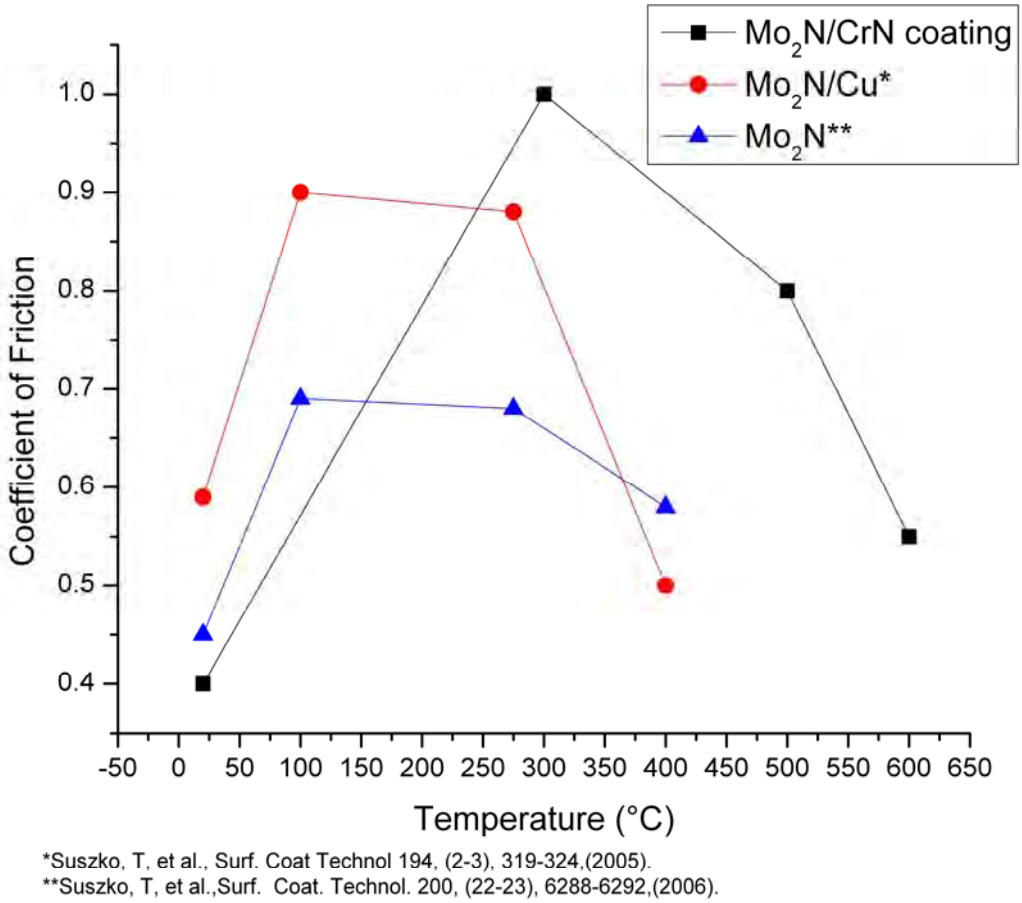

Figure 51. Comparison of the friction coefficients of Mo_2N/CrN, Mo_2N/Cu multilayers and Mo_2N at high temperature.

Compared to the Mo_2N/Cu multilayer, the Mo_2N/CrN multilayers are temperature resistant and offer low friction coefficients up to 600°C which is a full 200°C higher than the highest temperature the Mo_2N/Cu multilayer could withstand. The Bulk Mo_2N shows surface damage due to oxidation at relatively low temperatures of 300°C, the presence of CrN in the Mo_2N/CrN multilayers renders the coating oxidation resistant up to 600°C, which was the limit of the tribometer. The lubricious phase evolving through wear and subsequent oxidation bears a significant role in lowering the friction at high temperature. Figure 52 shows an increase in wear rate at 600°C. The wear rate is independent on the duration of the friction test, number of laps tested and load and offers a comparison between the relative wear at different temperatures. In general the wear rate of the coating in much lower than other reports of hard coatings with self lubrication mechanisms by a few orders of magnitude [76].The higher specific wear rate at 600°C predicts higher wear volumes and this is in agreement with later findings of more transfer particles at 600°C. The wear path shows little or no damage due to the friction test at RT. It is fair to assume that temperature related damage to the coating starts to significantly affect the coating only in the 600°C regime since the wear rates at 300°C and 500°C are comparable. A detailed study on the lubricious film and the wear debris collected from the ball side is included in the following section.

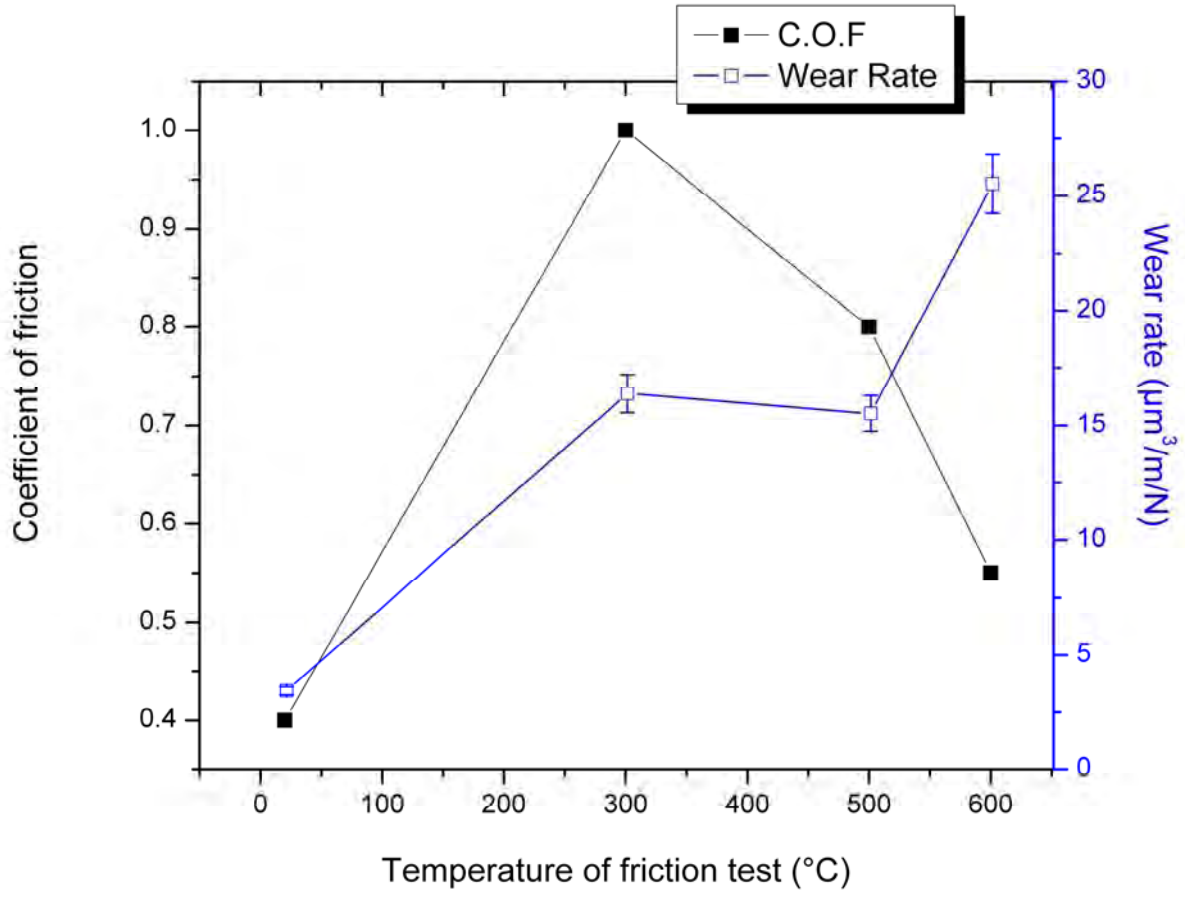

Figure 52. Coefficient of friction and wear rate as a function of temperature of test.

4.7.2 Origin of lubrication in air

To better understand the lubrication mechanism and understand the lubrication mechanism, XPS and SEM analysis are done on the transfer film. The wear debris from the sapphire ball (Figure 53) at 300°C, 500°C and 600°C is transferred onto a sticky carbon tape (Figure 54) and its elemental composition was mapped via E.D.S analysis Figure 55 shows E.D.S elemental maps of the Cr and Mo phase of the wear debris from the ball side. The image shows the transfer film to be Cr and Mo rich which is a result of wear of the coating. Quantitative analysis on the transfer film at 300°C, 500°C and 600°C shows that the relative amount of Mo in the film goes up with

temperature (Figure 56). This figure shows the SEM images of the wear debris at (a) 300°C (b) 500°C and its elemental analysis plots. The transfer film at 500°C and 600 °C consists of nanometer scale agglomerated wear particles , its lower grit size further aid in lowering friction[77]. The transfer film also appears to be layered. This layering could arise because the debris could be shearing along its low slip planes. XPS (Figure 56), studies on the wear debris revealed MoO_3 to be the predominant Mo phase of the wear debris. Figure 57 (a) shows the flatten out wear debris between the sapphire ball and the coating and this wear debris plays a direct role in further reduction of friction at 600°C. Figure 57 (b) is a higher resolution SEM image of one of the wear particles that appears flat. These particles in the tribo-test are found between the ball and the coating in our tests and constitute the so called “third body” that assists in lubrication. In short, the layered structure of the wear debris together with its composition (more Mo) provides more proof of the role MoO_3 plays in lower the friction at higher temperature. An eye-ball estimation of the wear debris collected at different temperatures indicates that amount of wear debris increases with temperature. This points to the enhanced adhesion of the wear debris at higher temperature, this enhanced adhesion is in agreement with literature that reports enhanced adhesion of MoO_3 at higher temperature[55]. MoO_3 is a known low friction phase and its presence is consistent with the related drop in friction coefficient exhibited at high temperatures.

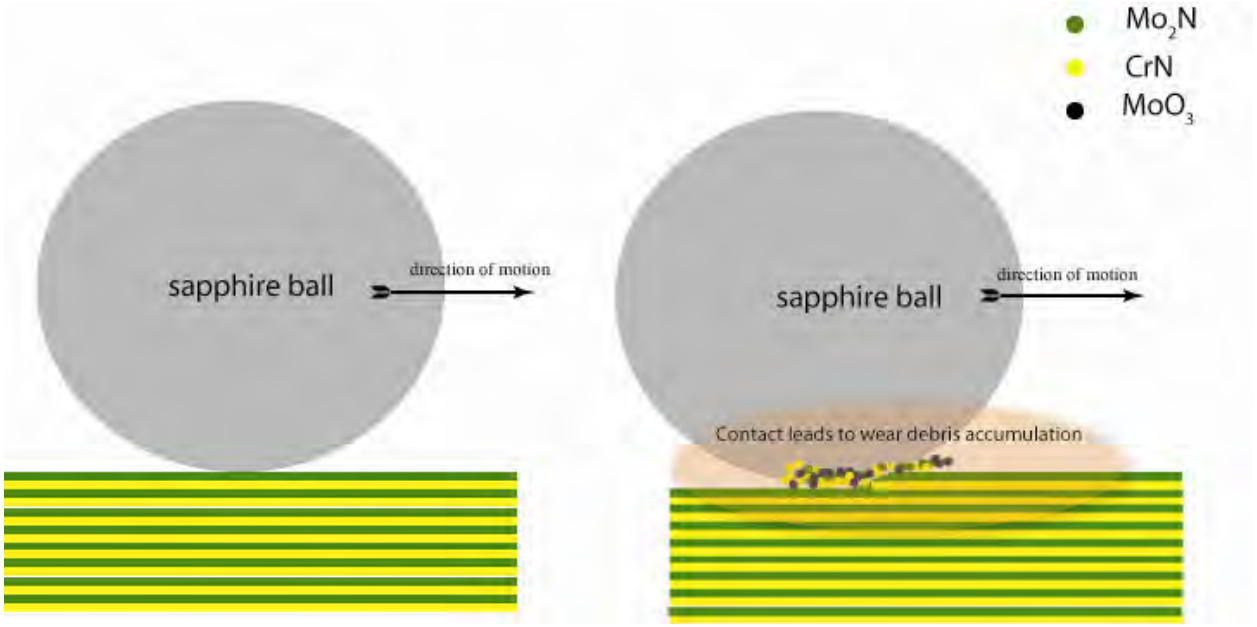

Figure 53. A cartoon representation of the ball on disc contact region showing wear debris accumulation.

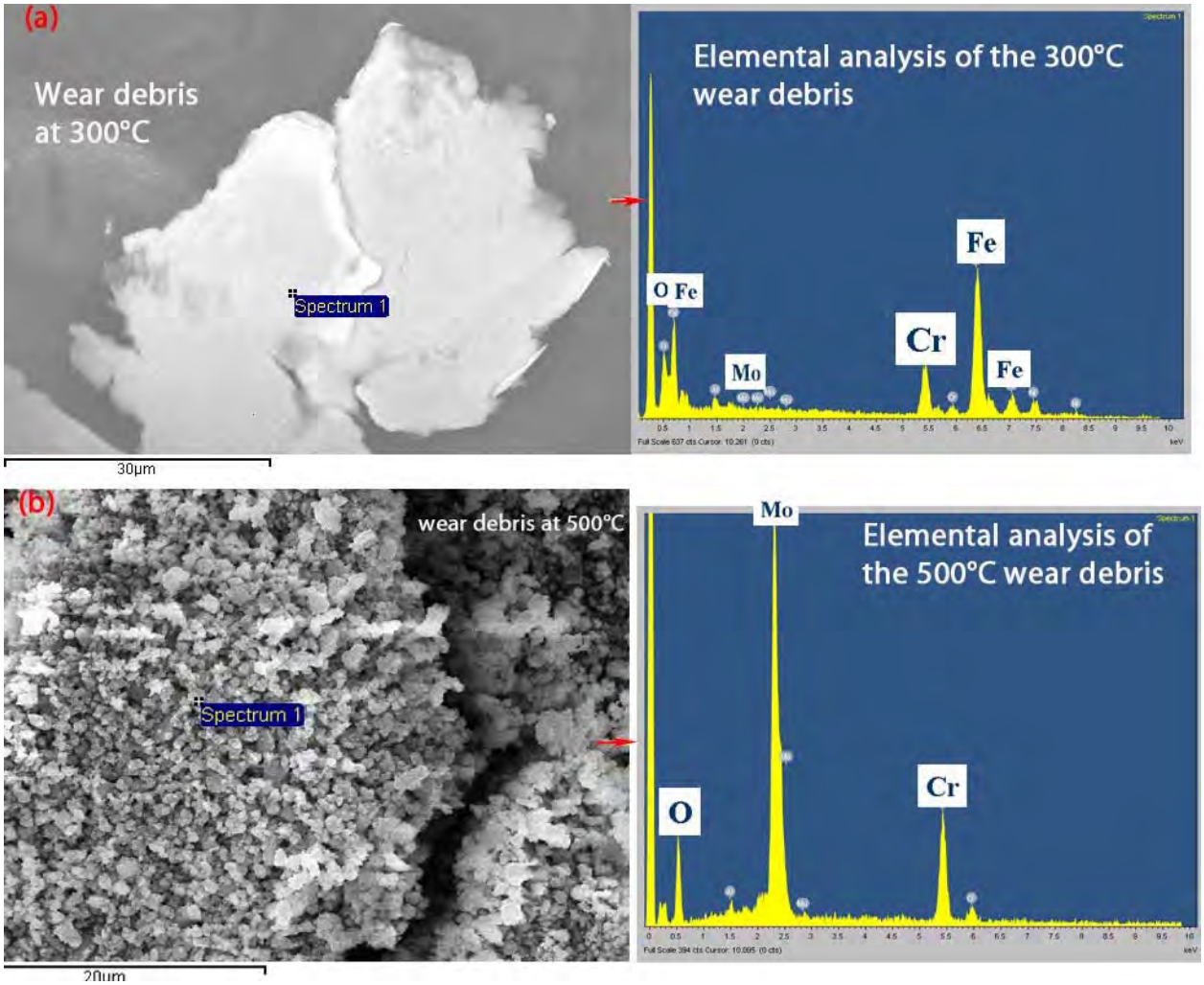

Figure 54. SEM images and its corresponding EDS elemental analysis of wear debris collected at (a) 300°C (b) 500°C (c) 600°C .

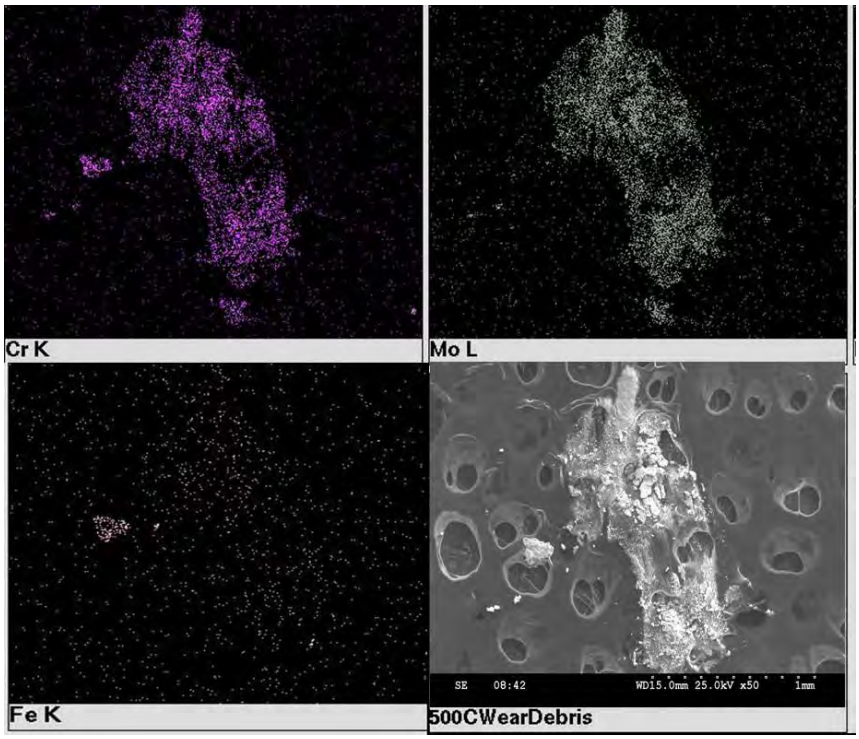

Figure 55. Elemental mapping of Cr, Mo and Fe of the transfer film from the ball side.

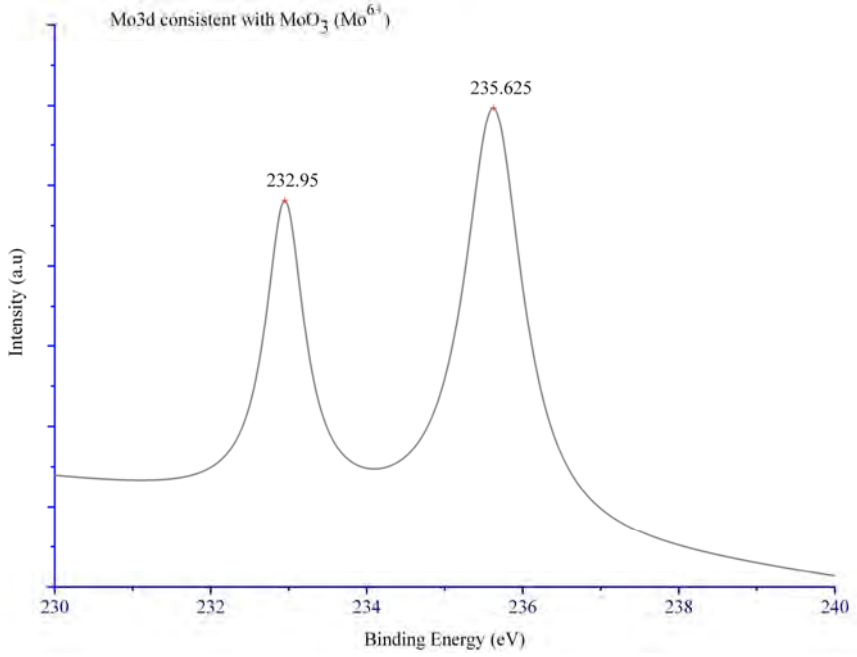

Figure 56. Curve fitted XPS data. Analysis was carried out on wear debris collected after the friction test at 500°C.

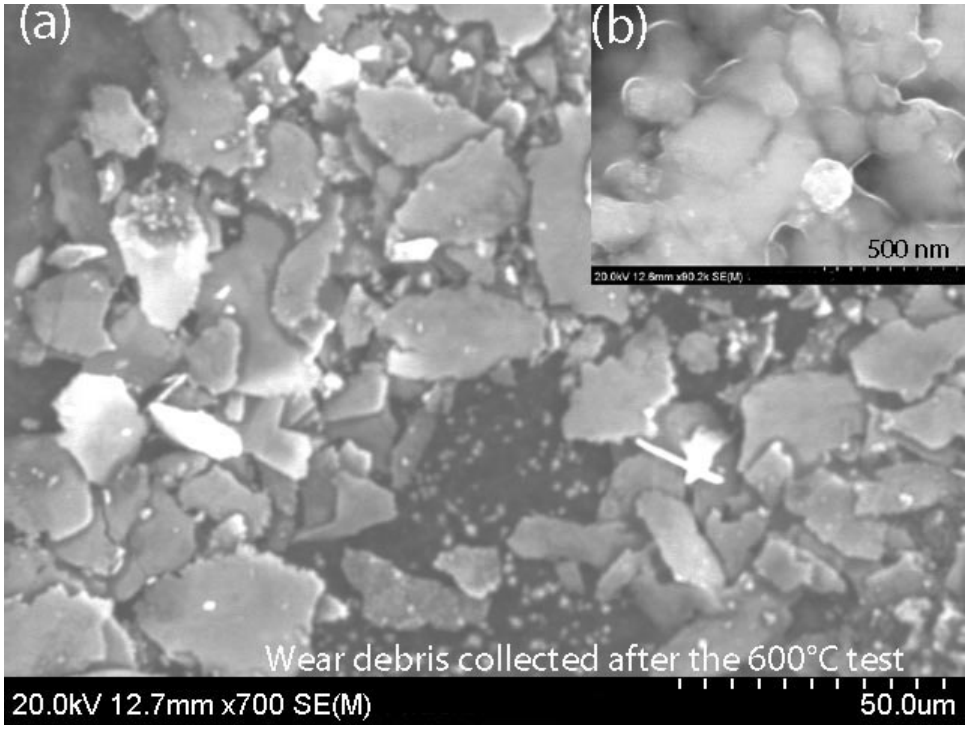

Figure 57. SEM images of wear debris collected from the ball side after the friction test at 600°C (a) lower resolution image (b) higher resolution images of one of the particles from (a).

SEM micrographs on the coating surface away from the wear track (600°C) shows the presence of a lamellar molybdenum rich phase (Figure 58). These SEM images are consistent with prior reported oxidation studies of Mo_2N [55]. This offers further evidence of the formation of MoO_3 on the coating surface. This surface evolution in the wear track provides the in situ lubrication.

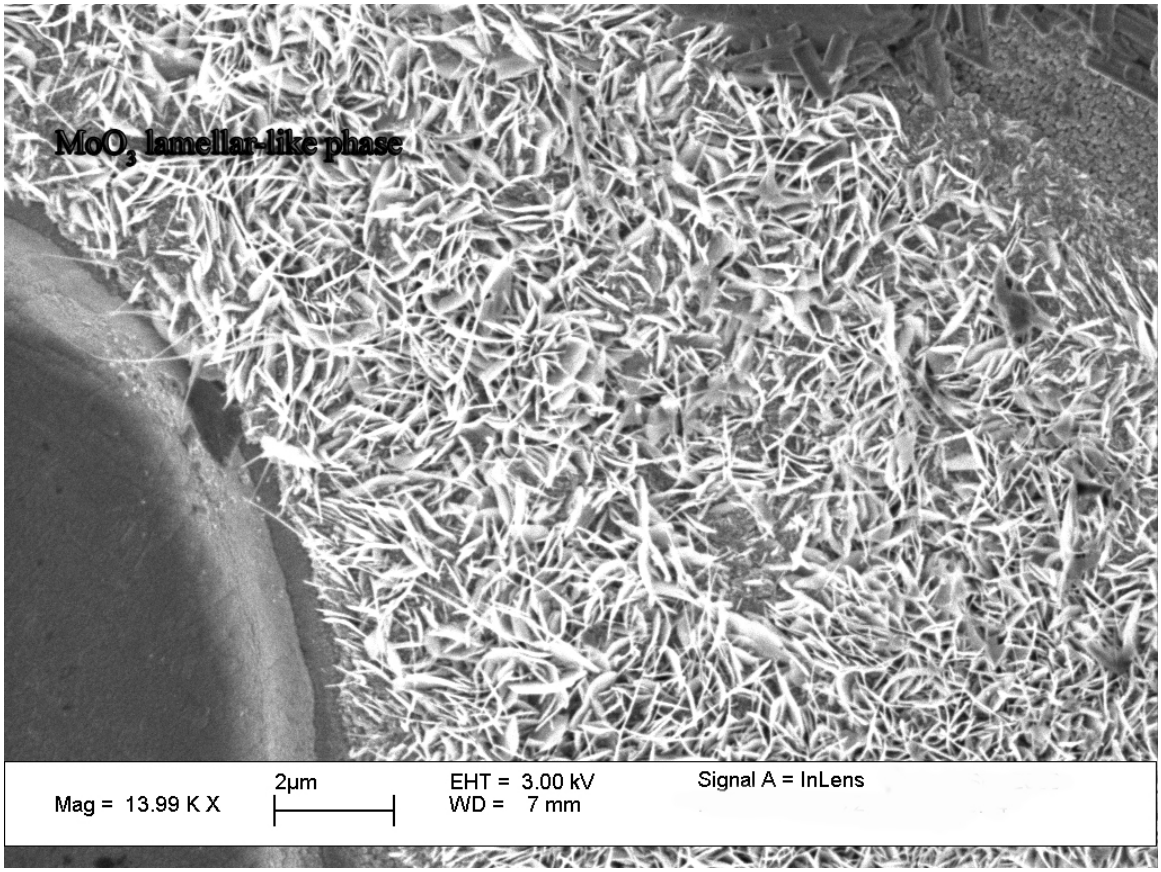

Figure 58. SEM image of the evolution of the lamellar MoO_3 phase on the surface of the multilayer coating.

4.7.3 SEM studies on the wear track.

Studies on the wear track will offer better insights into how the wear track and the lubricious wear debris in the wear track contribute to the lower of friction at high temperature. Figure 59 shows SEM images of the wear track at different temperature. The images (a), (b), (c) and (d) show an increasing trend in the amount of wear debris with temperature. Increasing film thickness in the wear track (when lubricious) reduces the adhesion contribution to the net friction coefficient. With rising temperature, the wear debris becomes increasing made up of soft materials with low shear planes (MoO_3). At room temperature the coating surface shows almost no damage with grain size of the coating clearly visible and relatively small amounts of wear

debris. Figure 59 (b) shows the wear track on the coating at 300°C, the amount of material accumulated due to wear in the track has increased. The wear debris is mainly composed of worn CrN and Mo_2N particles which contribute to increase in friction by ~150%. In short the transfer film is abrasive. Any lamellar MoO_3 formed at these temperatures are brittle and show insufficient adhesion to the native nitride. It has been shown in other studies that their softening with temperature results in better lubricating performance[57]. Our findings are similar.

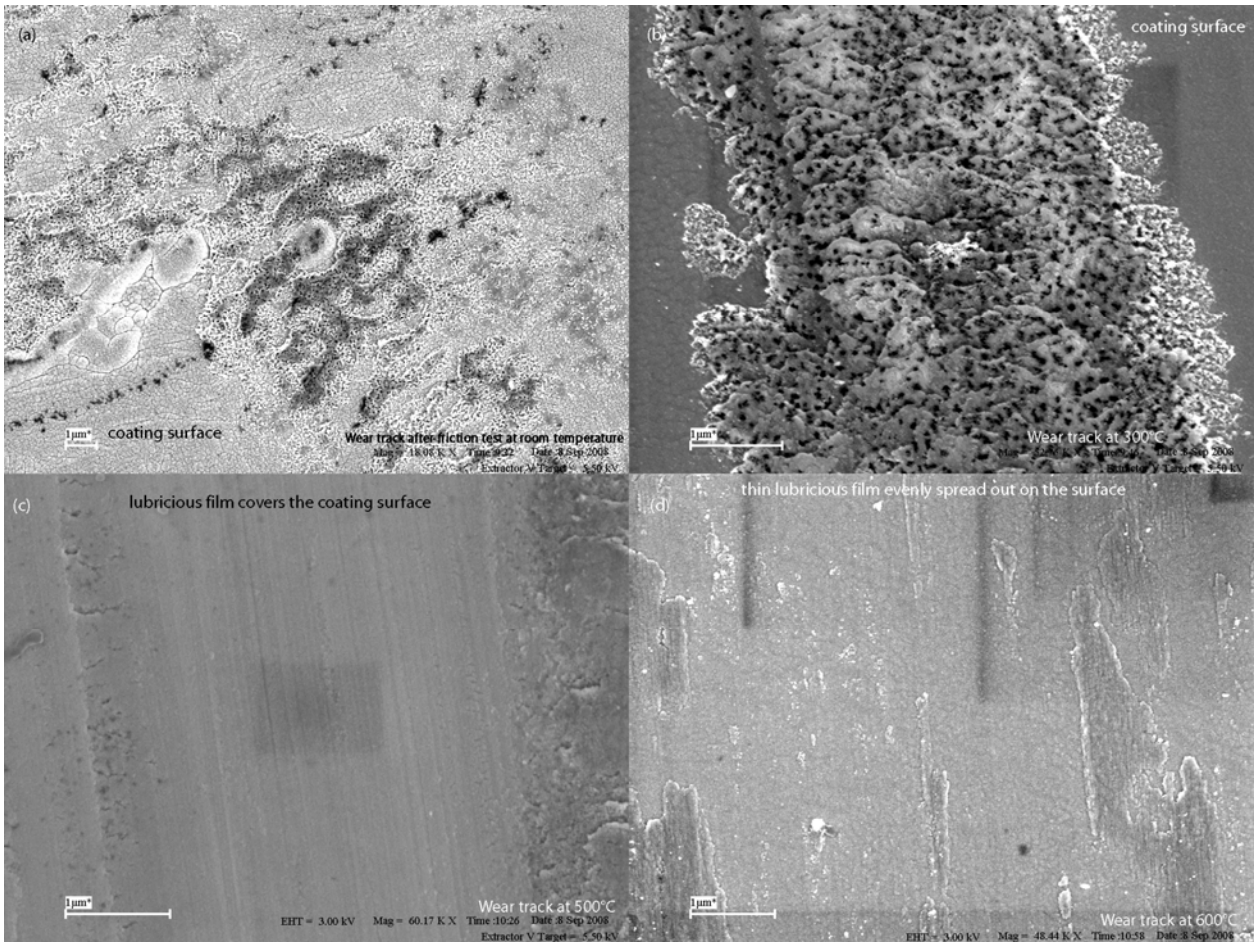

Figure 59. Wear tracks of high temperature friction tests (a) room temperature (b) 300°C (c) 500°C (d) 600°C.

At higher temperatures of 500°C and 600°C, the nature of the wear track changes significantly with the lubricious material smeared down and forming a thin continuous film. At 600°C the

film is extremely thin with the underlying grains visible through the films. Thin lubricious films offer lesser viscous drag [78] to the surface and lead to very low wear rates. E.D.S studies show that the Mo is present in relatively higher amounts at 500°C than at 300°C. In short the oxidation products of Mo assist in lowering the friction at higher temperatures.

4.7.4 High temperature friction studies on the Mo_2N/CrN multilayers in air and N_2

The tests were carried out in industrial N_2. Limitations of the equipment and impurities in the N_2 gas (5 ppm O_2) make us conclude that the atmosphere is only "near nitrogen" and has nominally about 2-5% of oxygen contamination. Although for convenience the following sections will refer to the test in the "near N_2" just as test in N_2, due note should be made of the 2-5% oxygen contamination level. More instrumentation details of the high temperature tribometer is included in chapter 2.

Our primary aim in carrying out the tests in nitrogen was to eliminate oxygen in the atmosphere and prevent the formation of the low friction MoO_3. The results obtained were surprising since the friction was expected to increase, presumably since the lubrication mechanism (oxidation) would not operate in the absence of oxygen. The results showed that the friction dropped even further in the N_2 atmosphere. Figure 60 demonstrates this increased drop in friction. The CrN to Mo_2N ratio is 4:5 and the tests are carried out from RT to 600°C. As we test our sample from RT to intermediate temperatures of 300°C there is an initial rise in friction due to the evolution of hard wear debris especially particulate CrN, Mo_2N and the highly abrasive Cr_2O_3. This increase in friction at intermediate temperatures of 300°C is seen in all of our high temperature friction tests and is consistent with multilayer high-temperature tribo-tests in literature where one of the constituents phases in the wear debris is abrasive[57, 79]. Our friction tests carried out in

nitrogen shown in Figure 60 show a similar trend of intermediate rise and eventual lowering of friction. In our friction tests on multilayers with CrN/Mo_2N::3:10 we see a similar trend.(Figure 61, Figure 62). The friction does not seem to be any discernable dependence on the relative ratios of CrN/Mo_2N (within the ratio range of our tests) although across the board the friction values at high temperature were lower in N_2 than in air. Although it is unclear exactly why the friction is lower at high temperature, a few possible explanations will be discussed in the following section.

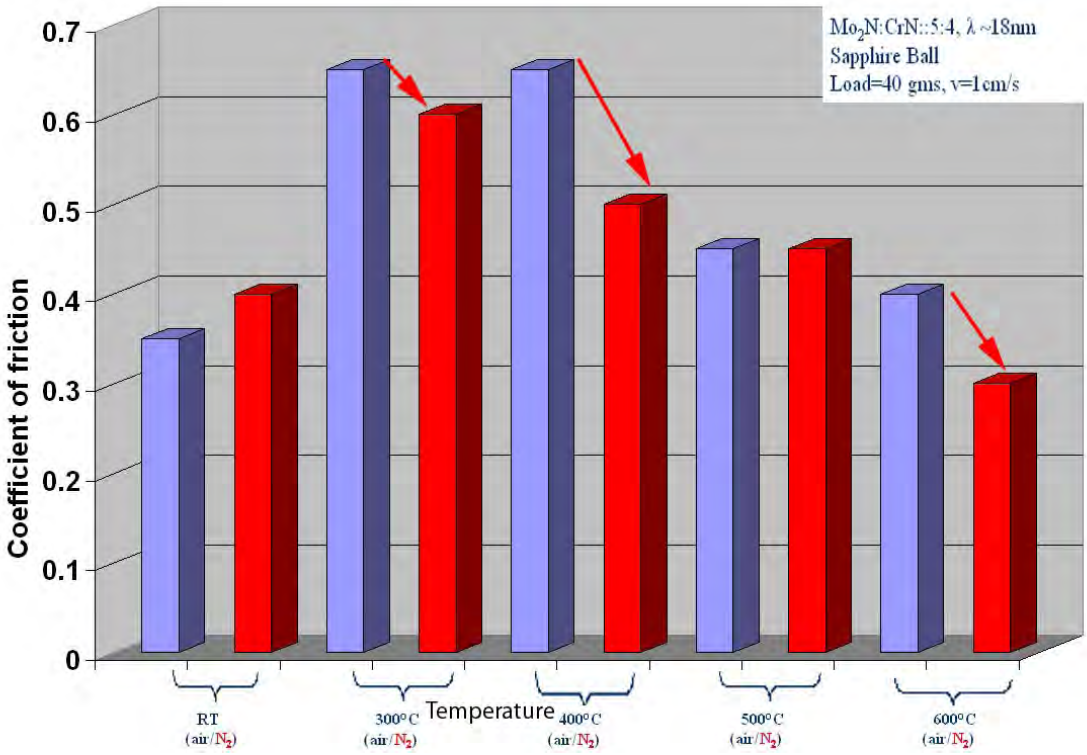

Figure 60. High temperature friction tests of the CrN/Mo_2N:4:5 (λ ~18nm) multilayers in air. The friction values at a specific temperature in air and N_2 are reported side by side with air on the left hand and N_2 on the right hand side. The friction values in nitrogen are recorded when the race track and the sapphire ball region is flushed with Nitrogen.

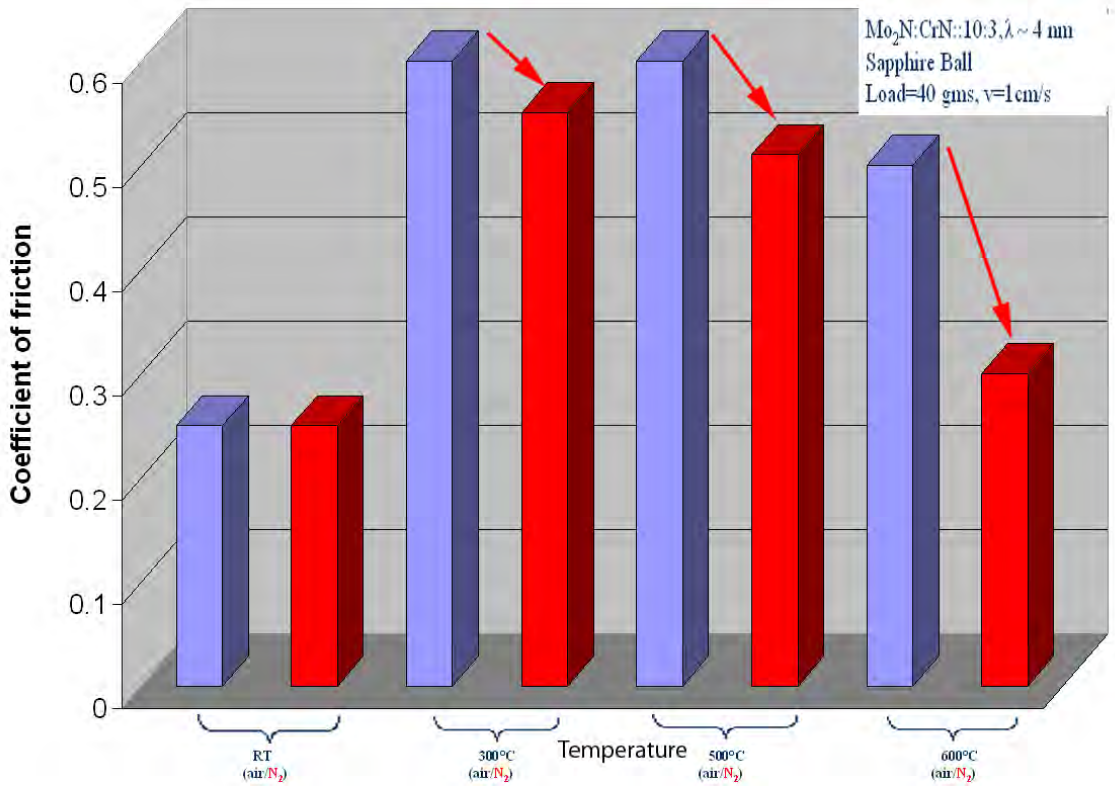

Figure 61. High temperature friction tests of the CrN/Mo_2N ::3:10 (λ ~ 4 nm)multilayers in air. The friction values at a specific temperature in air and N_2 are reported side by side with air on the left hand and N_2 on the right hand side. The friction values in nitrogen are recorded when the race track and the sapphire ball region is flushed with Nitrogen.

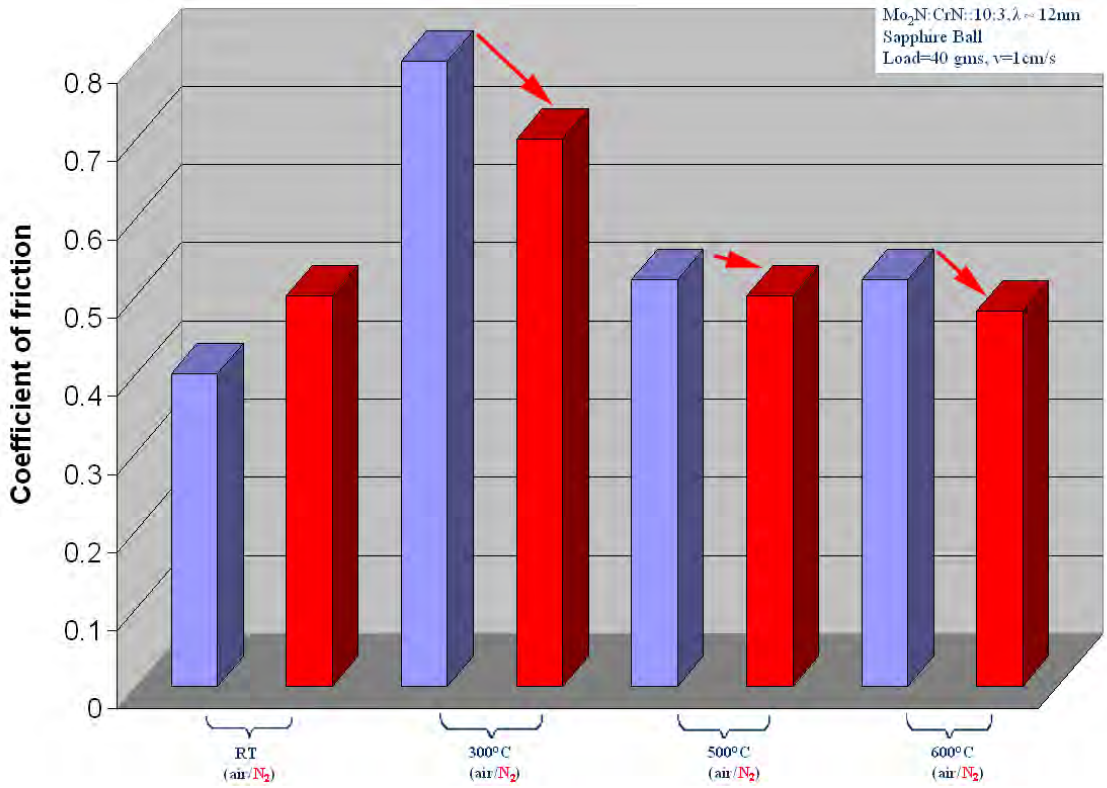

Figure 62. High temperature friction tests of the CrN/Mo_2N::3:10 , (λ ~12 nm)multilayers in air. The friction values at a specific temperature in air and N_2 are reported side by side with air on the left hand and N_2 on the right hand side. The friction values in nitrogen are recorded when the race track and the sapphire ball region is flushed with Nitrogen.

4.7.5 Studies on the wear surface of the samples tested in N_2

In the analysis on the wear debris and the wear track were inconclusive since no experiment evidence pointing to a phase or a mechanism, that could readily explain the enhanced lubrication in N_2, was identified. It is prudent to offer some ideas on why this behaviour is exhibited. The lowering of friction in N_2 environments is related to lower partial pressures of oxygen in the ambience. The nitrogen tests were carried out in industrial grade dry nitrogen. Industrial nitrogen has trace amounts of O_2 (~5 ppm) and CO (~3 ppm) and our experimental set up does not do a great job of eliminating oxygen (refer chapter 2). In this near N_2 atmosphere, there is limited availability of O_2 and relatively less oxidation of the coating surface. Surface studies on the CrN/Mo_2N (3:10, λ=12 nm) surface both in air and nitrogen is particularly insightful to understanding the relative oxidation damages on the surface. Figure 63 shows SEM images of the surface. Figure 63(a) shows an deposited Mo_2N/CrN surface. The top view of the grains is a result of the columnar growth is clearly apparent. Figure 63 (b) shows the minimal oxidation damage to the surface as a result of the tests in nitrogen. The image shows oxide growth on the grains ~20 nm in the longest dimension. On the other hand the Figure 63 (c) and (d) show surface images of oxidation damage on the samples tested in air. The longest dimension of the damage is ~90 nm. The lamellar wear debris is clearly apparent at 600C in N_2 (Figure 64).

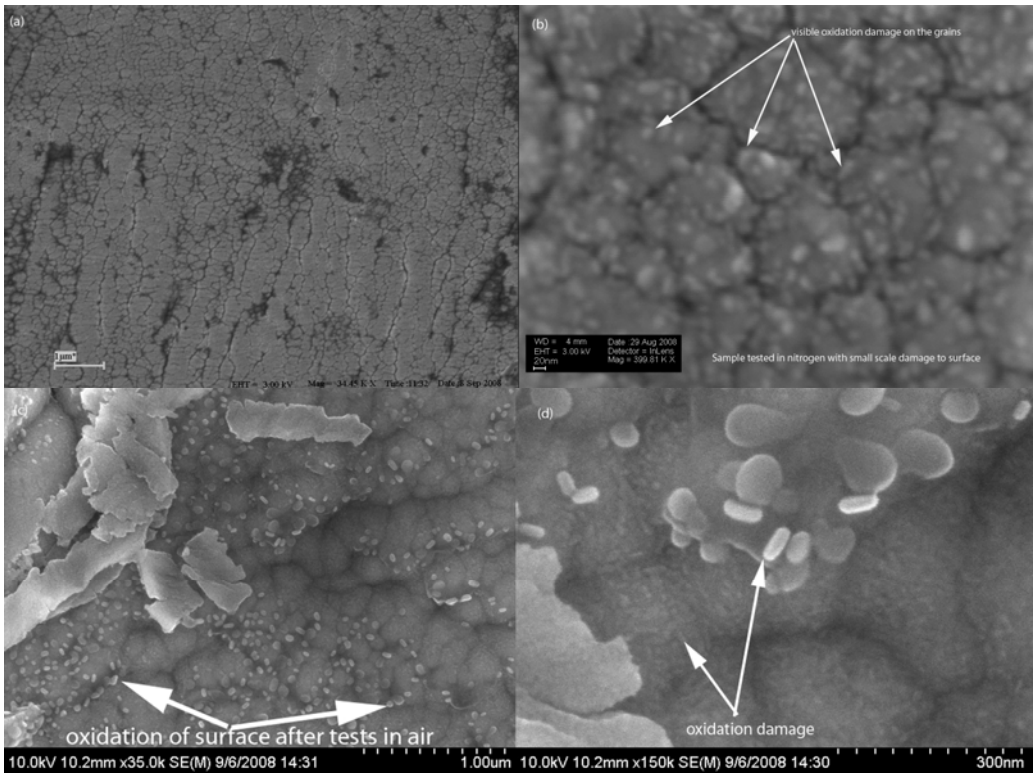

Figure 63. SEM view of the coating surface before and after oxidation (a) as deposited surface (b) surface tested in nitrogen (c) surface tested in air low resolution (d) surface tested in air higher resolution

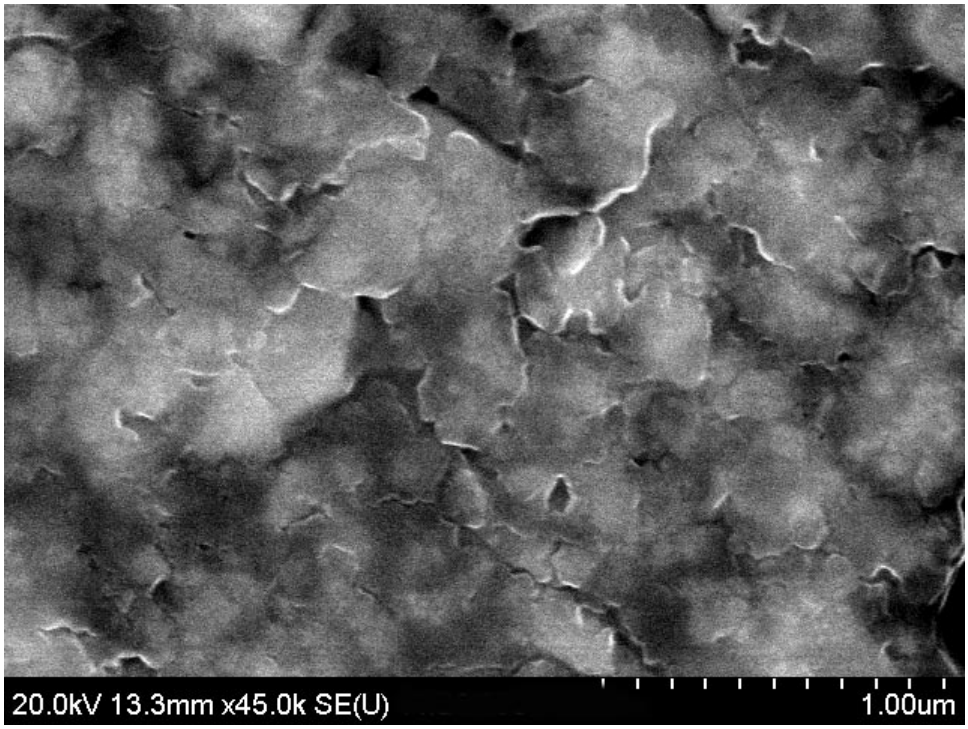

Figure 64. SEM image of the lamellar wear debris at 600°C in nitrogen.

The oxide growth in the N_2 is a small fraction of the grain size whereas in the samples tested in air the oxide growths are in some cases about the size of the grain. The surface of the coating appears less damaged by the heat (Figure 65) and is devoid of the breakouts and surface defects present in abundance on the samples tested in air. These images are on virgin surfaces away from the wear track but the condition in the wear track could be entirely different, yet we can definitively say that the amount of oxygen in the atmosphere plays a direct role in the oxidation damage to the surface and influences the amounts of the lubricious phase in the wear track. In the following section some ideas will be put forth on the possible origins of the enhanced lubrication in N_2.

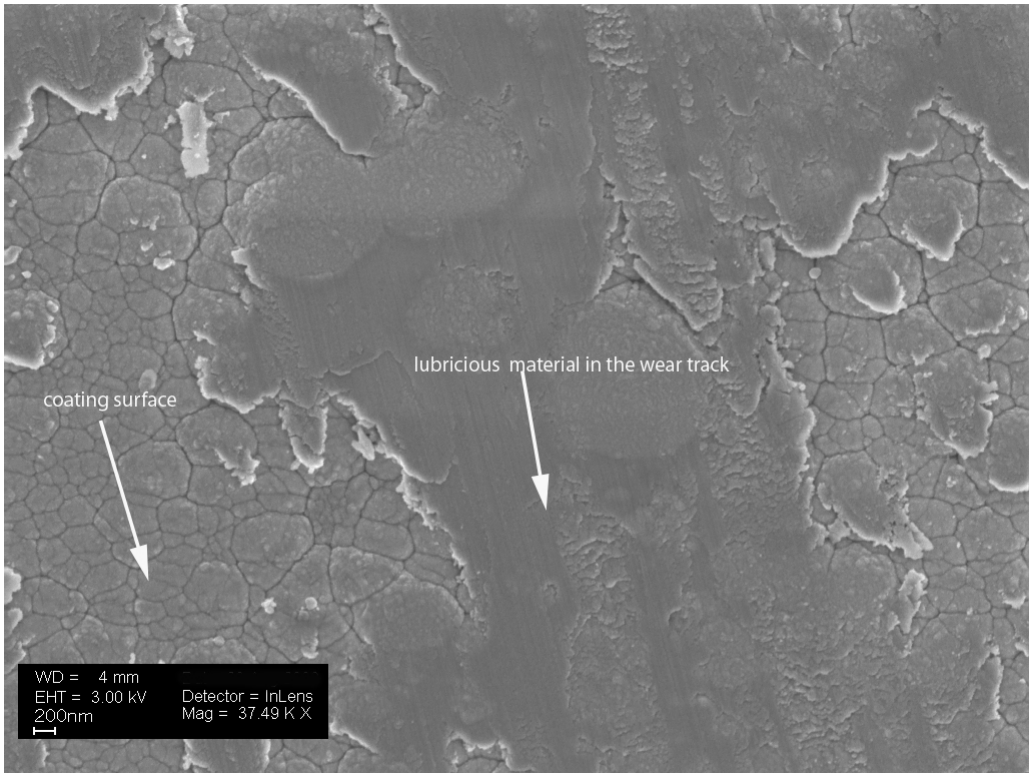

Figure 65. SEM image of the smeared in lubricating soft-phase in the wear track.

7.4.6 Possible reasons behind the origin of enhanced lubrication in N_2

Similar tests by other researchers at elevated temperature on the low fiction phases of Mo have confirmed the presence of Magnéli phases [54, 57, 80]. It has been found that the best lubrication performance is shown by oxygen deficient oxides- Magnéli phases[81], exhibited even in other metal systems such as (Ti, V and W)[82]. Phases of the form Mo_nO_{3n-1} has been shown to have planar faults[83]. A schematic of the shear planes of the possible phases of Mo is shown in (Figure 66). Stabilization of these phases in atmospheric conditions is difficult and this could be the reason why the tests in atmospheric conditions are relatively higher[84].

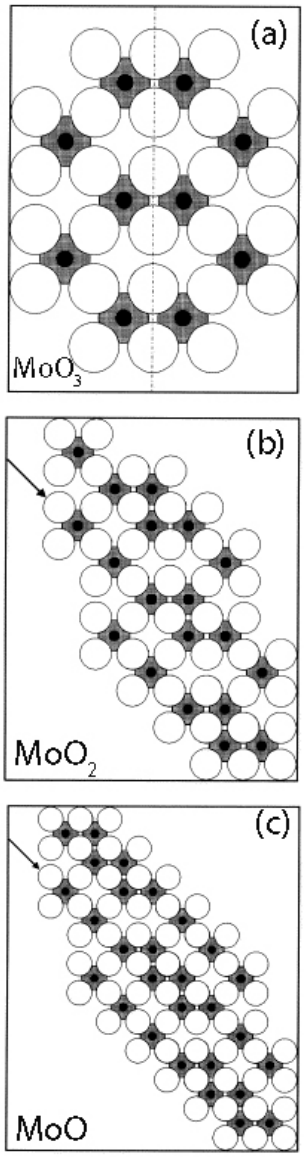

Figure 66. Structure of oxygen-deficient Magnéli-phases and the resulting crystallographic shear planes (a) MoO_3 type (b) MoO_2 type (3) MoO type.(after Lugscheider,2000).

The relative thickness of the lubricious layer coating could one of the contributing factor in lowering the friction. A closer examination of the wear track in Figure 59 (d) (600°C) shows the wear track to be relatively thin with the underlying grains visible. This relatively thin layer of lubricious film could play a role in the lowering the friction of the coatings [85, 86]. Nanometer

scale lubricious film thickness have, in some case, shown to reduced friction by an order of magnitude.[78]

4.8 Conclusions and discussions

Multilayers of CrN and Mo_2N were deposited at different power settings and different substrate rotation speeds to vary the relative amounts of Cr and Mo. The change in the power settings lead to deviations from the rule of mixtures in the hardness values. The changes in sputtering rates (from power level changes) affect the bombarding ion to depositing species ratio, which in turn leads to depressed hardness numbers (Cr ,Mo) [36]. This is a well understood phenomena [56]. TGA studies show that the CrN in the coatings acts as a diffusion barrier to oxygen and protects the underlying Mo_2N from oxidation. This consequently makes the coating withstand higher temperatures without oxidation and related mass-loss.

The concept of self lubrication at high temperature was demonstrated in CrN/Mo_2N multilayer films. Friction tests at high temperature on the multi-layer samples show a temperature activated self lubricating mechanism.. MoO_3 is the lubricious oxide forming at high temperatures. There is an increase in the amounts of MoO_3 in the wear debris at high temperature (>500°C) compared to the wear debris at RT and 300°C. This is indicative of more oxidation with temperature and enhanced adhesion of the MoO_3 to the sliding sapphire ball. This is in good agreement with other studies that show similar temperature induced enhancements in adhesion of the MoO_3 [55].

The friction results of the samples tested in N_2 at higher temperatures were lower than the friction results in air. The N_2 atmosphere has ~5 ppm of oxygen and hence does not completely prevent the oxidation of the CrN and the Mo_2N phases, but certainly plays a role in limiting the

oxidation rates due to the lower amounts of oxygen in the environment. Special environments could offer a method to control the lubricating efficiency of these coatings.

Although the exact mechanism of the enhanced lubrication in the N_2 atmosphere was not completely understood, the presence of lower lubricating regimes where other oxides of molybdenum (of the Mo_nO_{3n-1} type) play a significant role in lubrication is widely reported [54, 57, 80]. The results in N_2 are in good agreement with these reported results, in which Mo_nO_{3n-1} phases shows enhanced lubrication [81]. Hence the possibility of formation of Magnéli phases of Mo cannot be discounted.

The relative quantities of the lubricious phase would also influence friction [78]. The coatings show less oxidation damage in N_2 atmosphere and hence the amount of oxides forming on the surface in N_2 is certainly lower. It is well documented that thinner coatings assist in lower friction regimes[78]. A thicker coating would offer more viscous drag to the sapphire ball as it slides on the surface.

The presence of Cr_2O_3 at higher temperatures (500°C and 600°C) in addition to MoO_3 cannot be discounted. The free energy of formation of Cr_2O_3 (-857 kJ/mol) and MoO_3 (-633.2 kJ/mole) is calculated from the reactions below.

$$2CrN + \frac{3}{2}O \longrightarrow Cr_2O_3 + N_2 \quad \Delta G_{300K} = \text{-857 kJ/mole} \quad (15)$$

$$\frac{1}{2}Mo_2N + \frac{3}{2}O_2 \longrightarrow MoO_3 + \frac{1}{2}N_2 \quad \Delta G_{300K} = \text{-633.2 kJ/mole} \quad (16)$$

The free energy of formation of Cr_2O_3 relative to MoO_3 is lower, and hence its formation is certain. Although the rate of formation of Cr_2O_3 could be much lower than MoO_3 since the rates

of oxidation of CrN is reported to be atleast 2 orders of magnitude lower than TiN a more temperature stable phase than Mo_2N [87]. In short the formation of Cr_2O_3 while relatively low cannot be discounted. The Cr_2O_3 phase is an abrasive phase and its presence in the wear debris could be detrimental to the self lubrication initiated by the oxides of Mo at high temperatures. It is quite conceivable that the absence of the abrasive phase (Cr_2O_3) in the wear debris at higher temperature would have further lowered the friction. In hind sight CrN may not be the most appropriate phase in the multilayer system. TiN may be an excellent substitute with its high hardness, good adhesion and oxidation resistance.

$$TiN + O_2 \longrightarrow TiO_2 + \frac{1}{2}O_2 \quad \Delta G_{300K} = \text{-554 kJ/mole} \quad (17)$$

Mo_2N will preferentially oxidize in environments of limited oxygen and the absence of the abrasive phase at high temperature would further reduce the friction. The nitrides of W (WN_2) offer an alternative option that is oxidation resistant to temperatures of 800°C. In addition W [15] forms lubricious oxide phases that if present in the debris would not be detrimental but aid in the lubrication mechanism. More ideas on improvement the coatings are included in Chapter 7.

Chapter 5. Industrial validation testing of the CrN/Mo_2N coated drill bits

Self lubricating coatings have been shown to work at high temperatures. This chapter will go over the effort to coat industrial cutting tools, and carry out validation testing in the laboratories at Ford and Boeing. The intent is to demonstrate that the self lubrication coating works in an industrial testing environment. The work described in Chapter 5 was tested in the laboratory scale using a high temperature ball on disk tribometer. The test conditions and environmental are well controlled with the substrate heated up to the pre-set temperature and a 40 mg force applied via a fresh surface of a sapphire ball at each temperature. Industrial drill bits on which our coatings were applied are subject to much higher torque and thrust forces. The (Figure 67) shows the different substrates on which our coating was implemented. The Ford drill bit is a 5/16'' tungsten carbide (WC) drill bit marketed under the "Titex" brand name. The Boeing drill bits are 10 mm high speed steel (HSS).

Figure 67. Image of Ford, Boeing drill bits and M50 substrate used for laboratory scale tests.

The hardness and adhesion were optimized on polished M50, 1'' coupons. The overarching purpose of our validation testing was to gauge how our multilayer films performed in industrial scale drilling tests. The tests were carried out by drilling 20mm holes in compacted graphic iron. The details of the experimental setup are outlined in chapter 2.

5.1 Deposition of Coating.

The conditions of deposition optimized in chapter 5 were largely maintained in our deposition of industrial coatings. The power on the Cr and Mo cathodes were 2.1 kW and 3.5 kW respectively. The bias was maintained at -50V. The sample holder was changed since it was expected to hold drill bits instead of M50 coupons. The drill bits undergo rotation about two axis on the planetary

stage holder. The sample holder was a planetary rotation type stage (Figure 68) in which the drill bits rotate about its length while the whole stage rotates about its centre axis. The deposition was carried out in three batch of different CrN:Mo_2N ratio deposition. The relative amounts of CrN to Mo_2N were maintained in batch 1 and 2 but the thickness of the bilayer period was decreased by increasing the rotation speed of the stage from 1.5 rpm to 5 rpm. This will allow us to understand the effect of bilayer thickness on the test results. The amount of CrN in the multilayer coating was increased in Batch 3 by increasing the power on the Cr cathode from 2.1 kW to 3.5 kW. This decrease in the molybdenum amount relative to Batch 1 and Batch 2 will allow us to study the effects of CrN:Mo_2N ratio on the coating (Table 5).

Table 5. Deposition details of the 3 different batches of industrial coatings (CrN/Mo2N).

	Bi-layer periodicity(nm)	Volume fraction (CrN:Mo_2N)	Thickness	Adhesion Layer(CrN)	Critical load to failure(Lc)
Batch 1	6.6	~ **1:2** (2.1 kW:3.5 kW)	4 µm	~200 nm	4 kgs
Batch 2	2.2	~**1 :2** (2.1 kW :3.5 kW)	4 µm	~200 nm	5 kgs
Batch 3	2.7	**4:5** (3.5 kW:3.5 kW)	4 µm	~200 nm	4.5 kgs

Figure 68. Planetary rotation stage for coating drill bits

5.2 Optimization of bulk properties

5.2.1 Hardness measurement: Hardness studies in chapter 3 and chapter 4 have established that variation of the relative amounts of CrN and Mo_2N does not significantly affect the hardness numbers of the multilayer coating. The hardness of the coating tends to stay within the rule of mixtures (20-30 GPa regime). A hardness measurement via the Rockwell hardness scale on the drill bit shows a hardness increase from 54 Rc to 56 Rc, this indicates that the deposition process did not produce any softening of the drill bits which is a concern in general deposition process.

5.2.2 Adhesion tests: Drill bits are subjected to large stresses and torques forces during drilling. Adhesion of the film is of particular importance because the test block (CGI) is particularly abrasive. Our adhesion tests were carried out on M50 steel, which due to its wear resistance and strength at high temperature is a fairly representative tool substrate. The actual materials of the drill bits were tungsten carbide (WC) and high speed steel (HSS). Table 5 shows the adhesion values of the 3 different batches of coatings. The detailed explanation of adhesion tests and its critical load to failure (in kgs) is included in chapter 2. The adhesion values are in excess of 4 kgf and this is a characteristic of well adhered films. The adhesion layer and the film thickness (4 μm) were optimized to maximize adhesion of all the coatings in the 4-5 kgs regime. A general rule of thumb for critical load for well adhered films is about 1 kg for each micron of thickness[88-90] and the critical force to failure generally has a linear dependence.[91]. The true measure of adhesion is of course, determined by actually testing the drill bit.

5.2.3 Adhesion layer. The purpose of the CrN adhesion layer was to increase adhesion to values in excess of 4 kgs. Coatings were applied with 1) no transition layer 2) 1 μm transition layer and 3) ~200 nm transition layer. The coatings on the test M50 samples were in the 1- 1.5 μm range.

The choice of ~200 nm was arbitrarily chosen to be less than 1 µm. The coating with the intermediate adhesion thickness showed the highest critical load to failure of 4 kgs (Table 6). So a transition layer of ~ 200 nm was selected on all the coatings batches to maximize adhesion. The Figure 69 shows the difference in the scratch channel of the 3 loads. The critical normal force at which first failure of the coating is detected is 4 kgf. The test done using the 5 kgf shown in Figure 69 (c) was above the critical load to failure (Lc) and the acoustic emission was ~80% of the maximum range. The final coatings on the drill bits themselves were 4 µm.

Table 6. Temperature measured on the surface where the drill bit exits when drilling.

	CrN:Mo_2N ratio (Bilayer period)	Surface temperature on break out (°C)
Uncoated	0	946
Coated (batch 1)	1:2 (~7 nm)	631
Coated (batch 2)	1:2 (2.2 nm)	753
Coated (batch 3)	4:5 (2.7 nm)	669

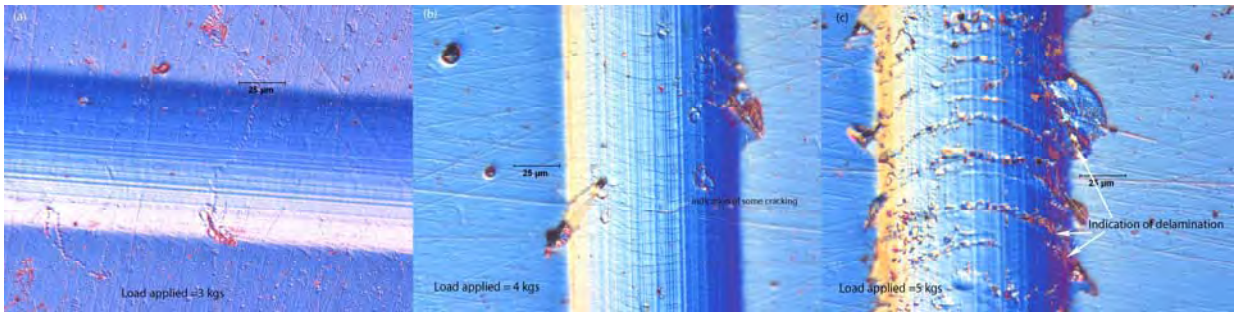

Figure 69. Comparison of the scratch track at (a) 3 kgs (b) 4 kgs (c) 5 kgs

5.3 Results

5.3.1 Ford Testing (WC-Titex): Torque and thrust measurements

Our tests were carried out by drilling on CGI and the temperature was monitored by a thermal imaging camera. The help of John Pawelec, lab technician at Ford Motor Company, Livonia, was critical to the success of these experiments and his help is acknowledged here. Torque and thrust were measured by using a dynamometer that measure torque and thrust. The torque that will be

applied in our tests are set in the CNC lathe and the machine works to maintain a steady torque value. The thrust typically compensates for an appropriate rise or fall in torque values. This means that in case of increase surface resistance to the drill bit (e.g. metal adhesion) the lathe compensates by providing a thrust increase to aid in easier cutting. Lower torque and thrust values for the same geometry of the drill bit and similar work piece indicates a smoother more energy efficient cut. Lower torque/thrust values can be correlated with longer tool life. Figure 70 shows that the torque of the coated drill bit is lower than the uncoated drill bit at all speeds. There is an expected rise in torque of the coated and the uncoated drill with wear. Similarly the thrust values of coated drill bits are lower than the uncoated drill bit as shown in Figure 71. The increase in thrust values with increasing number of holes is an expected behaviour given degradation of the drill bit with increasing use. The last histogram plotted at the 9^{th} hole is done at 100 mm/min. This is the speed at which the first hole was drilled and this comparison between (1,100) and (9,100) serves to highlight the degradation of the drill bit. The uncoated drill bit shows much more adhesion of CGI on the surface when compared to the coated drill bit. The uncoated drill bit shows more damage to the drill tip (Figure 72). The drill tip is the first surface of the drill that touches the work piece and hence maintaining sharpness of the drill tip is important to keeping low torque and thrust values. Figure 72 (a) shows the increased damage to the drill tip compared to the relatively coated tip that shows little or no metal adhesion (Figure 72 (b)).

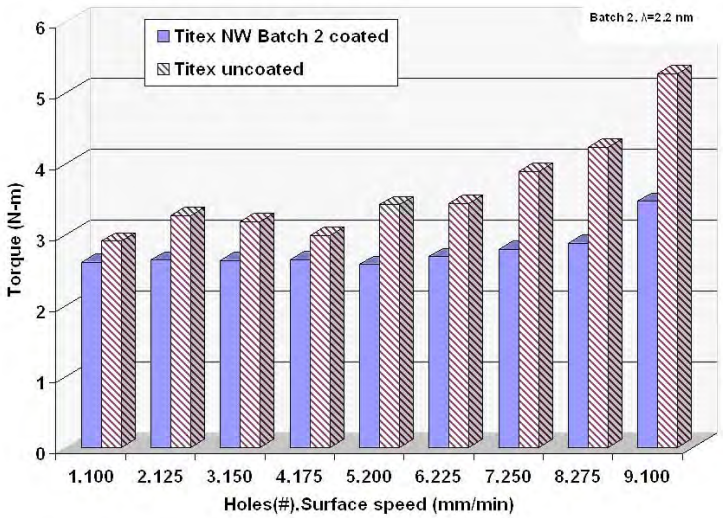

Figure 70. Torque of a coated drill bit and an uncoated drill bit measured as a function of number of holes drilled at a certain surface speed.

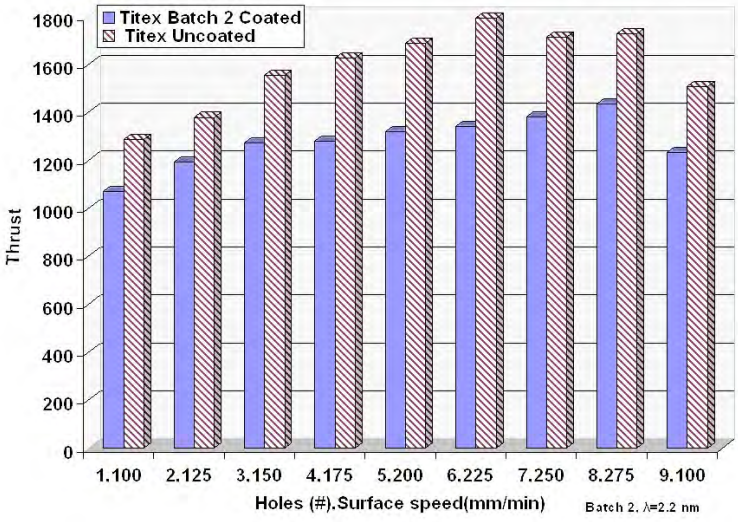

Figure 71. Thrust of a coated and an uncoated drill bit measured as a function of number of holes drilled at a certain surface speed.

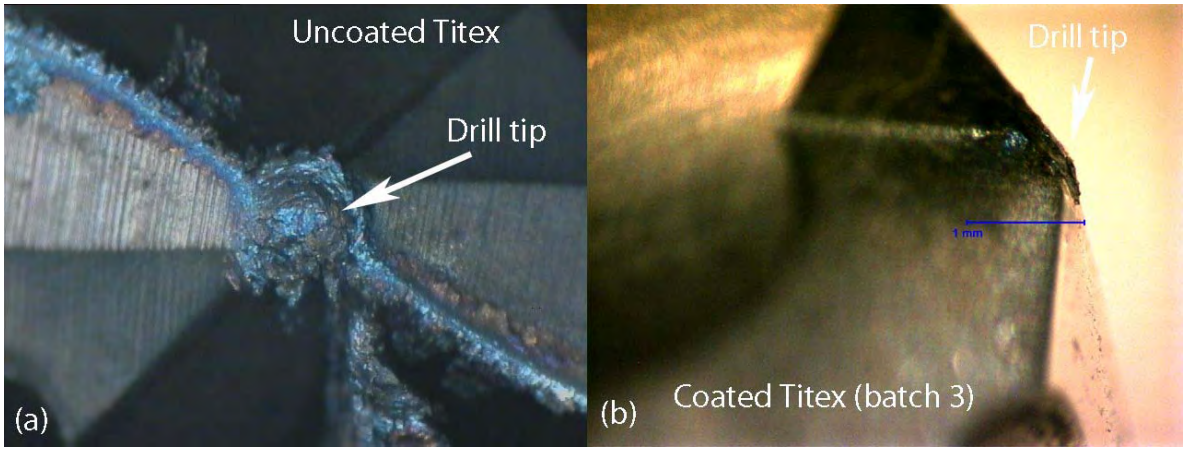

Figure 72. Coated vs. Uncoated drill Titex drill bit tested at Ford

A consistent concern in our test was our inability to reach high enough temperatures (> 400°C) to initiate self lubrication. At the maximum spindle surface speeds we were still unable to operate in temperatures in excess of 300°C (Figure 73). The CGI block and the metallic chuck constituted a large heat sink that was part of the reason why the drill bit failed to operating in the high temperature regime. (> 500°C). Time of cut was another critical component that we explored. Doubling our time off cut by doubling the thickness of the work piece did not show any significant rise in temperature and general remained in the <300°C regime.

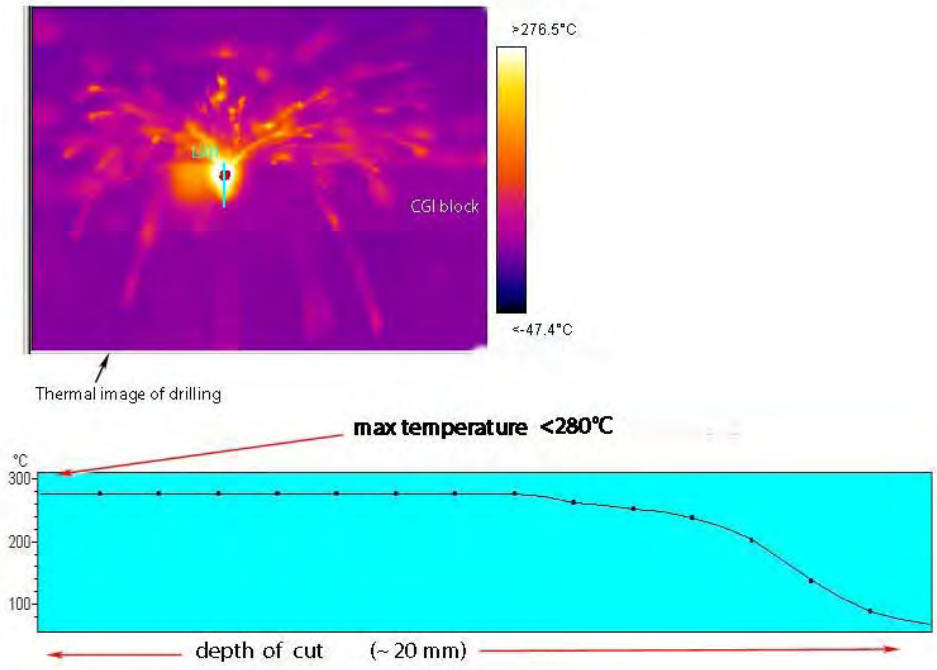

Figure 73. Thermal image of the drill bit in the CGI block with temperature profile into the block plotted.

Adhesion on the drill bit: SEM images of the drill bit after testing shows low amounts of adhesion of CGI on the coating. The Figure 74 (a) shows a cross section image of the drill bit while Figure 74 (b) shows a lower resolution image of the coating with some areas where coating of delamination. This drill bit in particular was drilled till failure to compare with commercially available coatings SEM images reveal porosity in the WC coatings which could adversely affect coating adhesion. This could have lead to coating delamination at high stresses areas of the drill bit

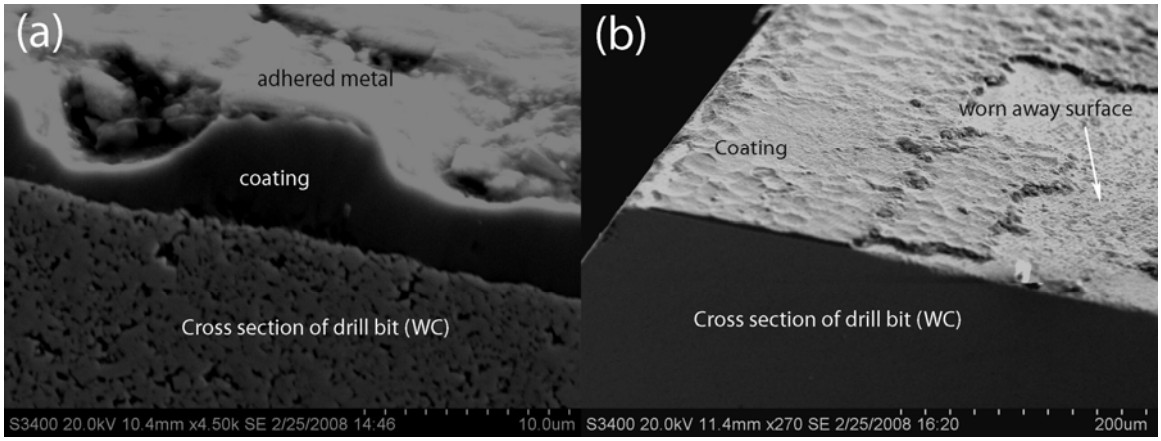

Figure 74. SEM image of the cross section of WC coated surface after validation testing on CGI blocks.

5.3.2 Tests in the presence of nitrogen

Our prior tests have shown a marked reduction in friction at elevated temperatures in the presence of nitrogen. These friction results were ~25-30% lower than their tests in air.

The testing rig at the Ford laboratory allowed us to flush the cutting surface with nitrogen via the lubricant bore (Figure 75) . Our test results did not show any marked effect due to the addition of nitrogen. In general coated drill bits showed lower torque and thrust values than uncoated drill bits with increasing usage.

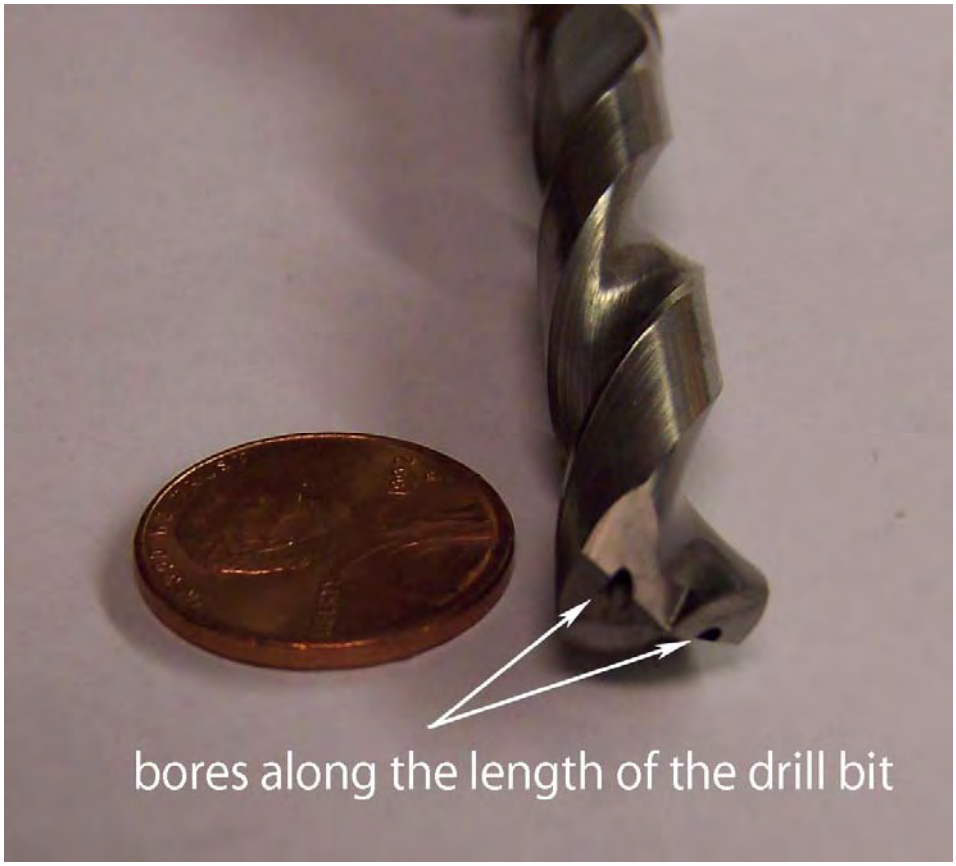

Figure 75. Image of the drill bit showing the lubricant bore for N2.

5.4. Boeing Test on HSS

Validations testing via drilling of our coated drill bits were carried out in the Boeing laboratory. The help of James Castle, a PhD student at Washington University and a part time employee of Boeing, is acknowledged. Drilling of the 0.3125'' holes was done on Ti6Al4V alloy blocks and the temperature of the surface as the drill bit exits was measured. (Table 6) shows the exit surface of the uncoated and coated drill bits. It is important to note that the exit temperature in the uncoated drill bit is ~250- 300°C higher than the coated drill bit. The uncoated drill bit shows high exit temperatures of 946°C while the coated drill bits are in a relatively lower temperature range of 630-750°C. In general, the close up of the drill bits show that the coated and uncoated drill bits showed metal adhesion leading to a built up edge (BUE). BUE refers to the unwanted rough edge on a cutting tool that is created by workpiece binding or welding on the tool during cutting. In these tests the uncoated drill bit in particular shows severe titanium built up edge.

Although the surface temperatures were in the 600°C range our test failed to demonstrate self lubrication at high temperature. Any drop in torque or thrust values at high temperatures were masked in the noise of the dynamometer. It is believed that adhesion of metal on the coating severely impeded our lubrication tests and our ability to test for high temperature lubrication. Figure 76 (a) shows a cross section image of the drill bit before drilling, while Figure 76 (b) shows the uncoated drill bit after drilling. Not the extreme build up edge of the uncoated drill bit. In short the tests at Boeing indicated that we must have a coating that eliminates work piece adhesion, if we expect the self lubrication mechanism to be active.

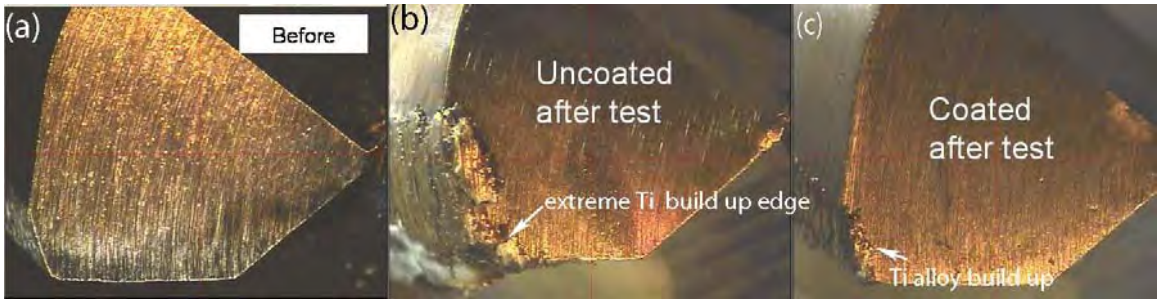

Figure 76. cross sectioned Boeing drill bits showing build up edges of the drill bits (a) Before use (b) Uncoated after drilling (c) Coated after drilling.

Although the amount of built up Ti alloy on the cutting edge of the coated sample is significantly less than the uncoated alloy. The Ti adhesion on the cutting tool prevents our native coating surface from coming in contact with the work piece, thus the measured torque and thrust values are likely due to the Ti on Ti contact.

5.5 Conclusions and future work

The deposition conditions and bulk properties were optimized to suit the geometry of the drill bits. Three batches of CrN/Mo_2N multilayer coatings, were deposited with varying bi-layer periodicity and different relative ratios of CrN:Mo_2N . The coatings had critical load to failure values of 4 kgs and above in scratch adhesion tests. The coatings were 4 µm thick with an interfacial adhesion layer of CrN (~200 nm). Tests at both Ford and Boeing showed that the coatings were largely well adhered and were intact during the test. They exhibited lower torque and thrust values than uncoated drill bits. We were unable to demonstrate self lubrication at high temperature due to low drilling temperatures at Ford and metal adhesion issues at Boeing. Commercially available coated Titex drills performed at an average ~40% lower torque and thrust values when compared to the CrN/Mo_2N drill bits. This was expected given the self lubrication at high temperature and the associated lowering of friction failed to activate. The damage to the drill tip in the Titex coated drill bits and CrN/Mo_2N coated drill were comparable

in the tests performed. So as a hard coating its resistance to wear was comparable to commercially coated available Titex drill bits.

To improve on the properties of these coatings there are other aspects onto which attention must be focused. The choice of the drill bit material has a very important role to play in improving coating adhesion and overall coating performance. The WC drill bits exhibit porosity in bulk and it is likely that the porosity could adversely affect coating adhesion. For future work it will be appropriate to systematically study the effects of WC's bulk porosity on coating performance. The WC drill bits are made (by manufacturer) via the powder metallurgy route, which accounts for its porosity. Since our coatings have performed well as hard coating, the extra hard WC substrate could be unnecessary and could even be replaced with a HSS drill bit.

Surface analysis of some of the coated HSS drill bits show that parts of the coating on the drill bit exhibited low angle columnar growth morphology or atomic shadowing effects[92]. Such low angle growth areas are typically not fully densified [93] and leads to coatings of inferior properties [94]. Increasing the bias during deposition and hence enhancing atomic mobility on the coating surface during growth should easily prevent this problem.

CrN has significantly reduced performance due to BUE formation. This is further aggravated by the high temperatures we operate in. To reduce BUE formation in machining it is importance to look for substitute to the CrN layer. Even additives to the CrN like Al and Si that can reduce BUE are worth looking into. TiN or TiAlN could serve as a feasible substitute to the CrN layer. TiB_2 with its low surface friction and speeds chip flow in cutting could be a viable alternative if incorporated into our multilayer system in place of CrN [95, 96]. In any material selection process the performance of the coating is dictated by a range of performance variables and so

just optimizing for a minimal built up edge formation will not suffice. Hence the compatibility of these alternatives with the Mo_2N layer and its performance in a multilayer arrangement has to be investigated.

Chapter 6. Deposition and characterization of co-sputtered BN-Mo_2N

6.1 Introduction

Self-lubrication at high temperature as a concept was proved and shows considerable promise. The tests at high temperature show that in the Mo_2N/CrN system, the lubrication mechanism activates at ~500°C. Validation tests have shown that we failed to reach temperatures high enough to initiate self-lubrication. The temperature remained below 300°C even in machining operations on a highly abrasive alloy. A coating in which lubrication initiates below 300°C would be an excellent working alternative. Better still, incorporating an element that forms lubricious oxides at temperatures below 300°C would broaden the temperature response window and serve to fit a wider range of machining applications. The basic idea is to incorporating an oxide forming element into the coating to achieve a low friction phase through an auto-initiated response at relatively lower temperature. In effect we propose to use the materials in a nano-layered structure that will be hard, tough, adherent, and lubricious at a broader range of service temperature. In the following work, the intent is to build on the current work and investigate ways to broaden the temperature response widow of self-lubricating coating, while still retaining our proven twin system of Mo_2N/CrN.

6.1.1 Material selection criteria

Our effort is to choose an appropriate material that could be suitably co-sputtered with our working Mo_2N/CrN system and yet form an oxide at lower temperature and help in widening the temperature response window for our self-lubricating films. It is important to have oxides of metals or transition metals that exhibit low friction at high temperature. Among our choices are Re, Zn, V, Ti ,W and B [15]. B_2O_3 is a particularly low friction phase when it forms its glassy

phase at high temperature [97, 98]. Compounds of boron including its nitrides and carbides[99] when oxidized in the presence of oxygen can form a low friction phase at lower temperatures too. This wide temperature spread in lubrication behaviour makes boron a favorable element to incorporate in our material system.

6.1.2 Boron as the material of choice

Hexagonal Boron nitride can be an excellent candidate to incorporate into our coatings due to a range of favorable properties. Boron nitride forms a B_2O_3 high temperature lubricious oxide. The predominant nitride phase of B that is deposited in magnetron sputtering is the h-BN which is a somewhat lubricious material, similar to MoS_2 and graphite, but due to its ionic character it exhibits a relatively higher friction coefficient than MoS_2 and graphite. The self lubrication of h-BN is explained in terms of its sliding on its low-index crystal planes [100-102]. Under dry lubrication h-BN shows friction coefficients of ~0.2 and transfer films have been characterized be lamellar with oriented (002) planes [103]. Boron nitrides readily form boric acid on oxidation. So our challenge is to incorporate boron into our material system and make it readily available for oxidation at the right conditions [99, 104]. It is relatively soft compared to the nitride matrix and its effect on coating strength will also be explored as a function of its dispersion/size. Boron nitrides in general have many desirable qualities including their non-reactivity with ferrous materials and their ready ability to be deposited in thin films make them most suited for our tooling applications. While c-BN is extremely hard (second only to diamond), this phase has proven to be difficult to form by magnetron sputtering, and is not likely to be formed in our study.

The oxidation rates of BN is strongly orientation dependant and water vapour sensitive [105]. In the absence of water vapour B_2O_3, the oxidation product of BN forms a glassy phase at high temperature characterized by its high adhesion to the sample and low viscosity in its liquid state[106], this aids in its performance as a low friction phase. Boron and its compounds have an alternative mechanism of producing a low friction phase at lower temperatures.B_2O_3 even at room temperature reacts spontaneously with water molecules to from H_3BO_3 film on the surface[98]. This reaction is favoured since the standard heat of formation producing the H_3BO_3 film is negative [62, 99, 107]. The boric acid has a layered structure and when present on the sliding surface the atomic planes align themselves parallel to the direction of motion and slip along their easy shear planes. In the case of H_3BO_3 films, the slip happens along the weakly bonded (Van Der Waals forces) planes (Figure 77). In plane the boron is strongly bonded to oxygen and hydrogen. Since our coatings are deposited via reactive sputtering, we start with metal targets and introduce nitrogen in controlled amounts to form the desired nitrides.

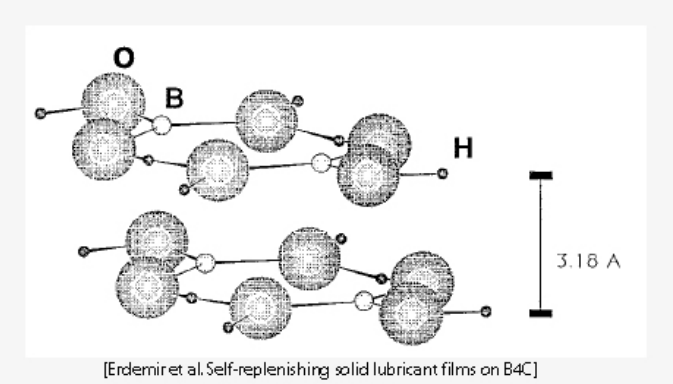

Figure 77. Layered structure of H_3BO_3

The boron nitride is to be dispersed in the solid form in one of the metal nitrides. The possibility of forming a metal boride exists, since typically the borides are harder and more stable than the

nitrides. From the standard heats of formation, it appears that we will have more success forming BN in the Mo_2N lattice than in the CrN lattice, since the energy balance favors forming BN over the Mo_2B[11]. The goal of this work is to deposit, characterize and study the behavior of the as-deposited BN-Mo_2N films and to understand their behavior on annealing. A schematic of the phase distribution scheme developed in chapter 4 is shown in Figure 78 (a). Figure 78 (b) shows the current scheme in which a composite phase of BN and Mo_2N will be deposited to study its properties.

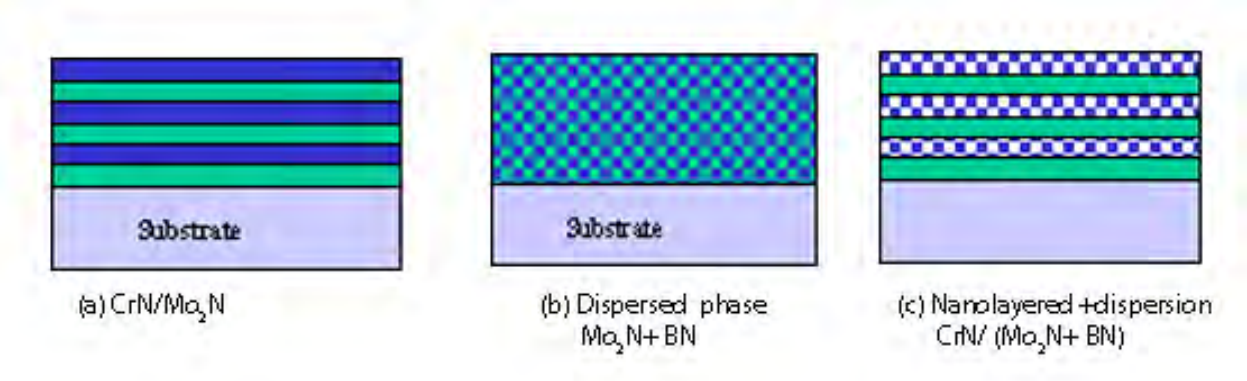

Figure 78. Different nanostructured deposition schemes researched. (a) CrN/Mo2N multilayers (b) composite Mo2N+BN(C) (c)CrN/Mo2N+BN(C) multilayers.

The eventual goal was to deposit this BN-Mo_2N (composite) material with CrN as a multilayer and optimize its bulk properties as shown in Figure 78 (c). The idea is to eventually end up with a self lubricating coating without any compromise in bulk properties. It is proposed to use materials in a nano-layered structure that will be hard, tough, adherent, and lubricious at the service temperature.

6.1.3 Deposition parameters and experimental details

Prior work with the Mo_2N/CrN had established optimum deposition parameters for both Cr and Mo. The current work will build on this work and since it is critical that we form the same phases

of Cr and Mo, the partial pressure and bias conditions are maintained at the levels used for the CrN/Mo_2N deposition. The baseline parameters of deposition are: 1.5 mTorr of N_2, -50 V bias and 5.5kW power, unless explicitly stated. The thin film deposition to study the separation of the phases was carried out on salt (~50nm) and the salt was dissolved away and the film as scooped up onto a TEM grid. The TGA studies were carried out in air and the mass gain is tracked only in the forward cycle, where the rate of heating from room temperature was 5°C/min and finally held at 900°C for 15 minutes. TEM characterization was carried out on a JEOL 2100 microscope.

6.2 Deposition and phase segregation studies on NaCl crystal

Composite coatings that are TEM transparent (~50nm) were deposited on freshly cleaved salt crystals. The intent is to specifically study how the BN and Mo_2N segregate in the reactive sputtering process The sample preparation routine is depicted in the Figure 79.

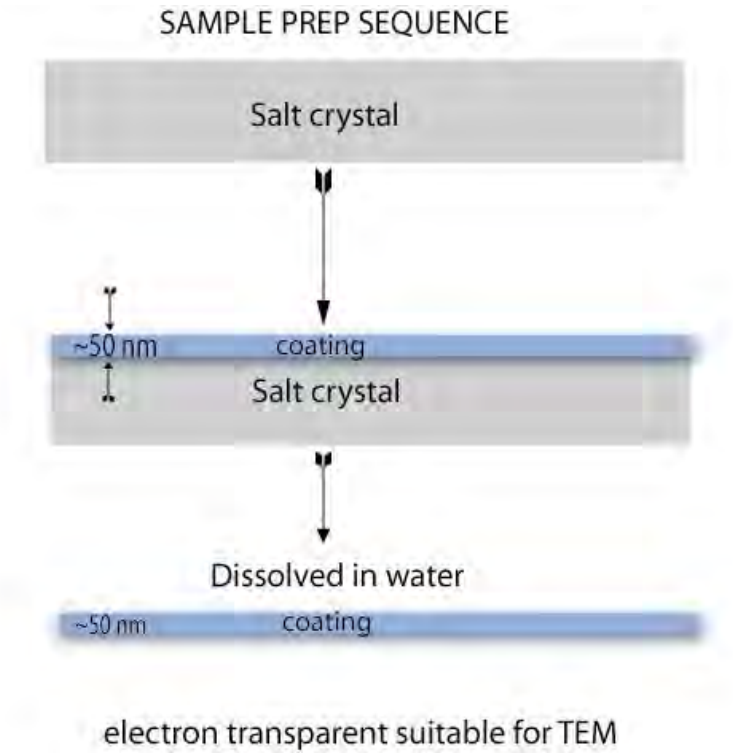

Figure 79. Steps involved in preparing TEM samples of BN-Mo_2N composites deposited on salt to study their phase contrast.

Our deposition studies show that the two phases of BN and Mo_2N have a clear demarcation in contrast, which is visible in the bright field mode of the TEM image in Figure 80. The phase contrast originates from the atomic number (Z) contrast of the BN and Mo_2N. It is interesting to note that there are two different length scales of segregation. A ~10nm wide, largely two dimensional phase segregation, where the lighter region of Mo rich region is clearly apparent. The figure also shows regions where both Mo rich and B rich phases of about ~2 nm seems to be present. The fact that BN seems to separate out as ~2 nm wide regions seem to indicate that the BN does not coarsen under our deposition conditions. The deposition temperatures(~100°C) and bias (-50 V) conditions are low and due to insufficient energy the diffusion rates on the substrate are too low to favour agglomeration, at least under the condition of our deposition.

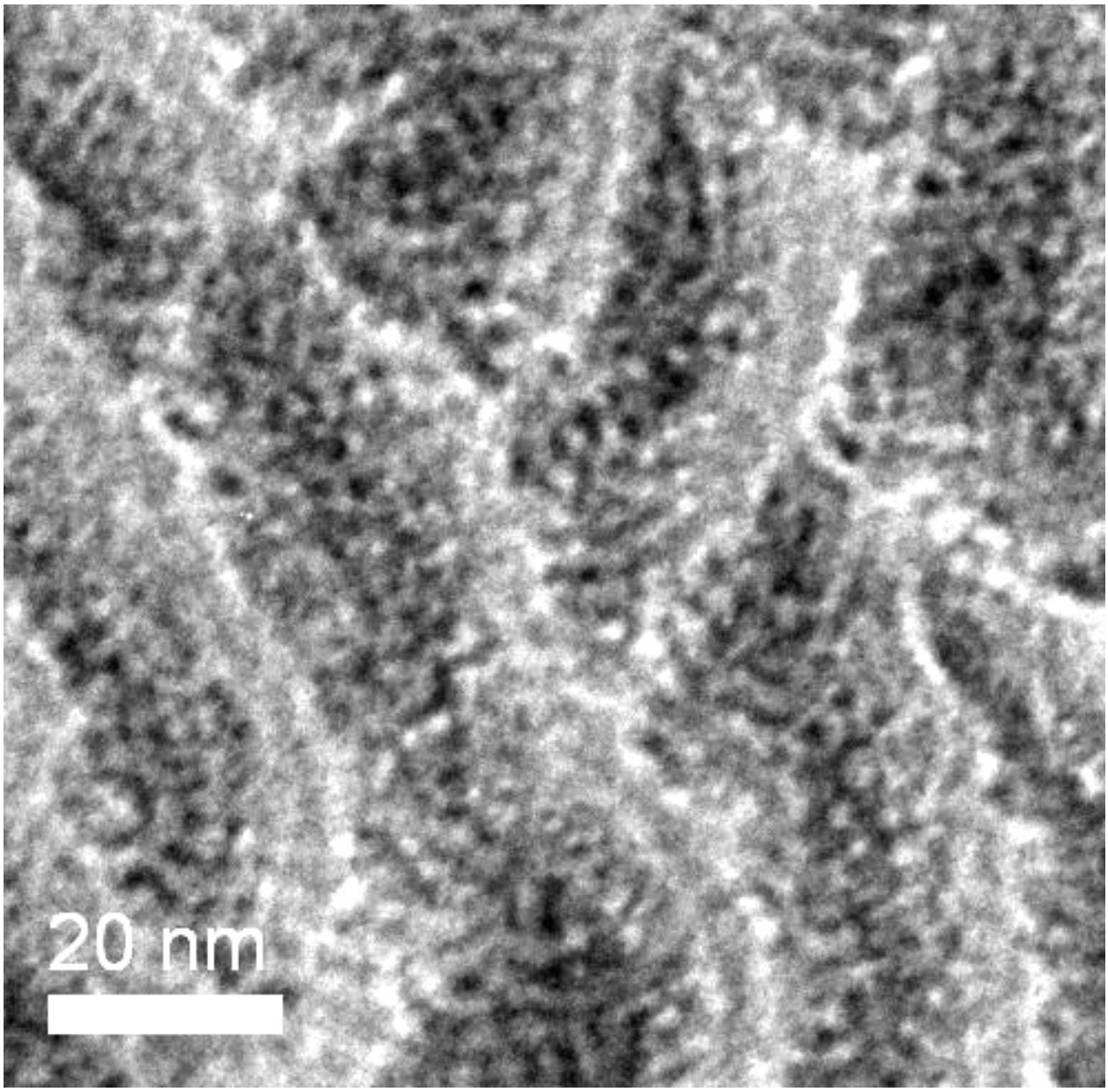

Figure 80. TEM image in image mode of reactively sputtered BN-Mo2N films at 50 bias (5.5kW, 1.5mTorr N2).

6.3 Deposition rate, compressive stress and TGA studies on co-deposited samples

6.3.1 Deposition rate and compressive stress as a function of partial pressure

The deposition rates and residual stress of the BN-Mo_2N composite is studied as a function of partial pressure, power and bias. The target used for our composite reactive sputtering is shown in Figure 81. The arrangement is an alternating sequence of pure Mo (99.99%) and B_4C. Studies on the sputtering rates of BN have established the sputtering rates of BN to be in the 17.5-20.0 nm/min range. Deposition rates of Mo is around four times higher than B_4C at -50V bias and so significantly more Mo_2N is expected in the composite coating. Rough calculations were done to calculate the exact composition of the film on deposition. Working with relative sputter rates (Mo_2N:B_4C::6:1) and race track lengths we determine that 90% Mo phase and 10% of Boron phase were formed. The Figure 82 shows that the co-sputtered BN-Mo_2N composite has a higher deposition rate at low partial pressure. This is classic reactive sputtered behaviour given poisoning and nitride formation of the cathode with increasing partial pressure [56]. It is important to track residual stresses of the films since film adhesion is directly influenced by residual stresses. It is important to note that the residual stress data presented below is calculated from just a single coated sample in each case. The residual stress plots are more a pointer to the general stress regime of the coating (refer Chapter 2). The residual stress is very low (below -0.6GPa) and is not limited to any particular phase or deposition condition. Since the residual stress show no large differences, making any claims that the changes in residual stress are due to changes in deposition conditions would be erroneous.

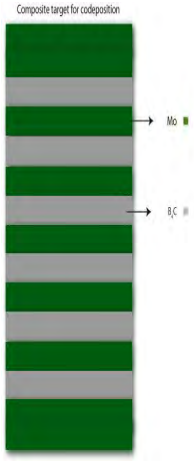

Figure 81. Composite target for co-deposition of BN-Mo_2N

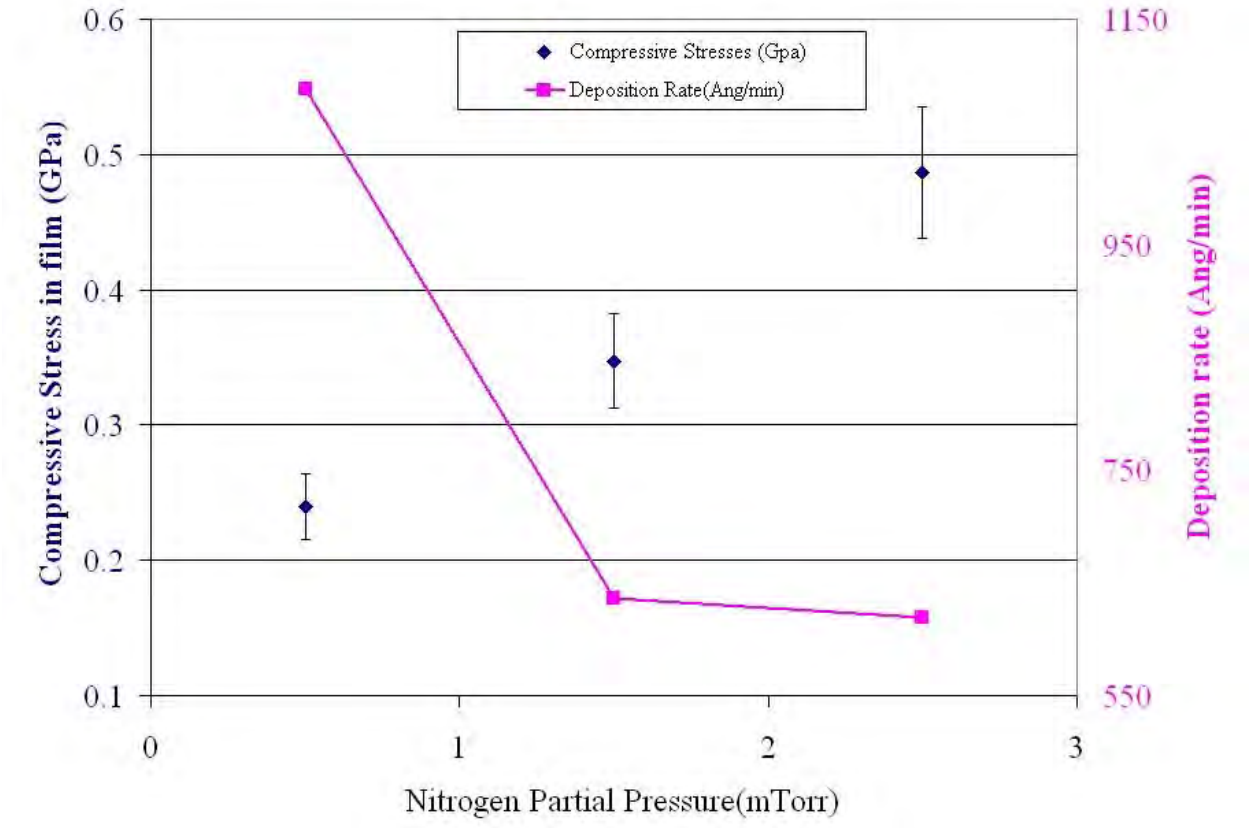

Figure 82. Residual stresses and deposition rates are tracked as a function of partial pressure of N2.

6.3.2 Deposition rate and compressive stress as a function of target power

Figure 83 shows classic deposition rate increase with target power which is the expected behavior with power. In general it is important to note that the residual compressive stress is below -0.6 GPa.

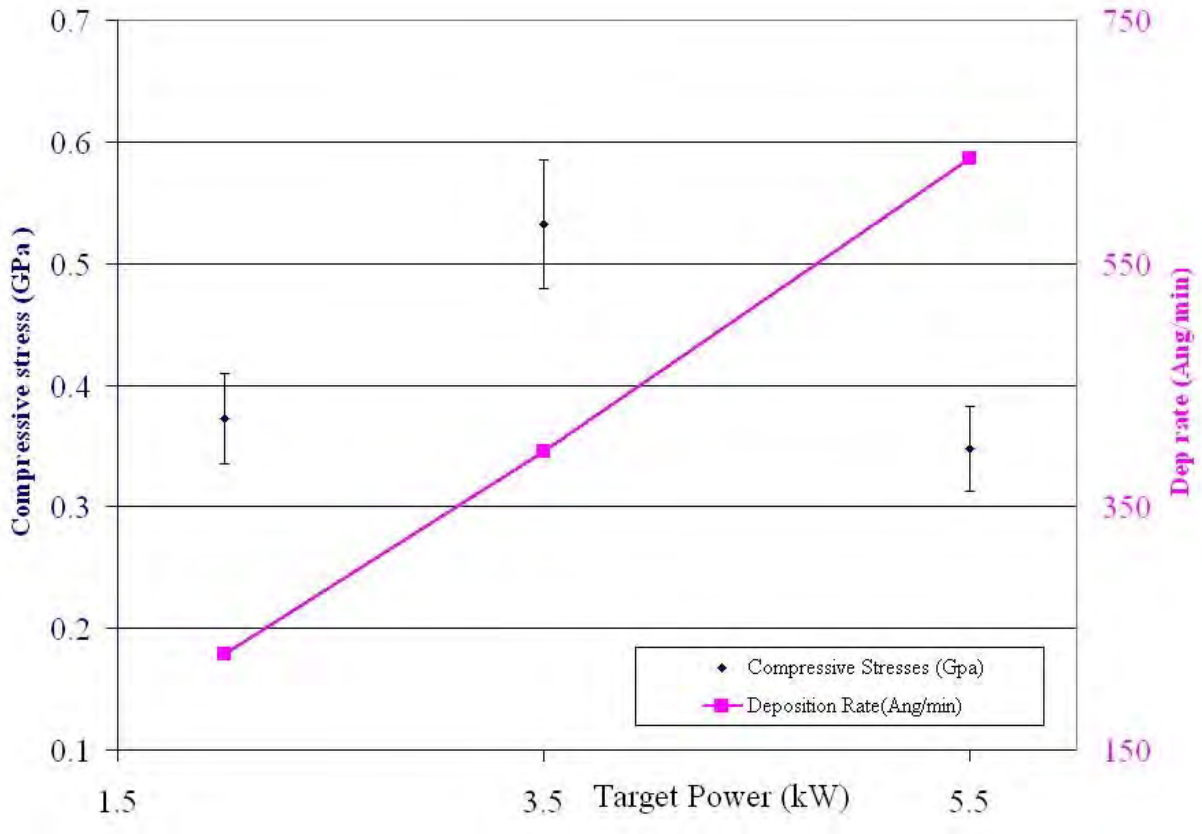

Figure 83. Residual stresses and deposition rates are tracked as a function of power.

6.3.3 Deposition rate and compressive stress as a function of target bias

Figure 84 shows that with increasing bias the deposition rate show a steep decrease. This is consistent with reported studies in which the deposition rates of boron nitride are extremely sensitive to deposition bias[108]. B has a low atomic mass (11) and it easily undergoes ballistic resputtering from Argon (40). Increasing bias on the substrate increases the kinetic energy of the

incoming charged species and this leads to further resputtering. The TEM images show a BN crystal formed by reactively sputtering B_4C in nitrogen at -50V bias. The lattice planes visible in the bright field image correspond to the h-BN. Its polycrystalline behavior is apparent from the random orientation of crystallites h-BN films at -50V bias (Figure 85). The dark field image, formed from a diffracted beam, shows how some of the crystallites are bright since they diffract along the imaging direction while others are dark since they do not diffract along the imaging direction. The final intent is to deposit BN in the Mo_2N layer of the CrN/Mo_2N coating, so it is likely that we will deposit BN as the h-BN phase. A detailed study is included in the following sections. The residual stress is below 1.2 GPa and the rise in residual stress with bias is expected given increase in bias.

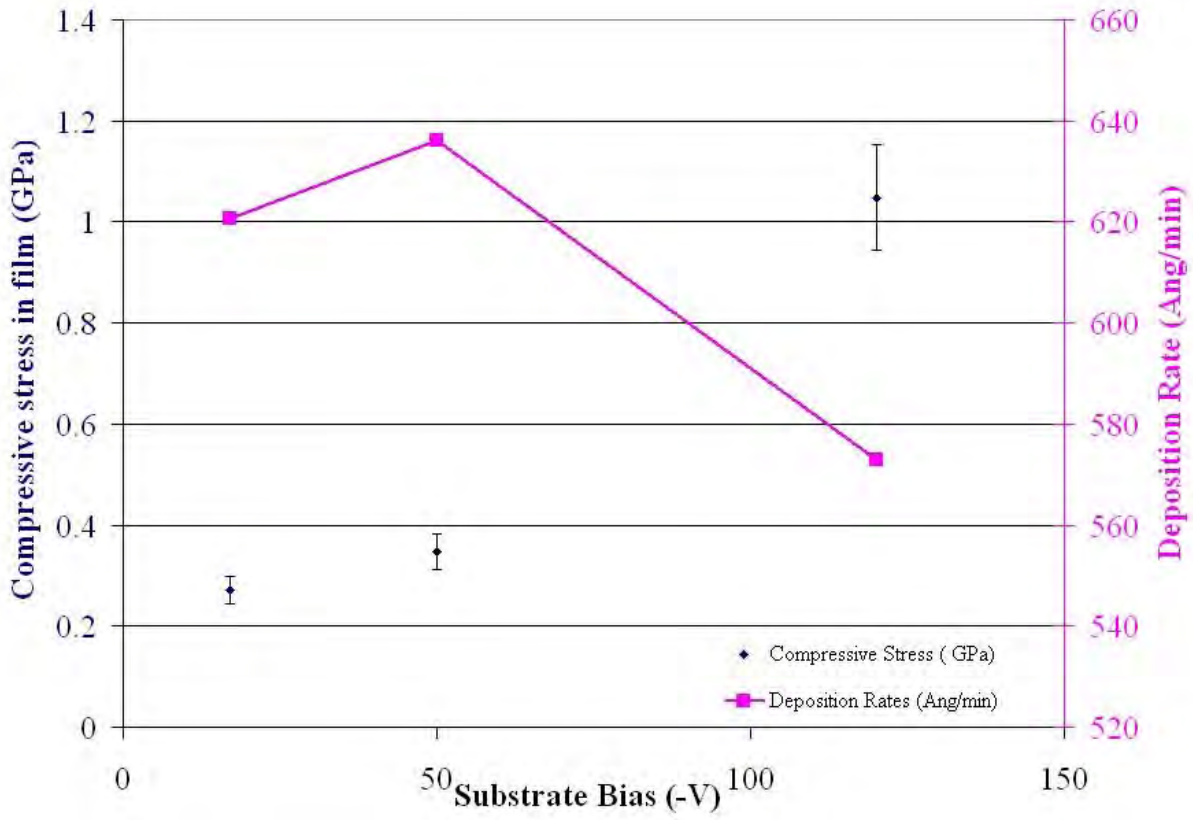

Figure 84. Residual stresses and deposition rates are tracked as a function of bias.

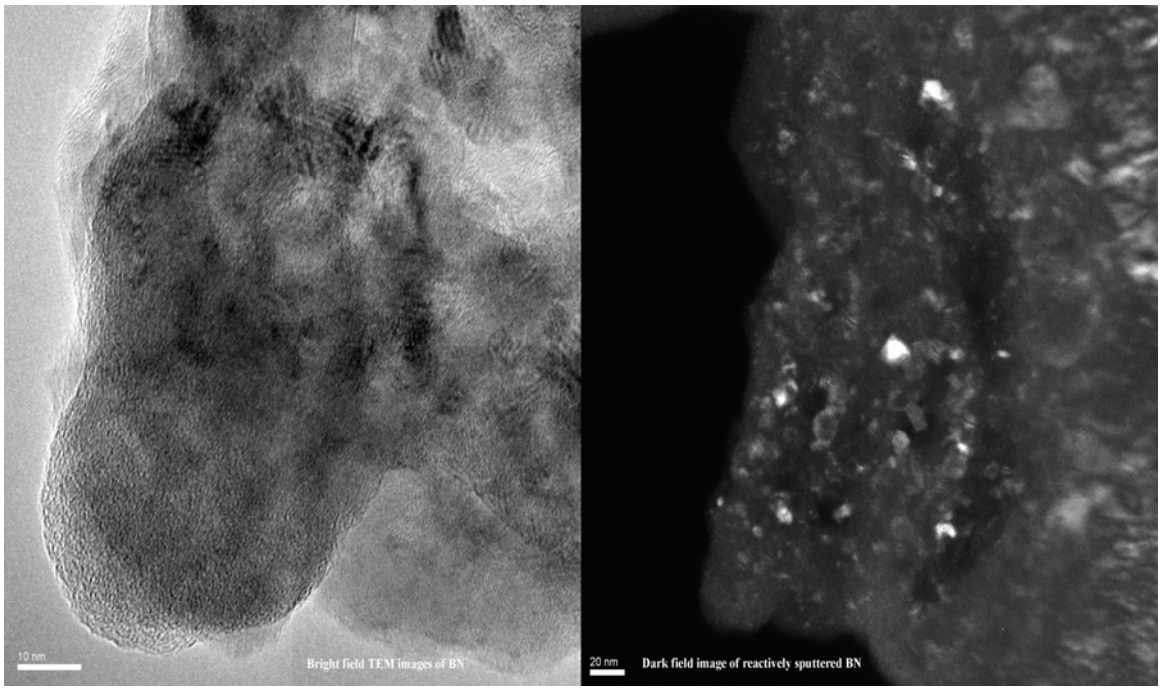

Figure 85. TEM images in bright field and dark field mode of reactively sputtered BN from B_4C cathodes.

6.4 Thermo-Gravimetric studies (TGA) on the BN, BN-Mo_2N coatings

Weight loss or gains are generally disruptive processes to coatings and thermal gravimetric analysis is a simple analytical technique that measures the weight loss and weight gain as a function of temperature. Getting a better picture of the magnitude and temperature ranges of any disruptive effects on the coating due to temperature will allow us to design better coatings. It is important to note here that the films are deposited on Si wafers and the mass gain of the Si substrate is substantial as shown in Figure 86. The Figure 87 has been corrected for Si mass gain. The control Si wafer and the Si wafers on which the compounds and the composite are coated are not always the same thickness. This means that a thinner wafer of equal mass will show larger mass gain with temperature than a thicker Si wafer of equal mass (exposed surface area differences). Hence a sharp rises or loss in mass can be attributed to the coating while small mass gain or loss trends could be attributed to substrate effects.

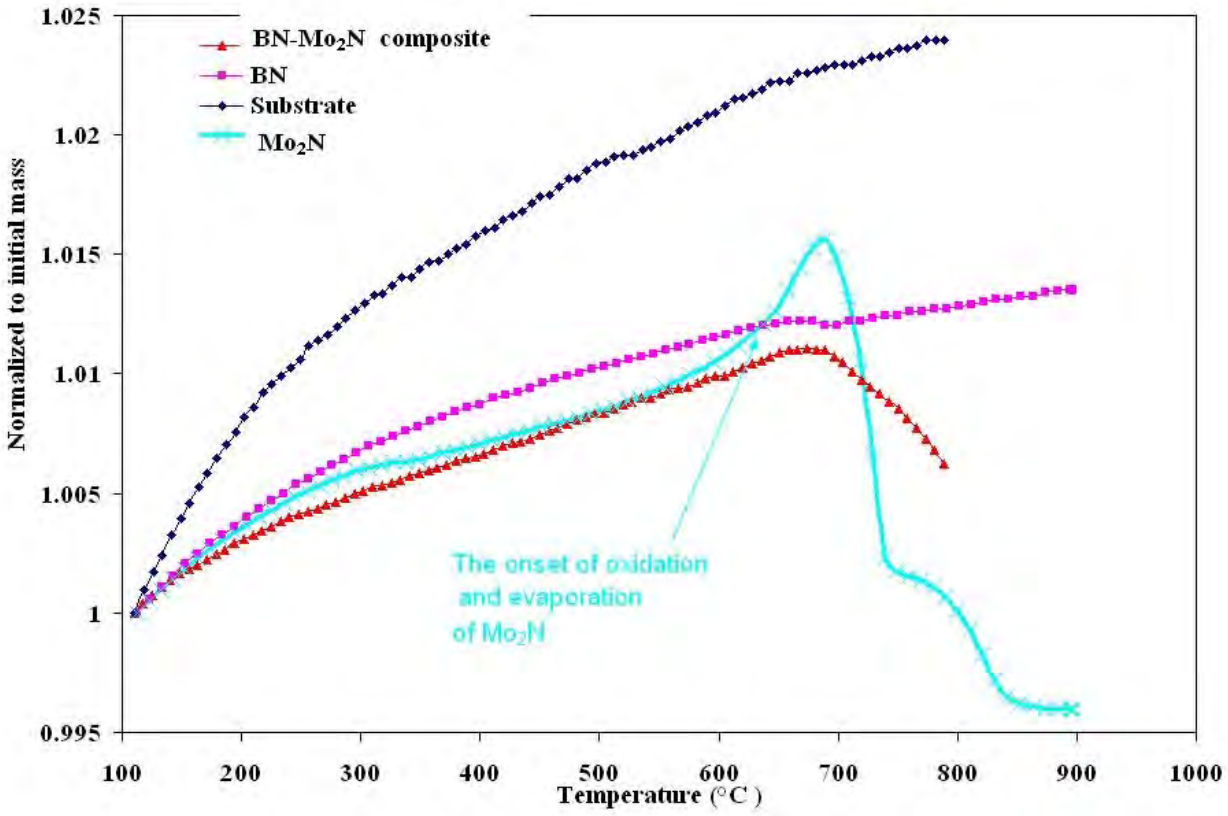

Figure 86. TGA studies on cosputtered BN-Mo_2N phase and BN phase (not corrected for Si substrate weight gain).

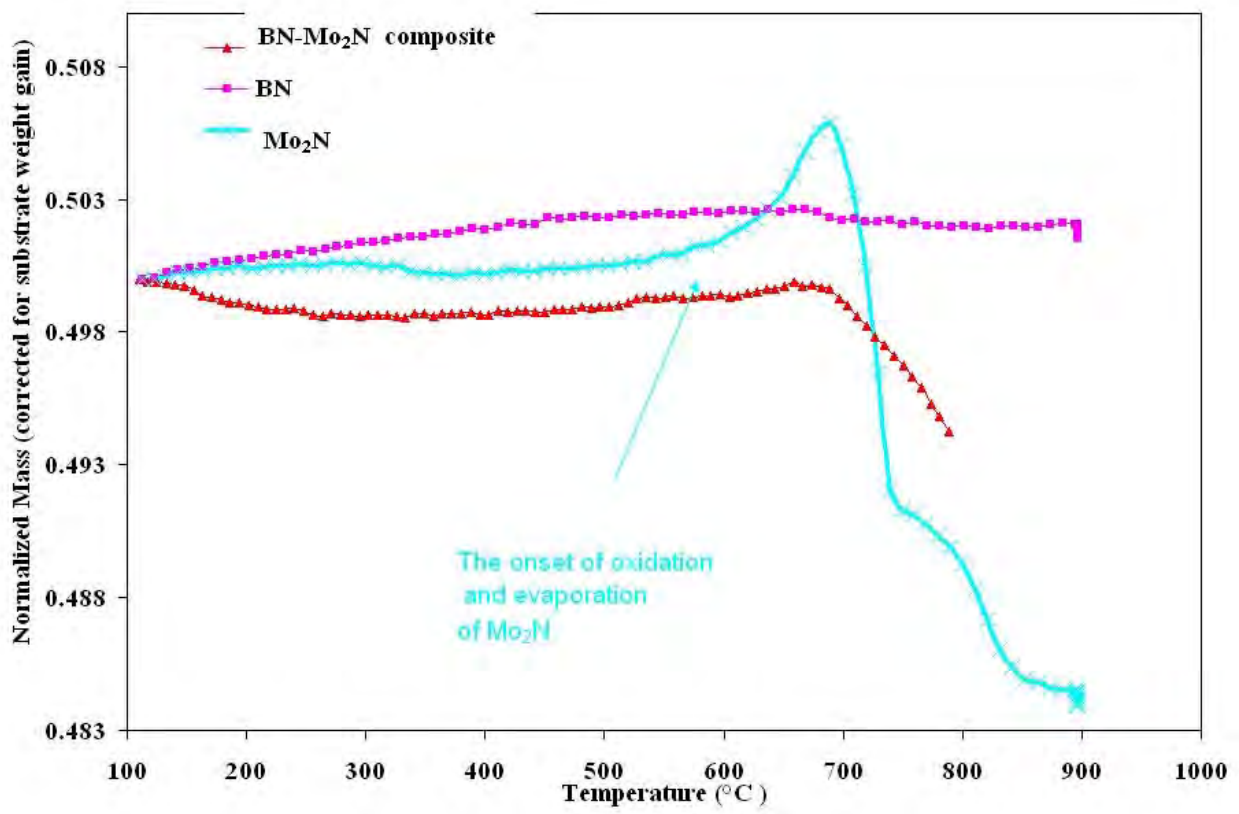

Figure 87. TGA studies on cosputtered BN-Mo2N phase and BN phase (corrected for the Si substrate weight gain).

These TGA studies will help us better understand how temperature affects the BN and the BN-Mo_2N composite. BN films show a steady mass gain with temperature as the BN oxidizes (Figure 86) this is consistent with reported literature [109]. B_2O_3 (equation 15) the primary product of oxidation[110] is known to be highly sensitive to moisture in the atmosphere but given that we operate in temperatures in excess of 500°C we find little or no mass drop associated with a moisture related loss of mass. Mo_2N shows a large mass gain due to oxidation above 500°C and large mass loss above 700°C, this is consistent with the temperatures of formation and evaporation of the oxides of Mo[111].

$$2BN + \frac{3}{2}O_2 = B_2O_3 + N_2 \qquad \Delta H_{298} = \text{-182 kcal/mole} \quad (15)$$

6.5 Hardness and annealing studies on BN-Mo_2N composites deposited at different bias

In this first part of this section, effects on bulk properties due to annealing are presented. The samples were deposited keeping partial pressure (1.5 mTorr) and target power constant (5.5 kW) and bias was changed to study its affects. Recrystallization and grain growth is expected to play a big role in changing the bulk properties of our coating on annealing. In nanostructured materials, large amounts of interfacial energy are stored in the grain and phase boundaries. This can reach ~70% of the volume for grain sizes of ~2-3 nm [112]. This stored energy is a huge driving force to force recrystallization and subsequent grain growth even at relatively low temperatures [113]. An important fact to note is that at 0 applied bias power the substrate is still exposed to -17V (plasma potential).

6.6 Annealing effects on sample prepared at -17V bias

The co-sputtered films at all deposition bias voltages show a significant improvement in hardness on annealing (Figure 88). The hardness rose from 4.81 GPa to 21.34 GPa, this is ~340% rise in hardness. The low bias and the presence of boron together play a significant part hardness of the as deposited film. BN is known to affect the crystallinity of the predominant phase[114] in which it is deposited and this seems to influence the coating crystallinity. TEM images confirm that at lower bias, lower deposition energetic, the Mo_2N lacks crystallinity. XRD images show no significant peaks from either phase. Neither, the as-deposited sample nor the annealed samples deposited at -17V bias, show any obvious features from phase separation. On annealing the -17V deposited sample the intensity contrast that originates from phase separation is more predominant in Figure 89. The difference in the phase contrast due to recrystallization

and growth is clearly apparent in the side by side comparison in the plan view TEM of the coating shown in Figure 89.

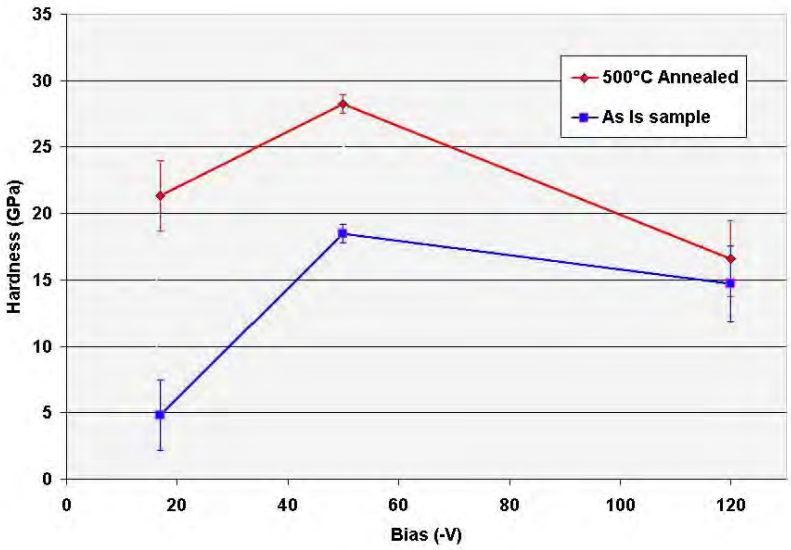

Figure 88. Hardness vs bias of a codeposited and annealed samples of BN-Mo2N (500°C).

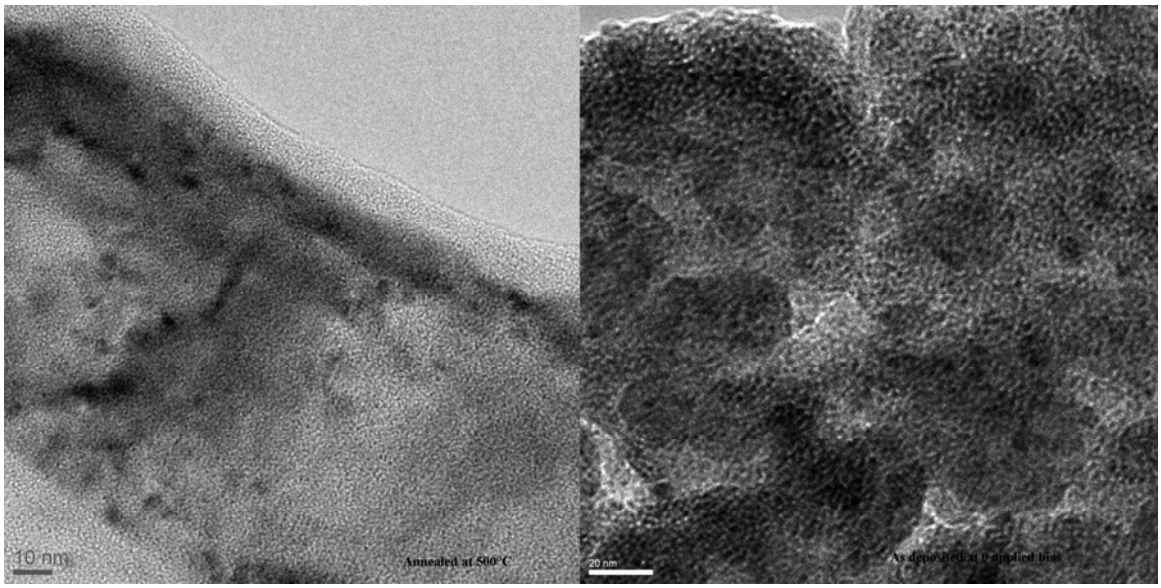

Figure 89. TEM images in bright field mode of the BN-Mo_2N composite deposited at -17V bias(5.5kW,1.5mTorr). The annealed sample is on the left and the as deposited sample is on the right.

6.7 Annealing effects on sample prepared at -50V bias

The sample deposited at -50V bias shows significant improvements in hardness. The hardness rises to 28.22 GPa from 18.48 GPa. This is a ~50% rise in hardness. TEM studies on the annealed samples show sharp contrast between the two phases (Mo_2N and BN) but the as-deposited samples show low contrast between the two different phases. The BN phase is amorphous in the as-deposited sample. On annealing the sample shows sharper phase contrast in the bulk which is an obvious result of recrystallization and phase separation (Figure 90). The BN phase in the as-deposited sample was amorphous which on annealing recrystallized into the hexagonal BN (h-BN) as show in Figure 91. Lattice measurements on the HRTEM images identify the lattice parameter(~3.4-3.5 nm) to be the basal plane of h-BN, this is consistent with literature (~3.3 - 3.83 nm) [115].

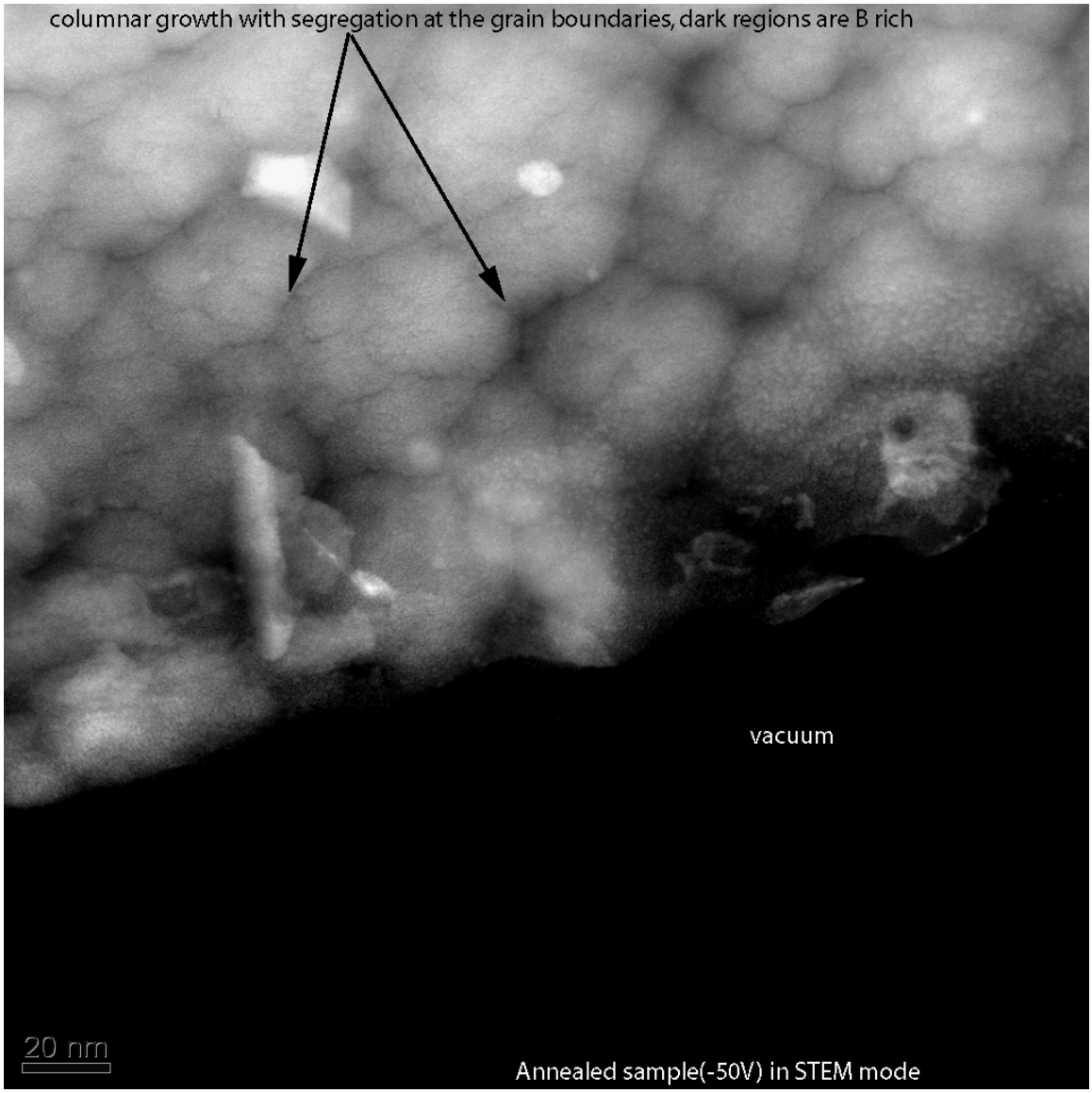

Figure 90. Cosputtered composite BN-Mo_2N deposited at -50V bias and annealed.

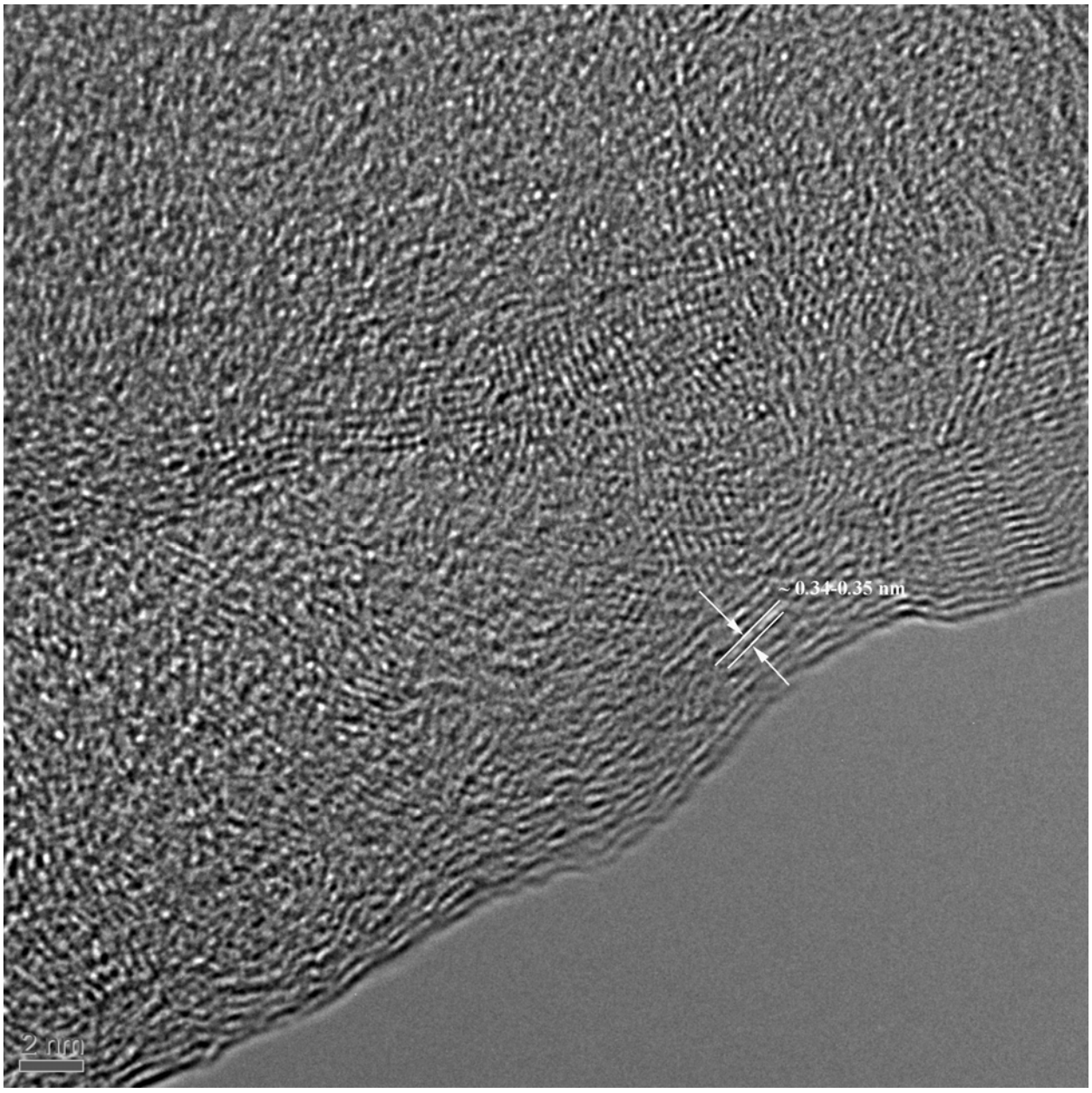

Figure 91. The TEM image in BF mode showing h-BN. The sample was deposited at 5.5kW,50 bias and 1.5mTorr N2 partial pressure and annealed at 500°C.

6.8 Annealing effects on sample prepared at -120V bias

The as deposited coating at higher bias (-120V) shows regions of phase decomposition as evidenced by the Z-contrast image in Figure 92 (a) and its contrast modulation which has an origin in the difference in atomic number (B=dark and Mo=bright). On annealing this contrast is lost but the sample showed enhanced crystallinity and loss of the regions of phase segregation Figure 92 (b). The hardness rises from 14.7 GPa to ~16.58 GPa on annealing, The 12% rise in hardness is due to recrystallization and growth effects that are expected with annealing. TEM analysis on the as deposited coating at -120V still exhibits crystallinity Figure 93. At -120V bias the energetic are high enough to support crystallinity even without annealing.

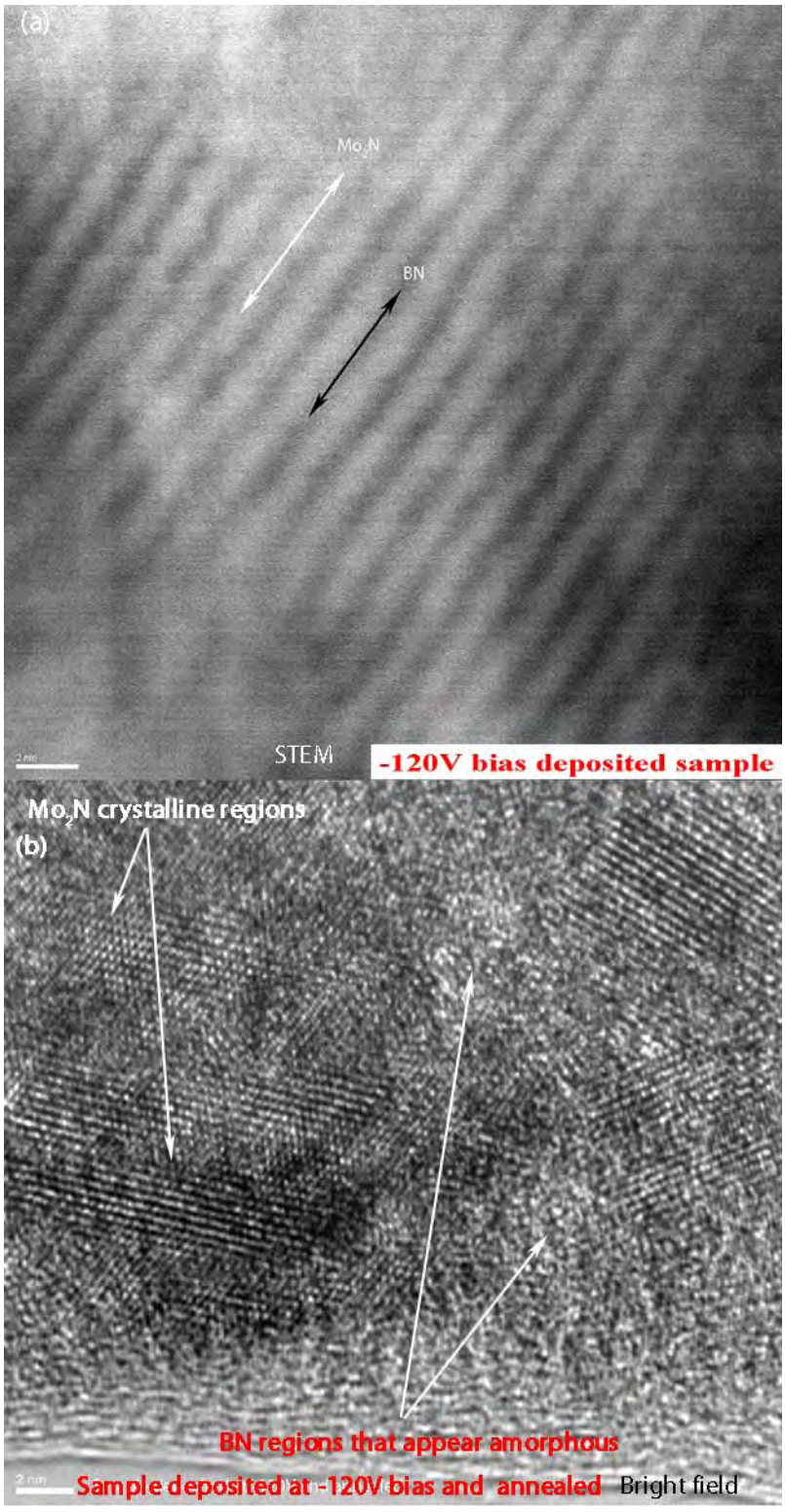

Figure 92. TEM images of as deposited sample and annealed samples deposited at -120V bias.

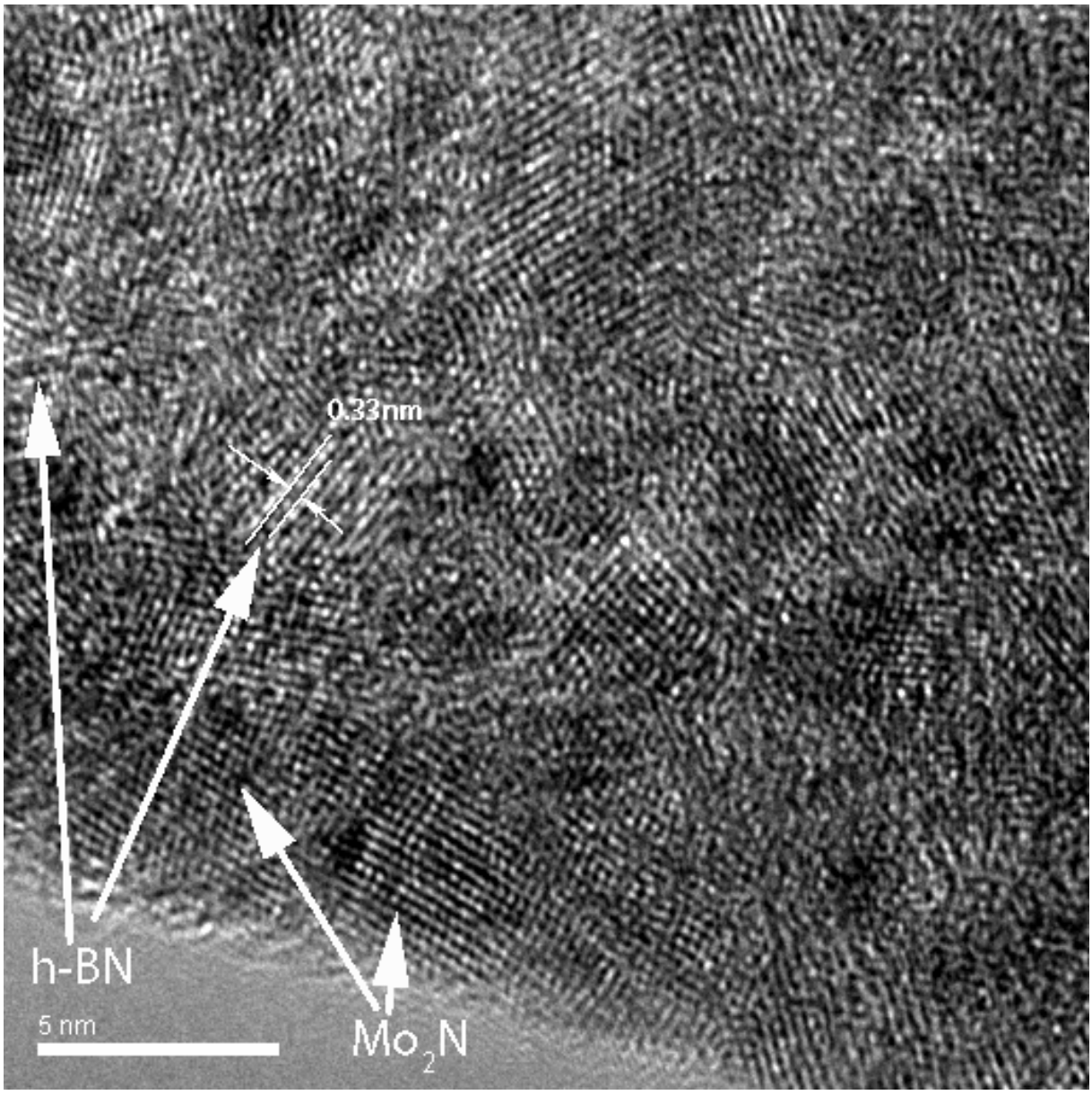

Figure 93. The high-resolution electron microscope (HREM) image shows a lattice spacing of 0.33 nm, corresponding to the spacing between the (0 0 2) planes of h-BN. The sample is the as deposited sample at 5.5kW,-120 V bias and 1.5 mTorr of N_2.

6.9 Conclusions and discussions

The goal of the study in this chapter was to optimize the bulk properties for the BN-Mo_2N coatings and eventually deposit CrN/ BN-Mo_2N multilayer coatings. A deposition condition of 5.5 kW , 1.5 mTorr and -50 V bias was selected because of its high sputtering rate, low residual stress (<2 GPa) and hardness (~ 25-30 GPa). Drill bits were coated with the CrN/(BN-Mo_2N) multilayers. Bias had a strong effect on the hardness of the composite BN-Mo_2N phase. TEM analysis of the coatings showed phase segregation of the boron phase and the molybdenum phases. TGA studies on BN shows a steady mass gain with temperature, associated with B_2O_3 formation. B_2O_3 at high temperature forms a glass like phase and could aid in lowering the friction at high temperature[98]. The samples deposited at 0,-50V and -120V applied bias showed significant hardening on annealing. The hardness improvement on annealing was primarily due to recrystallization and growth, but what is most interesting is the formation of h-BN on annealing. It was also shown that at -120V bias a combination of a-BN and h-BN phases form in the cosputtered phase. Annealing these films improves its hardness.

Low annealing temperatures and short duration of anneal (2 hrs) could be a contributing factor to the difference in hardening. These lower temperatures and shorter annealing times are responsible for incomplete recrystallization and growth in the films, particularly in the films deposited at 0V bias that develops no crystallinity even on annealing. In other reactively sputtered boron systems annealing temperatures of 1000 °C were reported [116]. In short it is likely that increasing annealing temperatures and durations of anneal could produce or further improve crystallinity. High resolution TEM studies shows the samples deposited at 120V bias, -50 V and 2 kW form h-BN on annealing. The recrystallization and growth and phase

transformation of a-BN to h-BN are responsible for the rise in hardness in these samples. Bias plays a significant role in controlling the growth kinetics and physical properties of the deposited films. Low applied bias during growth is associated with low adatom mobility. The energetics of the incoming species is relatively lower and hence amorphous crystals are formed characterized by columnar growth (0V bias). Hence the lack of crystallinity in our sample was due to the low applied bias and the low deposition temperatures (~100-150°C). At higher bias such as -120V , enhanced bombardment have been shown to significantly increase defects in the coating [117]. It is also well know that the relative amounts of trapped Argon in the coating increased with bias [118]. The bulk properties are heavily influenced by the enhanced defect concentrations and trapped argon gas atoms in the interstitial sites [119]. Higher bias conditions will also disproportionately resputter B (B=11 a.m.u, Mo= 40 a.m.u). The deposition rate of BN is highly sensitive to resputtering and is a strong function of bias. At high enough bias conditions complete resputtering of B has also been reported.[108]. This difference in deposition rate with bias could play a part in the hardness of the coating. It is also important to note that the recrystallization of a-BN to h-BN is incomplete and there are regions in the -120 V sample in which regions of a-BN is clearly apparent. Increasing the annealing temperatures and duration of anneal could further improve the recrystallization.

The bias region of -50V is characterized by ions in the intermediate energy regimes that aid in densification caused by implantation, recoil processes and forward sputtering into voided regions in agreement with published Monte Carlo and Molecular dynamic models [120]. There is enhancement of adatom mobility from the enhanced energetics of the charged species impinging on the surface. The energy knocks to the growing species on the surface leads to decreases in

void densities. Annealing the sample deposited at these intermediate bias conditions recrystallizes and grows these structure which leads to further hardening. The hardness improvements seen at -50V is also related to recrystallization and growth and phase transformations from a-BN to h-BN.

At all deposition conditions it is important to note there are nanoscale BN inclusions surrounded by Mo_2N. The associated surface area with these nanoscale precipitates would also act as a large driving force for recrystallization and growth during annealing.

Chapter 7. Future Work

The eventual goal of chapter 6 was to deposit CrN/BN-Mo_2N multilayer coatings. The CrN/BN-Mo_2N multilayer coatings were optimized for adhesion and hardness and coated on drill bits provided by Ford and Boeing. Validation testing on these composite multilayers coated drill bits would be an immediate future goal. In addition, witness polished M2, 1'' coupons, were coated with this composite material. A detailed study on the high temperature friction properties as conducted in Chapter 4 will be appropriate for these coating. It would also be insightful to collect wear debris at the tested temperatures and subject to quantitative as well as qualitative EDS analysis. Our tests in nitrogen have shown that controlling the atmosphere provided an added parameter to tune the performance of the coatings. The ability to control the atmosphere of the tribometer at ANL has significantly increased over these few years. A cage/ glove box has now been added to the machine to isolate the sample from atmosphere. Hence friction testing in a N_2 atmosphere together with wear debris analysis would be insightful in understanding any humidity and oxygen effects. It will also be extremely interesting to understand how the presence of CrN layer, known to be an oxygen diffusion barrier, would affects the oxidation stability/rates of the BN.

The choice of the drill bit material has a very important role to play in improving coating adhesion and overall coating performance. The WC drill bit exhibit porosity in the bulk and it is likely that the porosity could adversely affect coating adhesion. For future work it will be appropriate to systematically study the effects of WC's bulk porosity on coating performance. The WC drill bits are made (by manufacturer) via the powder metallurgy route, which accounts

for its porosity. Since our coatings have performed well as a hard coating, the extra hard WC substrate could be unnecessary and could even be replaced with a HSS drill bit.

Surface analysis of some of the coated HSS drill bits show that parts of the coating on the drill bit exhibited low angle columnar growth morphology or atomic shadowing effects. Such low angle growth areas are typically not fully densified and leads to coatings of inferior properties. Increasing the bias during deposition and hence enhancing atomic mobility on the coating surface during growth should easily prevent this problem.

An extension of this work could also include tests insitu studies (tribometer or TEM) to characterize tribo-induced phase transformations. Tests in a TEM would be able to characterize any texture of MoO_3 already deposited on the surface. Studies are already underway via SEM, in back scattering mode, to characterize any texturing (easy slip planes aligning themselves parallel to the surface to lower friction of the ball as it passes over) that has already resulted in the samples that were tested at high temperature.

In the industrial validation tests, metal adhesion on the drill bits tested at Boeing was a significant concern. CrN could be detrimental to our coating performance due to BUE formation. This is particularly important since our coatings operate at high temperature. Metals or alloys containing Cr always exhibit high friction and strong adhesion interaction with tool materials and a tendency to have built-up edge (BUE) formation. TiAlN-CrN/Mo_2N, TiAlN-VN/Mo_2N would be very interesting multilayer coatings to study. The presence of Al would also allows for the formation of an Al_2O_3 passivation layer on the surface of the coated tool, which may reduce the rate of oxidation.

The presence of Cr_2O_3 in the lubricating film at higher temperature is detrimental to the self lubrication mechanism. CrN may not have been the most appropriate phase to combine with Mo_2N in the multilayer system. TiN offers an excellent substitute with its high hardness, good adhesion and oxidation resistance. Mo_2N will preferentially oxidize in environments of limited oxygen and the absence of the abrasive phase at high temperature would further reduce the friction. It would also be possible to improve the temperature resistance of the Ti layer by incorporating Al specifically the (Ti,Al)N type alloys.

Incorporating other elements, that oxidize at high temperature to form lubricious oxides, was a goal of this project. The nitrides of W (WN_2) offer an alternative option that is oxidation resistant up to temperatures of 800°C. Replacing some of the molybdenum strips in the composite target with W can be immediately done. The W strips have been ordered and it can be readily incorporated into a target to make a Mo-W-B_4C composite target. The incorporation of W which forms a high temperature lubricious phase[15] into our coating would be a logical extension of this work.

References

[1] Voevodin, A. A.; Zabinski, J. S.; Muratore, C., Recent Advances in Hard, Tough, and Low Friction Nanocomposite Coatings. 10, (6), 665-679.

[2] Quinto, D., Twenty-five years of PVD coatings the cutting edge. SVC bulletin 1001,Oct, 17,(2007).

[3] Mayrhofer, P. H.; Mitterer, C.; Hultman, L.; Clemens, H., Microstructural design of hard coatings. Progress in Materials Science 51, (8), 1032-1114,(2006).

[4] Veprek, S., The search for novel, superhard materials. Journal of Vacuum Science & Technology A 17, (5), 2401-2420,(1999).

[5] Veprek, S.; Argon, A. S., Mechanical properties of superhard nanocomposites. Surface & Coatings Technology 146, 175-182,(2001).

[6] Lee, K. W.; Chen, Y. H.; Chung, Y. W.; Keer, L. M., Hardness, internal stress and, thermal stability of TiB2/TiC multilayer coatings synthesized by magnetron sputtering with and without substrate rotation. Surface & Coatings Technology 177, 591-596,(2004).

[7] DErrico, G. E.; Chiara, R.; Guglielmi, E., PVD coatings of cermet inserts for milling applications. Surface & Coatings Technology 86-7, (1-3), 735-738,(1996).

[8] Fella, R.; Holleck, H.; Schulz, H., Preparation and Properties of Wc-Tic-Tin Gradient Coatings. Surface & Coatings Technology 36, (1-2), 257-264,(1988).

[9] Weinert, K.; Inasaki, I.; Sutherland, J. W.; Wakabayashi, T., Dry machining and minimum quantity lubrication. Cirp Annals-Manufacturing Technology 53, (2), 511-537,(2004).

[10] Comission, E. U., Dry machining solutions for greener automative production. (2000).

[11] Graham M. E, Ford Boeing Northwestern alliance research proposal/ Dry Machining 2004 NSF proposal. Private communication, (2004,2007).

[12] Gangopadhyay, A.; Jahanmir, S.; Peterson, M. B., Self-lubricating ceramic matrix composites. Friction and Wear of Ceramics, 163–197,(1994).

[13] Voevodin, A. A.; Prasad, S. V.; Zabinski, J. S., Nanocrystalline carbide amorphous carbon composites. Journal of Applied Physics 82, (2), 855-858,(1997).

[14] Voevodin, A. A.; O'Neill, J. P.; Zabinski, J. S., Tribological performance and tribochemistry of nanocrystalline WC/amorphous diamond-like carbon composites. Thin Solid Films 342, (1-2), 194-200,(1999).

[15] Erdemir, A., A crystal-chemical approach to lubrication by solid oxides. Tribology Letters 8, (2-3), 97-102,(2000).

[16] Constable, C. P.; Yarwood, J.; Hovsepian, P.; Donohue, L. A.; Lewis, D. B.; Munz, W. D., Structural determination of wear debris generated from sliding wear tests on ceramic

coatings using Raman microscopy. Journal of Vacuum Science & Technology A 18, (4), 1681-1689,(2000).

[17] Derflinger, V.; Brandle, H.; Zimmermann, H., New hard/lubricant coating for dry machining. Surface & Coatings Technology 113, (3), 286-292,(1999).

[18] Hofmann, S.; Jehn, H. A., Oxidation Behavior of Crnx and (Cr,Al)Nx Hard Coatings. Werkstoffe Und Korrosion-Materials and Corrosion 41, (12), 756-760,(1990).

[19] Hones, P.; Sanjines, R.; Levy, F., Characterization of sputter-deposited chromium nitride thin films for hard coatings. Surface & Coatings Technology 94-5, (1-3), 398-402,(1997).

[20] Hones, P.; Martin, N.; Regula, M.; Levy, F., Structural and mechanical properties of chromium nitride, molybdenum nitride, and tungsten nitride thin films. Journal of Physics D-Applied Physics 36, (8), 1023-1029,(2003).

[21] Lyo, I. W.; Ahn, H. S.; Lim, D. S., Microstructure and tribological properties of plasma-sprayed chromium oxide-molybdenum oxide composite coatings. Surface & Coatings Technology 163, 413-421,(2003).

[22] Chu, X.; Barnett, S. A., Model of Superlattice Yield Stress and Hardness Enhancements. Journal of Applied Physics 77, (9), 4403-4411,(1995).

[23] Grove, W. R., On the Electro-polarity of gases. Phil. Trans. Soc. London 142, 87-101,(1852).

[24] Kay, E., Magnetic Field Effects on an Abnormal Trncated Glow Discharge and Their Relation to Sputtered Thin-Film Growth. Journal of Applied Physics 34, (4), 760-&,(1963).

[25] Yarshar, P. structure, mechanical properties and thermal properties of sputter deposited nitride and oxide superlattice thin films. Northwestern university, 1998.

[26] Martin, K. J. Structure, mechanical properties and high temperature stability of nanolayered titanium nitride/titanium diboride and zirconium nitride/zirconium diboride thin films. Northwestern University, 2001.

[27] Kelly, P. J.; Arnell, R. D., Magnetron sputtering: a review of recent developments and applications. Vacuum 56, (3), 159-172,(2000).

[28] Adibi, F.; Petrov, I.; Greene, J. E.; Hultman, L.; Sundgren, J. E., Effects of High-Flux Low-Energy (20-100 Ev) Ion Irradiation during Deposition on the Microstructure and Preferred Orientation of Ti0.5al0.5n Alloys Grown by Ultra-High-Vacuum Reactive Magnetron Sputtering. Journal of Applied Physics 73, (12), 8580-8589,(1993).

[29] Window, B.; Savvides, N., Unbalanced Dc Magnetrons as Sources of High Ion Fluxes. Journal of Vacuum Science & Technology a-Vacuum Surfaces and Films 4, (3), 453-456,(1986).

[30] Wu, L. C.; Greene, J. E., Mechanisms of the Reactive-Sputter and Chemical-Sputter Deposition of Tio2 from Ti and Tic Targets in Mixed Ar+O2 Discharges. Journal of Applied Physics 50, (7), 4966-4971,(1979).

[31] Ehiasarian, A. P.; New, R.; Munz, W. D.; Hultman, L.; Helmersson, U.; Kouznetsov, V., Influence of high power densities on the composition of pulsed magnetron plasmas. Vacuum 65, (2), 147-154,(2002).

[32] Thornton, J. A., Influence of Substrate Temperature and Deposition Rate on Structure of Thick Sputtered Cu Coatings. Journal of Vacuum Science & Technology 12, (4), 830-835,(1975).

[33] Messier, R., Toward Quantification of Thin-Film Morphology. Journal of Vacuum Science & Technology a-Vacuum Surfaces and Films 4, (3), 490-495,(1986).

[34] Guenther, K. H., Non-Optical Characterization of Optical Coatings. Applied Optics 20, (20), 3487-3502,(1981).

[35] Guenther, K. H., The Influence of the Substrate Surface on the Performance of Optical Coatings. Thin Solid Films 77, (1-3), 239-251,(1981).

[36] Hakansson, G.; Sundgren, J. E.; Mcintyre, D.; Greene, J. E.; Munz, W. D., Microstructure and Physical-Properties of Polycrystalline Metastable Ti0.5al0.5n Alloys Grown by Dc Magnetron Sputter Deposition. Thin Solid Films 153, 55-65,(1987).

[37] Oliver, W. C.; Pharr, G. M., An Improved Technique for Determining Hardness and Elastic-Modulus Using Load and Displacement Sensing Indentation Experiments. Journal of Materials Research 7, (6), 1564-1583,(1992).

[38] Hay, J. C.; Bolshakov, A.; Pharr, G. M., A critical examination of the fundamental relations used in the analysis of nanoindentation data. Journal of Materials Research 14, (6), 2296-2305,(1999).

[39] Bull, S. J., Failure mode maps in the thin film scratch adhesion test. Tribology International 30, (7), 491-498,(1997).

[40] Stoney, G., The Tension of Metallic Films Deposited by Electrolysis. Proceedings of the Royal Society of London. Series A, Containing Papers of a Mathematical and Physical Character, 82, (553), 172-175,(1909).

[41] Shieu, F. S.; Shiao, M. H., Measurement of the interfacial mechanical properties of a thin ceramic coating on ductile substrates. Thin Solid Films 306, (1), 124-129,(1997).

[42] Shieu, F. S.; Sass, S. L., Dislocation Mechanisms for the Relaxation of Thermal-Stress at Metal Ceramic Interfaces. Acta Metallurgica Et Materialia 39, (4), 539-547,(1991).

[43] Ohring, M., *The materials science of thin films*. ed.; San Diego, 2001; 'Vol.' p.

[44] Stearns, M. B.; Lee, C. H.; Groy, T. L., Structural Studies of Co/Cr Multilayered Thin-Films. Physical Review B 40, (12), 8256-8269,(1989).

[45] Hirsch, P.; Howie, A.; Nocholson, R.; Pashley, D. W.; Whelan, M. J., *Electron Microscopy of Thin Crystals.* ed.; Krieger Publishing Co.: Malabar, 1977; 'Vol.' p.

[46] Williams, D. B.; Carter, C. B., *Transmission Electron Microscopy: A Text Book for Materials Science.* ed.; Plenum Press: New York, 1996; 'Vol.' p.

[47] Reimer, L., *Transmission Electron Microscropy (Springer Series in Optical Sciences;v36)*. ed.; Springer-Verlag: Berlin, 1984; 'Vol.' p.

[48] Buseck, P. R.; Epelboin, Y.; Rimsky, A., Signal-Processing of High-Resolution Transmission Electron-Microscope Images Using Fourier-Transforms. Acta Crystallographica Section A 44, 975-986,(1988).

[49] Weaver, L., Cross-section TEM sample preparation of multilayer and poorly adhering films. Microscopy Research and Technique 36, (5), 368-371,(1997).

[50] Zhang, Z. G.; Rapaud, O.; Bonasso, N.; Mercs, D.; Dong, C.; Coddet, C., Control of microstructures and properties of dc magnetron sputtering deposited chromium nitride films. Vacuum 82, (5), 501-509,(2008).

[51] Prchlik, L.; Sampath, S.; Gutleber, J.; Bancke, G.; Ruff, A. W., Friction and wear properties of WC-Co and Mo-Mo2C based functionally graded materials. Wear 249, (12), 1103-1115,(2001).

[52] Urgen, M.; Eryilmaz, O. L.; Cakir, A. F.; Kayali, E. S.; Nilufer, B.; Isik, Y., Characterization of molybdenum nitride coatings produced by arc-PVD technique. Surface & Coatings Technology 94-5, (1-3), 501-506,(1997).

[53] Solak, N.; Ustel, F.; Urgen, M.; Aydin, S.; Cakir, A. F., Oxidation behavior of molybdenum nitride coatings. Surface & Coatings Technology 174, 713-719,(2003).

[54] Suszko, T.; Gulbinski, W.; Jagielski, J., The role of surface oxidation in friction processes on molybdenum nitride thin films. Surface & Coatings Technology 194, (2-3), 319-324,(2005).

[55] Li, Z. W.; He, Y. D.; Gao, W., Use of a solid-state oxygen pump to study oxidation kinetics of Cr and Mo. Oxidation of Metals 53, (5-6), 577-596,(2000).

[56] Rudnik, P. J.; Graham, M. E.; Sproul, W. D., High-Rate Reactive Sputtering of Monx Coatings. Surface & Coatings Technology 49, (1-3), 293-297,(1991).

[57] Suszko, T.; Gulbinski, W.; Jagielski, J., Mo_2N/Cu thin films - the structure, mechanical and tribological properties. Surface & Coatings Technology 200, (22-23), 6288-6292,(2006).

[58] Conde, A.; Cristobal, A. B.; Fuentes, G.; Tate, T.; de Damborenea, J., Surface analysis of electrochemically stripped CrN coatings. Surface & Coatings Technology 201, (6), 3588-3595,(2006).

[59] Han, S.; Lin, J. H.; Wang, G. H.; Shih, H. C., The effect of preferred orientation on the mechanical properties of chromium nitride coatings deposited on SKD11 by unbalanced magnetron sputtering. Materials Letters 57, (5-6), 1202-1209,(2003).

[60] Hovsepian, P. E.; Munz, W. D., Recent progress in large-scale production of nanoscale multilayer/superlattice hard coatings. Vacuum 69, (1-3), 27-36,(2002).

[61] Patscheider, J.; Zehnder, T.; Diserens, M., Structure-performance relations in nanocomposite coatings. Surface & Coatings Technology 146, 201-208,(2001).

[62] Erdemir, A.; Halter, M.; Fenske, G. R., Preparation of ultralow-friction surface films on vanadium diboride. Wear 205, (1-2), 236-239,(1997).

[63] Voevodin, A. A.; Zabinski, J. S., Supertough wear-resistant coatings with 'chameleon' surface adaptation. Thin Solid Films 370, (1-2), 223-231,(2000).

[64] Strong, K. L.; Zabinski, J. S., Tribology of pulsed laser deposited thin films of cesium oxythiomolybdate (CS2MoOS3). Thin Solid Films 406, (1-2), 174-184,(2002).

[65] Lugscheider, E.; Knotek, O.; Bobzin, K.; Barwulf, S., Tribological properties, phase generation and high temperature phase stability of tungsten- and vanadium-oxides deposited by reactive MSIP-PVD process for innovative lubrication applications. Surface & Coatings Technology 133, 362-368,(2000).

[66] PalDey, S.; Deevi, S. C., Single layer and multilayer wear resistant coatings of (Ti,Al)N: a review. Materials Science and Engineering a-Structural Materials Properties Microstructure and Processing 342, (1-2), 58-79,(2003).

[67] Munz, W. D., Titanium Aluminum Nitride Films - a New Alternative to Tin Coatings. Journal of Vacuum Science & Technology a-Vacuum Surfaces and Films 4, (6), 2717-2725,(1986).

[68] Horling, A.; Hultman, L.; Oden, M.; Sjolen, J.; Karlsson, L., Thermal stability of arc evaporated high aluminum-conteht Ti1-xAlxN thin films. Journal of Vacuum Science & Technology a-Vacuum Surfaces and Films 20, (5), 1815-1823,(2002).

[69] Musil, J.; Hruby, H., Superhard nanocomposite Ti1-xAlxN films prepared by magnetron sputtering. Thin Solid Films 365, (1), 104-109,(2000).

[70] Koshy, R. A.; Graham, M. E.; Marks, L. D., Synthesis and characterization of CrN/Mo_2N multilayers and phases of Molybdenum nitride. Surface & Coatings Technology 202, (4-7), 1123-1128,(2007).

[71] Kofstad, P.; Lillerud, K. P., On High-Temperature Oxidation of Chromium .2. Properties of Cr2O3 and the Oxidation Mechanism of Chromium. Journal of the Electrochemical Society 127, (11), 2410-2419,(1980).

[72] Lee, D. B.; Lee, Y. C.; Kwon, S. C., High temperature oxidation of a CrN coating deposited on a steel substrate by ion plating. Surface & Coatings Technology 141, (2-3), 227-231,(2001).

[73] Graham, M. E.; Rudnik, P. J.; Spoul, W. D., High rate reactive sputtering of CrN_x coatings In ed.; 'Ed.'^'Eds.' 'Vol.' p^pp.

[74] Diesselberg, M.; Stock, H. R.; Mayr, P., Friction and wear behaviour of PVD chromium nitride supported carbon coatings. Surface & Coatings Technology 188-89, 612-616,(2004).

[75] Ho, W. Y.; Huang, D. H.; Huang, L. T.; Hsu, C. H.; Wang, D. Y., Study of characteristics of Cr2O3/CrN duplex coatings for aluminum die casting applications. Surface & Coatings Technology 177, 172-177,(2004).

[76] Ajayi, O. O.; Erdemir, A.; Erck, R. A.; Fenske, G. R.; Nichols, F. A., The Role of Soft (Metallic) Films in the Tribological Behavior of Ceramic Materials. Wear 149, (1-2), 221-232,(1991).

[77] Miyoshi, K., Lapping of Manganese-Zinc Ferrite by Abrasive Tape. Lubrication Engineering 38, (3), 165-172,(1982).

[78] Bowden, F. P.; Tabor, D., *The friction and lubrication of solids*. ed.; Clarendon Press: Oxford, 1986; 'Vol.' p.

[79] Suzuki, M.; Moriyama, M.; Nishimura, M.; Hasegawa, M., Friction and Wear of Self-Lubricating Composites at Temperatures to 450-Degrees-C in Vacuum. Wear 162, 471-479,(1993).

[80] Gulbinski, W.; Suszko, T.; Sienicki, W.; Warcholinski, B., Tribological properties of silver- and copper-doped transition metal oxide coatings. Wear 254, (1-2), 129-135,(2003).

[81] Magneli, A., Structures of the ReO3-type with recurrent dislocations of atoms: `homologous series' of molybdenum and tungsten oxides. Acta Crystallographica 6, (6 %R doi:10.1107/S0365110X53001381), 495-500,(1953).

[82] Storz, O.; Gasthuber, H.; Woydt, M., Tribological properties of thermal-sprayed Magneli-type coatings with different stoichiometries (TinO2n-1). Surface & Coatings Technology 140, (2), 76-81,(2001).

[83] Magneli, A.; Aderson, S.; Westmann, S. 1959; p^pp.

[84] Serratos, M.; Bronson, A., The effect of oxygen partial pressure on the stability of Magneli phases in high temperature corrosive wear. Wear 198, (1-2), 267-270,(1996).

[85] Goto, M.; Yamamoto, T.; Honda, F., Thickness dependency of the lubricity of Ag thin films deposited on Si(111)7 X 7 surface. Tribological Research and Design for Engineering Systems, 133-140

921,(2003).

[86] Spalvins, T.; Buzek, B., Frictional and Morphological-Characteristics of Ion-Plated Soft Metallic-Films. Thin Solid Films 84, (3), 267-272,(1981).

[87] Vetter, J.; Knaup, R.; Dwuletzki, H.; Schneider, E.; Vogler, S., Hard coatings for lubrication reduction in metal forming. Surface & Coatings Technology 86-7, (1-3), 739-746,(1996).

[88] Sproul, W. D., Very high rate reactive sputtering of TiN, ZrN and HfN. Thin Solid Films 107, (2), 141-147,(1983).

[89] Perry, A. J.; Grossl, M.; Hammer, B., Some characteristics of HfN coatings on cemented carbide substrates. Thin Solid Films 129, (3-4), 263-279,(1985).

[90] Helmersson, U.; Johansson, B. O.; Sundgren, J.-E.; Hentzell, H. T. G.; Billgren, P., Adhesion of titanium nitride coatings on high-speed steels. Journal of Vacuum Science & Technology A: Vacuum, Surfaces, and Films 3, (2), 308-315,(1985).

[91] Hammer, B.; Perry, A. J.; Laeng, P.; Steinmann, P. A., The scratch test adhesion of TiC deposited industrially by chemical vapour deposition on steel. Thin Solid Films 96, (1), 45-51,(1982).

[92] Frederick, J. R.; D'Arcy-Gall, J.; Gall, D., Growth of epitaxial CrN on MgO(001): Role of deposition angle on surface morphological evolution. Thin Solid Films 494, (1-2), 330-335,(2006).

[93] Thornton, J. A., The Microstructure of Sputter-Deposited Coatings. Journal of Vacuum Science & Technology a-Vacuum Surfaces and Films 4, (6), 3059-3065,(1986).

[94] Schulz, K. J.; Viswanathan, K. V.; Wall, A. C.; Bowen, A. J., The Effect of Low Mobility Sputter Conditions on Thin-Film Disk Tribology. Ieee Transactions on Magnetics 28, (5), 2527-2529,(1992).

[95] Panich, N.; Wangyao, P.; Hannongbua, S.; Sricharoenchai, P.; Sun, Y., Tribological study of nano-multilayered ultra-hard coatings based on TIB2. Reviews on Advanced Materials Science 13, (2), 25-32,(2006).

[96] Berger, M.; Karlsson, L.; Larsson, M.; Hogmark, S., Low stress TiB2 coatings with improved tribological properties. Thin Solid Films 401, (1-2), 179-186,(2001).

[97] Miyake, S.; Hashizume, T.; Kurosaka, W.; Sakurai, M.; Wang, M., Deposition and tribology of carbon and boron nitride nanoperiod multilayer solid lubricating films. Surface & Coatings Technology 202, (4-7), 1023-1028,(2007).

[98] Erdemir, A.; Fenske, G. R.; Erck, R. A.; Nichols, F. A.; Busch, D. E., Tribological Properties of Boric-Acid and Boric-Acid-Forming Surfaces .2. Mechanisms of Formation and Self-Lubrication of Boric-Acid Films on Boron-Containing and Boric Oxide-Containing Surfaces. Lubrication Engineering 47, (3), 179-184,(1991).

[99] Erdemir, A.; Bindal, C.; Fenske, G. R., Formation of ultralow friction surface films on boron carbide. Applied Physics Letters 68, (12), 1637-1639,(1996).

[100] Geick, R.; Perry, H.; Rupprecht, G., Normal Modes in Hexagonal Boron Nitride. Physical Review 146, (2), 543.

[101] Koskilinna, J. O.; Linnolahti, M.; Pakkanen, T. A., Friction coefficient for hexagonal boron nitride surfaces from ab initio calculations. Tribology Letters 24, (1), 37-41,(2006).

[102] Yu, N.; Romero-Borja, F.; Zhang, Z. H.; Cui, X. T.; Liu, J. R.; Wood, L. T.; Chu, W. K.; Marton, D.; Rabalais, J. W.; Forster, K. M.; Reeber, R. R., Formation of boron nitride and boron carbide composite by nitrogen implantation at elevated temperature. 63, (12), 1645,(1993).

[103] Saito, T.; Honda, F., Chemical contribution to friction behavior of sintered hexagonal boron nitride in water. Wear 237, (2), 260,(2000).

[104] Graham M. E, Ford Boeing Northwestern alliance research proposal. Private communication, (2007).

[105] Jacobson, N. S.; Morscher, G. N.; Bryant, D. R.; Tressler, R. E., High-temperature oxidation of boron nitride: II, boron nitride layers in composites. Journal of the American Ceramic Society 82, (6), 1473-1482,(1999).

[106] Lavrenko, V. A.; Alexeev, A. F., High-Temperature Oxidation of Boron-Nitride. Ceramics International 12, (1), 25-31,(1986).

[107] Erdemir, A.; Fenske, G. R.; Erck, R. A., A Study of the Formation and Self-Lubrication Mechanisms of Boric-Acid Films on Boric Oxide Coatings. Surface & Coatings Technology 43-4, (1-3), 588-596,(1990).

[108] Kester, D. J.; Messier, R., Phase-Control of Cubic Boron-Nitride Thin-Films. Journal of Applied Physics 72, (2), 504-513,(1992).

[109] Chen, H.; Chen, Y.; Yu, J.; Williams, J. S., Purification of boron nitride nanotubes. Chemical Physics Letters 425, (4-6), 315-319,(2006).

[110] Smithells, C. J.; Brandes, E. A.; Brook, G. B., *Smithells metals reference book*. 7th / edited by E.A. Brandes and G.B. Brook. ed.; Butterworth-Heinemann: Oxford ; Boston, 1992; 'Vol.' p 1 v. (various pagings).

[111] Koshy, R. A.; Graham, M. E.; Marks, L. D., Temperature activated self-lubrication in CrN/Mo2N nanolayer coatings. Surf Coat Technol., (submitted).

[112] Gleiter, H., Nanostructured materials: Basic concepts and microstructure. Acta Materialia 48, (1), 1-29,(2000).

[113] Dannenberg, R.; Stach, E. A.; Groza, J. R.; Dresser, B. J., In-situ TEM observations of abnormal grain growth, coarsening, and substrate de-wetting in nanocrystalline Ag thin films. Thin Solid Films 370, (1-2), 54-62,(2000).

[114] Hao, X. J.; Cho, E. C.; Flynn, C.; Shen, Y. S.; Conibeer, G.; Green, M. A., Effects of boron doping on the structural and optical properties of silicon nanocrystals in a silicon dioxide matrix. Nanotechnology, (42), 424019,(2008).

[115] Mirkarimi, P. B.; McCarty, K. F.; Medlin, D. L., Review of advances in cubic boron nitride film synthesis. Materials Science & Engineering R-Reports 21, (2), 47-100,(1997).

[116] Martin, K. J., Structure, mechanical properties, and high-temperature stability of nanolayered titanium nitride/titanium diboride and zirconium nitride/zirconium diboride thin films [electronic resource]. In ed.; 'Ed.'^'Eds.' 'Vol.' p^pp.

[117] Karr, B. W.; Cahill, D. G.; Petrov, I.; Greene, J. E., Effects of high-flux low-energy ion bombardment on the low-temperature growth morphology of TiN(001) epitaxial layers. Physical Review B 61, (23), 16137-16143,(2000).

[118] Kazansky, P. R.; Hultman, L.; Ivanov, I.; Sundgren, J. E., Gas Porosity Formation in Epitaxial Tin Films Deposited by Reactive Magnetron Sputtering in Mixed Ar/N2

Discharges. Journal of Vacuum Science & Technology a-Vacuum Surfaces and Films 11, (4), 1426-1430,(1993).

[119] Pan, A.; Greene, J. E., Residual Compressive Stress in Sputter-Deposited Tic Films on Steel Substrates. Thin Solid Films 78, (1), 25-34,(1981).

[120] Muller, K. H., Model for Ion-Assisted Thin-Film Densification. Journal of Applied Physics 59, (8), 2803-2807,(1986).